University of Bergen

Master Thesis in Measurement Technology and Nanophysics

Low-temperature microwave plasma chemical vapour deposition of nanocrystalline diamonds for erosion protection on wind turbine blades

---

by
John Benjamin Lothe

Supervisor:
Prof. Bodil Holst

Co-supervisor:
Dr. Justas Zalieckas
Ph.D. Carsten Hinzmann

June, 2021

Department of Physics and Technology
University of Bergen
Norway

Abstract

The demand and growth of renewable energy is increasing even during the pandemic. A significant portion of the renewable energy comes from onshore and offshore wind turbines. Unfortunately, the operational and maintenance (O&M) cost constitute about 15-20% of the cost of wind power. One of the reason for the high O&M cost is due to leading edge erosion on the turbine blades. Leading edge erosion occur when airborn particles such as rain, snow and hail hit the wind turbine blade. These impacts eventually lead to pitting, cracking, and delamination of the surface coating. It is estimated that erosion of the leading edge increase the drag by 6-500% depending on the severity. There exists different solutions for protecting the leading edge, however, they have a shorter lifetime compared to the lifetime of the wind turbine. A long term solution is desirable especially for offshore wind turbines, which are subjected to harsher conditions and more expensive maintenance. For this reason new surface protective coatings are being developed. Dr. Justas Zalieckas of the University of Bergen proposed to use nanocrystalline diamond due to its excellent mechanical properties. It is almost possible to grow nanocrystalline diamond coatings at low temperatures. This can allow nanocrystalline diamond to be grown on temperature sensitive components such as wind turbine blades.

The goal of this thesis is threefold. First, to achieve low temperature deposition of nanocrystalline diamond using a conventional microwave plasma chemical vapour deposition (MWP-CVD) reactor. Second, write a user manual for the reactor. Third, write a new LabVIEW program for the reactor, designed from scratch with the purpose to be more modular.

Low temperature deposition of nanocrystalline diamond was achieved at substrate temperatures of $T_{substrate} > 450°C$. When this is compared to the literature, the results is satisfactory considering the pressure was large, $p > 50$ torr. A user manual was also written for the MWP-CVD reactor. And lastly a new LabVIEW program was created for the MWP-CVD reactor.

Acknowledgements

I want to thank my supervisor Professor Bodil Holst and my co-supervisors Dr. Justas Zalieckas for the guidance and constructive feedback throughout the work with this thesis. I also wish to give special thanks to head engineer Björn Samelin, and Ph.D Carsten Hinzman for advice and discussions. Finally, I want to give thanks to my friends, my family, and my girlfriend for their support and love.

John Benjamin Lothe
01 June, 2021

Contents

List of Figures

List of Tables

Listings

Chapter 1

Introduction

1.1 The Demand for Wind Electricity Generation

According to the report *Global Energy Review 2020*, authored by the International Energy Agency (see Ref [1]), the demand for electricity has gone down by 5% due to the economic downturn caused by the COVID-19 pandemic. Nevertheless the report also establishes that the demand for renewable electricity has continued to rise despite this reduction. This recent growth in renewable energy sources has been attributed primarily to the increased efficiency and cost reduction of the PV solar cells as well as growth in onshore and offshore wind, and it is predicted that renewable electricity production will overtake coal by 2025 as the primary means of producing electricity [2].

To achieve net-zero emission by the year 2050, many countries aim to follow the Sustainable Development Scenario (SDS). The SDS describes the cost effective path for countries to reach a sustainable future in terms of universal access to modern energy services, international climate goals, and reduction in energy-related pollutants [3]. To follow the SDS track, the capacity of wind electricity generation has to continuously increase. This demand in capacity is reflected in the annual electricity production, which rapidly increases over time. Both the onshore and the offshore wind electricity generation grew by 20% in the period 2018-2019, however, the growth in the onshore wind capacity is not quick enough to follow the track set by the SDS [4, 5].

There are several different ways to increase the electricity generation of wind turbines. This includes scaling up the wind turbine rotor, such that areas with good wind conditions are more efficiently taken advantage of; increasing the hub height (i.e. the height wind turbine tower), which extends the rotor into an air flow region with more consistent and larger wind speeds; reducing the costs of the planning stage, production stage, and the maintenance stage; and lastly, increasing the turbine reliability by employing pitch control, a yaw system, or variable rotor

speed [6]. Modern wind turbines employ all of these optimizations.

1.2 Erosion Problem on Wind Turbines

With the increase in rotor size discussed in the previous section, the operational costs and maintenance costs has also increased, and constituted in 2013 (see Ref. [7]), 15-20% of the cost of wind power. Although the report pointed out that the primary cause of downtime in wind turbines are due to problems with the electronic systems, the increased rotor sizes and rotor speeds in modern systems has also increased the rate of erosion on the leading edge.

The review article by Keegan et al [8], on leading edge erosion, discuss the significance of erosion in the section: "4. Leading edge erosion in literature". This section concludes that erosion is a significant issue facing the wind industry. Furthermore, the most challenging part of this is that the lifetime of protective coatings are unpredictable, and that in some cases erosion can become an issue after only 2-3 years of operation. The lifetime of the coating stands in stark contrast to the expected lifetime of the wind turbine itself, which is 15-25 years.

Erosion of the leading edge affects the aerodynamic performance significantly. Tests have shown that leading edge erosion results in an increase of drag ranging between 6-500%, which subsequently leads to a reduction in electricity generation ranging between 2-25% [9]. This erosion is caused by airborn particles like rain, hail, and sand, colliding with the surface of the blade.

The shell of modern wind turbine blades are made out of a thermosetting polymer matrix reinforced with glass fibre or carbon fibre, and then covered with a surface-protective coating, see Figure 1.1. The fibre reinforced composites have a high strength-to-weight ratio, and a high stiffness, making them suited for bearing the weight of the blades. However, these composites also have several inherent weaknesses: They are weak to transverse impact (i.e. impacts parallel to the fibre layer), and degrade when exposed to the working environment, especially from heat, moisture, salinity, and UV-radiation [8]. This leads to the use of surface-protective coatings both on the tower and the blades, with special care for the leading edge. These coatings have to perform well with regard to several challenges as shown in Figure 1.2. Unfortunately, three issues remain critical for the conventional coatings: ice adhesion/accretion, insect accumulation, and erosion caused by impacts with airborn particles [10].

The most used coating is elastomeric polyurethane, however, other materials are also often added to modify the properties of the coating. The elastonomeric

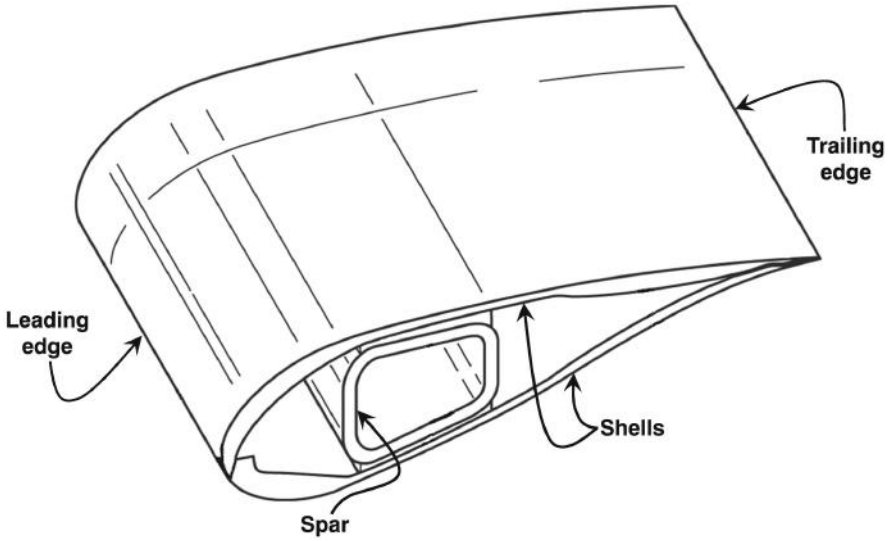

Figure 1.1: Cross-section of a wind turbine blade with elementary components. Image from [11, 12].

polyurethane has rubber-like qualities in addition to having good weatherability. The coating can deform slightly under the impact reducing the impact pressure. As mentioned earlier, other materials can be added to tweak the final properties of the coating. These may include fluoropolymers, which increase the weatherability and increase the anti-icing effect of the coating; acrylic resin; silicone resin; epoxy resin; and others [13].

It has been found that in polyurethane coatings, micrometer-sized morphologies work as nucleation sites for material loss [14], eventually leading to visible deterioration [11]. Fluoropolymer erode by having larger chunks fall off. And for brittle materials (e.g. epoxy resin, silicon resin, and acrylic resin), the failure occur at the large defect sites. Figure 1.3 shows the characteristic evolution of visible deterioration in polyurethane coatings on the leading edge of wind turbines.

1.3 Reducing Erosion on Wind Turbine Blades

The most widely employed solution is protective tapes, most commonly consisting of polyurethane. A specific example of a protective tape is the polyurethane tape by Bergolin. In terms of coatings and paint there exists several solutions, among these are Problade Collision Barrier by LM Wind Power, a 2-component solvent-free polyurethane paint; W4600 by 3M, a 2-component polyurethane coating, applied through brushing it on, or by casting; the polyurethane coating system by Enercon, with a finish consisting of a gel coat, filler, edge protection

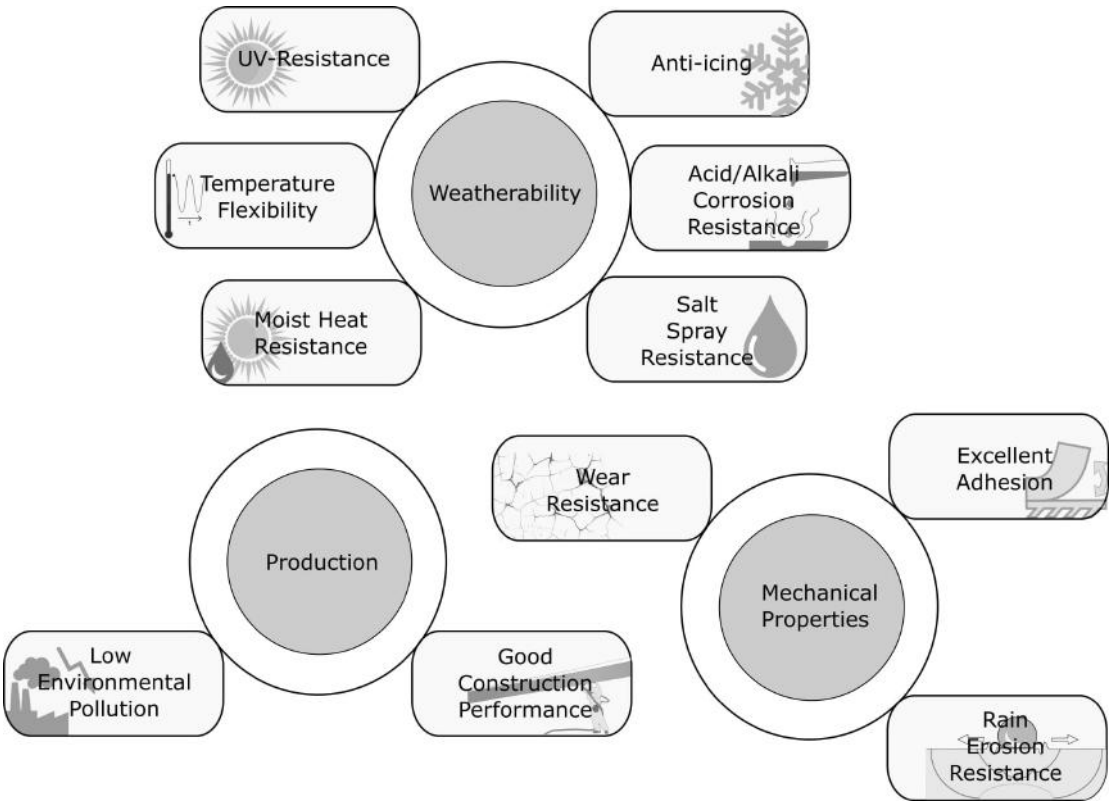

Figure 1.2: The requirements for selecting a suited protective coating [13].

and finally a top coating, all parts consisting of a two-component solvent-free polyurethane; LEP 10 by ALEXIT® BladeRep®, a two-component solvent-free polyurethane coating; and KYNAR PVDF-acrylic hybrid emulsion coating by ARKEMA. Lastly there is the protective sheet known as Blaid by IER Fujikura, and the protective shell known as PowerEdge by Siemens.

Although these solution for leading edge erosion work as intended, they are not an optimal solution to the problem. Many of the previously mentioned solutions run into two issues, they do not serve the entire lifetime of the wind turbine, or they introduce significant drag due to the added material at the leading edge [15].

The development of new protective coatings is based on how the contemporary coatings fail, and the theory of the kinetic interactions. The primary issue with erosion protective coatings is that they have an unpredictable lifetime. The review article Ref [16] discuss the topic of coating lifetime in depth. It reviews the current understanding of the rain droplet impact, how it relates to the wear mechanisms, how different coatings erode, and what the development of new coatings should focus on. The development of new coatings should focus on material systems with the following properties:

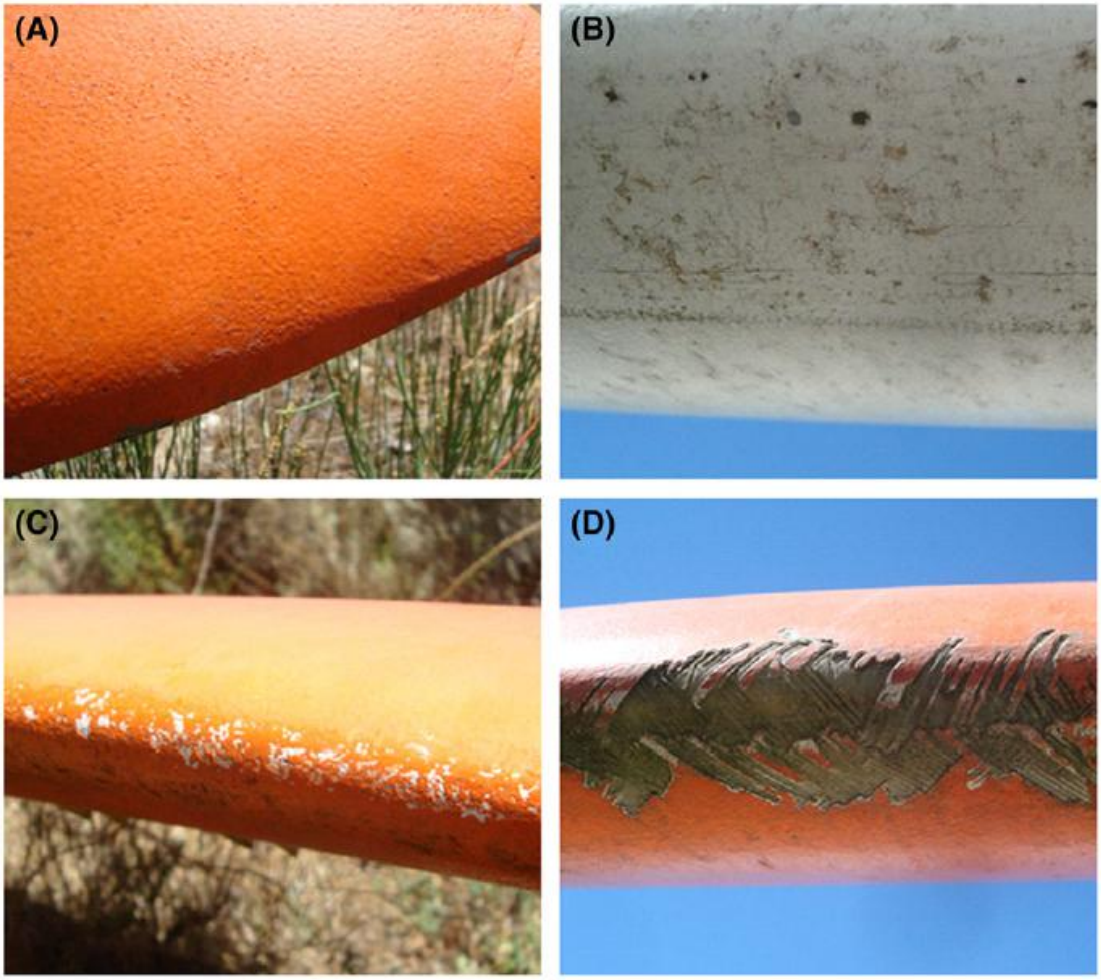

Figure 1.3: Evolution of rain erosion in polyurethane based coatings on the leading edge of wind turbine blades: (A) pitting, (B) cracking, (C) cratering, and (D) delamination. Illustration from: [11].

- Reduction of the water pressure by using rubber-like coatings, i.e. coatings with low modulus of elasticity.
- The coatings with adjustable compressive stresses and adjustable compressive hardness.
- Reduce the amount of coating defects.

Improvement of coating lifetime, has been discussed further by Mishnaevsky (see Ref [15]). In depth discussion was done on the following topics: coating thickness, multiphase coatings, multilayer coatings, reinforced coatings, and reduction of surface roughness.

An important parameter for evaluating new coatings is the damage threshold velocity (DTV). DTV is the lowest impact velocity which result in material

damage. [17] gives an estimate of the DTV:

$$v_{DT} \approx 1.41 c_w \left(\frac{K^2 c_R}{\rho_w^2 c_w^2 d_w} \right)^{\frac{1}{3}} \tag{1.1}$$

where c_w is the compressional wave speed in water, ρ_w is the density of water, K is the fracture toughness of the coating, c_R is the Rayleigh wave velocity in the coating, and d_w is the droplet size. The Rayleigh wave is the surface wave generated by the impact, and is calculated from the Young's modulus E, Poisson's ratio ν, and the density of the coating ρ [18]:

$$c_R = \left(\frac{0.862 + 1.14\nu}{1 + nu} \right) \left(\frac{E}{2(1+\nu)\rho} \right)^{\frac{1}{2}}. \tag{1.2}$$

To maximise the DTV the most important parameters is the fracture toughness and the Rayleigh wave velocity.

1.3.1 Proposed Approach to Reduce Erosion: nanocrystalline diamond Coating

Following the discussion of the critical impact speed, a new coating has been proposed by Dr. Justas Zalieckas: a thin top-coating made out of nanocrystalline diamond. Nanocrystalline diamonds are diamond particles larger than 10 nm, and smaller than 100 nm, which cohere into a solid polycrystal by either fusing together, or by becoming linked together by regions of intermediate materials. The intermediate materials consist of graphite, or amorphous carbon (also known as diamond-like-carbon, DLC). nanocrystalline diamonds have properties shared with conventional single-crystalline diamond. Some of the shared mechanical properties includes high hardness, large Young's modulus, large speed of sound, and a low friction coefficient [19]. Diamond has a large Rayleigh wave velocity, which leads to a large DTV. Furthermore, nanocrystalline diamond films have exceptional performance in bending tests, and can be considered the strongest ceramic foil material [20]. The performance in the bending test allows for high flexibility, and it has been shown that a 1.16 μm thick nanocrystalline diamond film is able to bend around 6.35 mm diameter tube without fracturing [21]. All the aforementioned properties may lead to a higher coating lifetime.

1.4 Nanocrystalline Diamond Coating Synthesis

Nanocrystalline diamond coatings are usually produced by chemical vapour deposition (CVD). Chemical vapour deposition is a technique to grow strong and smooth coatings. In this technique, reactants are activated such that reactions can occur at the substrate. These reactions lead to coating growth. There are different ways the gas is activated in CVD, and for systems growing diamond the gas is activated by creating a plasma. There are several different ways to generate the plasma including a microwave source (MWP-CVD), hot-filament (HF-CVD). These methods produce nanocrystalline diamonds, microcrystalline diamonds, or single-crystalline diamond at relatively low temperatures and low pressures. Using CVD, often requires a substrate temperature between 700 $^{\circ}C$ and 1100 $^{\circ}C$ for good coating quality. Unfortunately, epoxies and other polymer materials used in the composite are temperature sensitive, and heating them up beyond 100 $^{\circ}C$ will decompose them. The lowest deposition temperature using MWP-CVD with a conventional MWP-CVD reactor is located in the range $(80 - 135)^{\circ}C$, using a mix of carbon monoxide, oxygen, and hydrogen, at a pressure of approximately 2 torr [22].

There are four approaches addressing the issue of substrate overheating. The most common approach is to use substrate cooling. The second approach is to use pulse plasma. The third approach is to increase the distance between the substrate and the plasma. The forth is reducing the microwave power.

1.5 Thesis Objective

The objective of this thesis is to achieve growth of nanocrystalline diamonds on polymers, writing a user manual for the reactor, and designing a new program for running the reactor. To be able to grow nanocrystalline diamond on polymers it is necessary to decrease the substrate temperature. To reach the goal, the work is divided into steps:

1. Growth on silicon and carbon fibre using MWP-CVD, where different temperature reduction techniques are tested.

2. Growth on polymers reinforced with carbon fibre.

1.6 Thesis Outline

Chapter 2 explains the theoretical background of diamond growth. It briefly covers the crystal structure of diamond, and the mechanical properties. Additional focus is spent on the topic of diamond growth. Chapter 3 discuss methods used for characterising the nanocrystalline diamond coatings. Chapter 4 presents the experimental setup. Similarly, chapter 5 presents the setup for the simulations. The results from the experiment is shown in chapter 6. The results from the simulations are shown in chapter 7. The thesis conclusion is given in chapter 8. And lastly, chapter 9 discuss the future work. Appendix A is the user manual written by the author. Appendix B describes the new LabVIEW program which runs the MWP-CVD reactor written by the author.

Chapter 2

Theory of Diamond Growth using Microwave Plasma Chemical Vapour Deposition

The growth of diamond on samples of polymer and carbon fiber is not a trivial task as discussed in the introduction. Improper growth conditions may promote a large density of defects, graphite impurities, or may even damage the substrate by overheating or etching. It is thus essential to understand what parameters influence the chemical composition, and the morphology of the deposited material.

In section 2.1 the properties of diamond are discussed with emphasis on mechanical strength, structural defects, and growth. Section 2.2 explains the fundamental principles of the growth technique known as chemical vapour deposition (CVD). The reactor designs used for chemical vapour deposition are divided into different categories based on what gas activation technique they employ, and section 2.3 reviews the technique known as: microwave plasma chemical vapour deposition (MWP-CVD). The model describing the plasma of the MWP-CVD system is shown in section 2.4. And lastly, section 2.5 goes through the theory of heat transfer as it is relevant for the temperature measurements.

2.1 Diamond

2.1.1 What is a Diamond?

Diamond is a solid form of carbon arranged in a crystalline structure known as diamond cubic[1], shown in Figure 2.1. A carbon atom has 6 electrons in total, with 4 of them being valence electrons. In cubic diamond, the carbon atom utilizes its 4 valence electrons to bond with 4 neighbouring carbon atoms. This forms a tetrahedral structure. To achieve the tetrahedral bonding symmetry the orbitals

[1]Diamond can also exist in other crystalline structures and are classified by its polytype. Examples of such materials are: hexagonal diamond (polytype: 2H, name: Lonsdaleite).

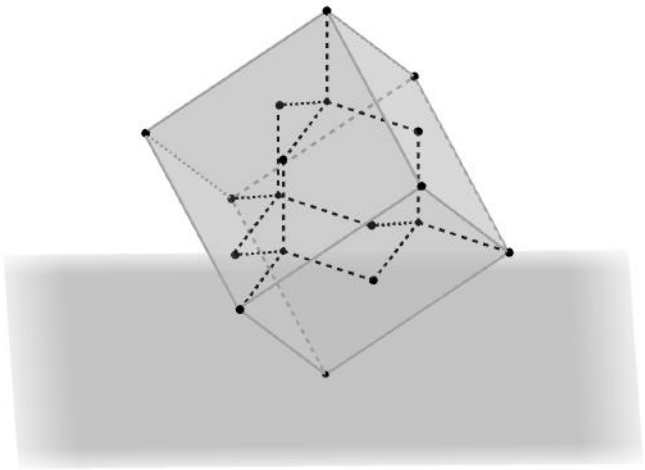

Figure 2.1: Diamond cubic. The black spherical dots show the position of the carbon atoms. The dotted lines show the bonds formed between nearby carbon atoms. Each carbon atom forms bonds with 4 nearby carbon atom forming tetrahedral symmetry. The surrounding grey cube shows the faces of the unit cell. A complete diamond lattice can be constructed by stacking the unit cells.

has to be populated with electrons in a particular way known as sp^3 hybridization. Instead of the 4 electrons occupying the s, p_x, p_y, and p_z orbital they occupy the hybrid orbitals (linear combinations) formed from the s and p orbitals, i.e. filling the orbitals sp_1^3, sp_2^3, sp_3^3 and sp_4^3. It is this tetrahedral structure, along with the electron distribution and low atomic number which gives diamond its characteristic properties, including mechanical strength. For readers interested in an intuitive explanation for this strength, a good place to start is the article "Why diamond is very hard" by J.J Gilman, see Ref [23].

2.1.2 The Mechanical Strength of Diamond - In-depth

The mechanical strength of brittle crystalline materials can be quantified by the properties: ultimate strength (tensile, compression), different moduli (shear, Young's, bulk, flexural), hardness (scratch, indentation, rebound), fracture toughness, among others. Brittleness means that a material fractures with little to no elastic deformation and plastic deformation. In mechanical applications, brittle materials are used for their high ultimate compressional strength, however tend to be weak to tensile stress.

Single crystalline diamond is unfortunately prone to fracture along the $\langle 111 \rangle$ crystal plane. This weakness is caused by the properties of ideal diamonds and is furthermore enhanced by the inclusion of defects like voids, and larger microcracks

[24]. The intrinsic weakness of diamond has been investigated theoretically, and the study concluded with that the weakness is caused by, (1) the lower strength between the bonds, and (2) the lower energy between the bonds in this particular direction [25], which can also be imprecisely interpreted from the larger lattice planar distance of the $\langle 111 \rangle$ planes. In practice the mechanical failure of diamond is lower than the ideal case, and this is caused by the movement of dislocations in the crystal. It has been found that the movement of dislocations can be inhibited, by using the polycrystalline form instead of the singlecrystalline form.

Polycrystalline materials consists of small crystals adhering to eachother and oriented in different directions. Due to the random orientation of the crystals, dislocations have to deform the grains to transmit through the matrix, thus requiring higher stresses. An additional strengthening mechanism is through the deposition of defects on the grain boundary. The inclusion of defect which distorts the crystal lattice cause an increases the energy. Since the defects are able to diffuse throughout the crystal they tend to accumulate at the boundary leaving the interior and decreasing the energy of the system. Due to these two effects, the fracture toughness (i.e. the material's resistance to brittle fracture) generally increases with decreasing grain size, until a critical size is reached, in which the ability to store dislocations at the grain boundaries are reduced. This is true in ideal polycrystalline material, however inclusion of multiple phases and materials alter this relation. For example: this is not the case for polycrystalline diamond used in many industrial applications, see the review article, Ref [26]. These polycrystalline diamonds include cobalt binder to make it easier to synthesize. And, although the grain boundaries become strengthened by the random orientations of the grains, other effects associated with binders are dominating the value of the fracture toughness such that it ends up being reduced.

2.1.3 Growth and Nucleation

The first step in the growth process of any solid is nucleation. Nucleation can be caused by physical processes or chemical processes. Successful nucleation is driven by the supersaturation of nucleants. There are two kinds of nucleation, homogeneous nucleation and heterogeneous nucleation. Homogeneous nucleation occur when the production of the nucleants occur in uniform media. In heterogeneous nucleation the nucleants are catalyzed by interfaces.

Diamond growth consists of the crystals growing larger and may include renucleation. Renucleation is the formation of new nuclei. This cause new crystals

to grow ontop of the existing crystal layer. The competition between growth and renucleation lead to observered effects, such as grain size and growth twinning. Growth twinning is when two crystals of different orientation grow into eachother but end up sharing some of the same lattice points at the intersection. The twinning often cause more complex crystal shapes. In the case of a large growth rate and small renucleation rate, the crystals become large with a low amount of crystal twinning. And whenever the renucleation is high relative to the growth, the crystals are small with more complex and chaotic geometric shapes. If the renucleation rate is very high the crystals end up seeming more spherical due to the large amount of crystal intergrowth.

2.1.4 Diamonds Grown in Nature and Thermodynamic Stability

In nature, most diamonds grow in the earth's mantle at depths of 200 km where elemental carbon is subjected to high pressures and high temperatures ($P \approx 5$GPa, $T \approx 1400$K) [27]. At these pressures and temperatures, diamond is the most stable phase of carbon, which can be seen on the carbon allotrope phase diagram, see Figure 2.2. A phase diagram does not denote growth rates, only thermodynamic stability, and metastability. The metastability of materials refers to its ability to exist in a thermodynamically unfavorable state for a significant amount of time due to the low conversion rate to the more stable allotrope. Although not shown on the diagram, the metastability of diamond and graphite extends over large ranges both in pressure and temperature. This is apparent in diamond, as it is metastable at standard conditions ($P \approx 10^{-4}$GPa, $T = 300$K). Due to the large range in metastability of diamond, the phase diagram can be ignored when discussing diamond growth.

2.2 The Chemical Vapour Deposition Process

Chemical vapour deposition (CVD) is the process of growing coatings atomistically using chemical reactions. The growth process can be described by the following steps [31], and is illustrated in Figure 2.3:

1. The reactants are transported from the gas inlet to the reaction zone.

2. While in the reaction zone, additional chemical species are produced.

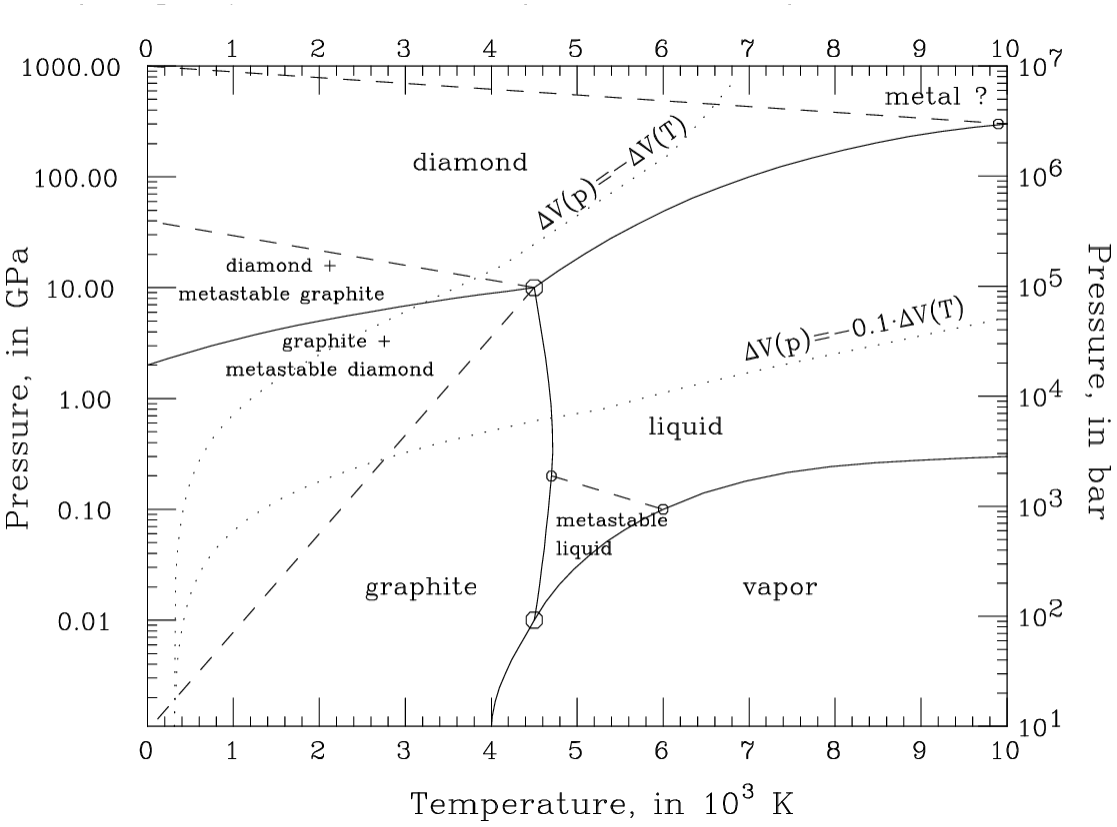

Figure 2.2: PT Phase diagram for carbon allotropes. Source: Ref [28], with data from references [29, 30].

3. The reactants and the products are then transported to the surface.

4. The species are adsorbed by the substrate.

5. The species then diffused into substrate.

6. While inside the substrate, the gas species chemically react, and the deposit is formed. During this reaction biproducts are also generated.

7. These biproducts diffuse out and into the surroundings from which they leave the system through the outlets.

The reaction that occurs at the surface (step 6), is usually not a single chemical reaction, it is usually multiple competing reaction paths, where each reaction is caused by gas kinetics. These different paths lead to the growth of different phases and materials. The reactions themselves depend on many parameters, like the properties of the substrate, among others, however the main factors which determines the growth is the density of different gas species as well as sufficient

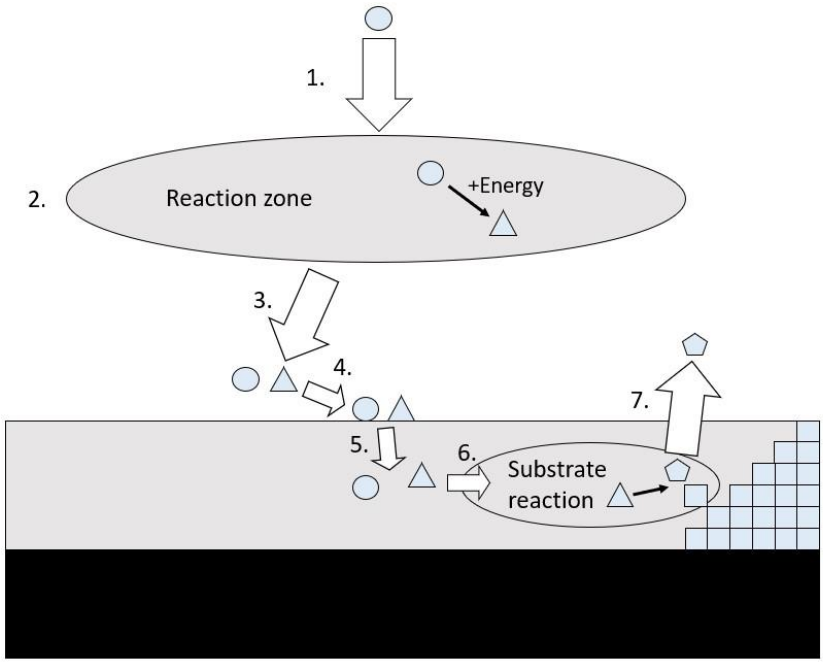

Figure 2.3: Fundamental steps in the chemical vapour deposition process. Recreated from Ref [31]. Step (1): The gas arrives from the gas inlet to the reaction zone. Step (2): The gas becomes activated forming volatile species. Step (3): The reactants and the products from the reaction zone diffuse/flow to the surface of the substrate. Step (4): The species becomes adsorbed by the substrate. Step (5): The adsorbed species diffuse into the substrate. Step (6): The species participate in chemical reactions resulting in a deposit. Step (7) The biproducts diffuse out of the substrate and leave the system through the outlet valve.

temperature at the surface. These parameters are especially influential on the reaction viability and the reaction rate.

CVD growth process is usually categorized by the gas activation technique. There are many different techniques for depositing diamonds using CVD, but the most common systems are Microwave Plasma CVD (MWP-CVD), and Hot Filament CVD (HF-CVD). Since the experiments done in this thesis only use MWP-CVD to grow diamond, only theory regarding MWP-CVD growth is covered.

2.3 Microwave Plasma Chemical Vapour Deposition of Diamond

Microwave plasma chemical vapour deposition (MWP-CVD), is an application of the CVD process which uses a microwave source to activate the gas from the

inlet. The key components of a MWP-CVD system are shown in Figure 2.4, more in-depth information regarding the designs can be found in [32]. The power transfer happens because electrons couple to the field and absorb the microwave power. The final temperature of the electrons is determined from the energy absorption from the field, and the heat dissipation with gas molecules. The heat dissipation, and various chemical reactions in the plasma is driven by collisions between the electrons (which have higher energy) and the gas molecules (which have lower energy). By keeping the system at non-equilibrium, i.e. keeping the electron temperature higher than the gas temperature, new volatile species can be created which would otherwise only be available at higher gas temperature [33]. Three temperatures are important for categorizing the deposition conditions: (1) electron temperature, (2) gas temperature, (3) substrate temperature.

Deposition of diamond at low temperatures allows growth on thermally sensitive materials. This is particularly interesting because new materials can be coated like glass and plastics. Additionally, there would be less delamination between the diamond layer and the substrate caused by differences in the coefficient of thermal expansion when the coating cools down after the deposition.

To grow diamond at low temperatures different methods can be used: (1) Lowering the input power, (2) lowering the pressure, (3) cooling the substrate directly (e.g. water cooling the substrate or substrate holder), (4) distancing the plasma from the substrate, and (5) pulsing the power source. However, the chemical reactions resulting in diamond growth is kinetically driven, thus when the temperature is reduced, the growth will eventually stop. For production of diamond films, the temperature of the substrate is usually held between $500°C$ and $1300°C$ while in a low pressure environments.

2.3.1 Growth Mechanism specific to CVD Diamond

The growth mechanism of diamond in CVD systems is complicated as it involves both gas phase chemistry and surface chemistry with many gas species being present. Other important properties are the temperature of the gas species, the chemical composition of the surface material, and the morphology of the surface material. Understanding what gas species contribute to the growth is a useful tool when optimizing deposition conditions at lower temperatures. The primary gas species and the reaction paths are shown in Figure 2.5.

Although much is unknown about the growth mechanism, investigations have concluded that the precursor (chemical compound initiating the reaction) is either

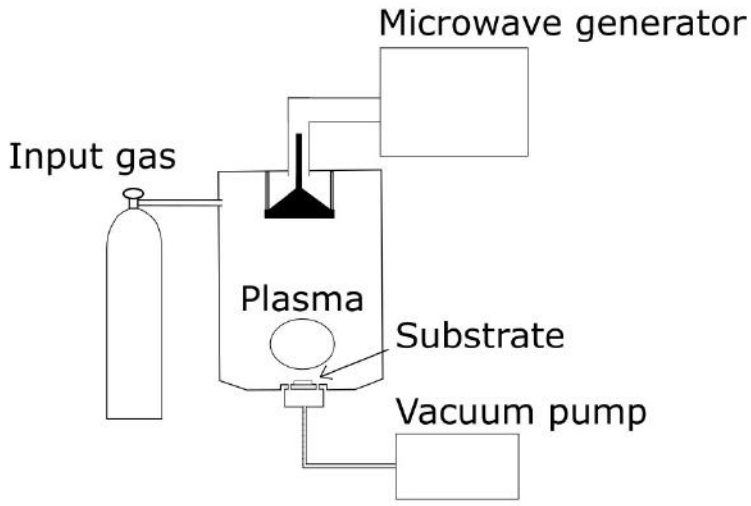

Figure 2.4: Key components of a MWPCVD system. Contains: a gas supply, microwave generator, reaction chamber, vacuum pump.

methyl CH_3 or acetylene C_2H_2, or both of them [36]. Butler *et al.* argued based on kinetics and spectroscopic data at different distances from the plasma, that the methyl radical is the species responsible for the growth [37]. Later experiments has shown that both methyl and acetylene environments can result in growth, however the nucleation rate and the crystalline quality is better for methyl environments compared to acetylene environments [38, 39].

The methyl radical, CH_3, was originally proposed by R. Mania, L. Stobierski, and R. Pampunch as the primary growth species [40]. M. Tsuda, M. Nakajima, and S. Oikawa in Ref [41] found out using quantum chemical calculations that growth by methyl insertion has the lowest energy path. Figure 2.6 shows the reaction path for diamond growth by the methyl radical. Recent growth rate simulations for CVD diamond assume methyl is the primary growth species [42].

M. Frenklach and K.E. Spear, from the article in Ref [43], proposed an alternative model, where atomic hydrogen initate the reaction from which acetylene reacts to form an extension to the diamond lattice. D. Huang, M. Frenklach, and M. Maroncelli updated this model based on semi-empirical quantum mechanical calculations using the Modified Neglect of Diatomic Overlap method (MNDO) [44]. This acetylene based growth model at lattice terrace sites is shown in Figure 2.7. M. Frenklach and K.E. Spear argued that the acetylene model is an improved model because acetylene and atomic hydrogen are more abundant species than methyl radicals, and could more easily explain the large growth rate observed in CVD diamond [43]. Additionally, D. Huang, M. Frenklach, and M. Maroncelli in their calculations using MNDO showed that the acetylene reaction path has a

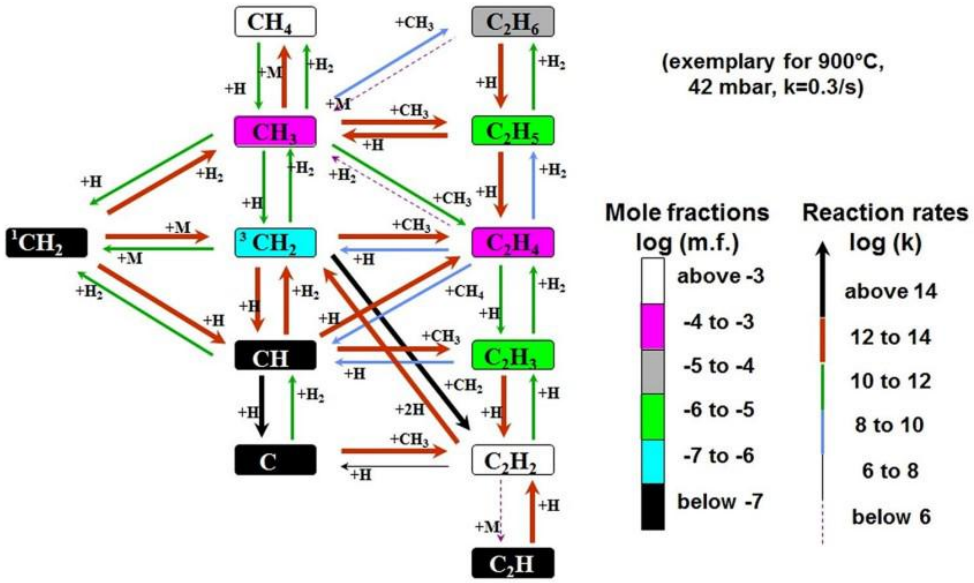

Figure 2.5: Reaction diagram and species population diagram of the most significant species partaking in the gas phase chemistry. The original calculations are from [34], and the image is from [35].

lower energy barrier than the reaction path of the methyl radical [44].

2.3.2 Carbon

A source of carbon is needed to grow diamond. Hydrocarbons are most commonly used, specifically methane CH_4. However other compounds can also be used as a carbon source like carbon dioxide or carbon monoxide [45, 22]. In systems with large concentrations of carbon, the deposit grows quickly and also forms either amorphous sp^3 bonded carbon or graphitic sp^2 bonded carbon [46, 47], as is shown in Figure 2.8. The increase in methane concentration also usually cause an increase in the diamond renucleation rate, as well as an increase in C-H bonds observed in the Raman spectrum [46].

2.3.3 Hydrogen

Hydrogen performs the role as the primary etchant of non-diamond material. At high electron temperatures the collisions between the hydrogen and the electrons splits the molecular hydrogen into two hydrogen atoms (also known as hydrogen radicals or atomic hydrogen). These hydrogen atoms are highly reactive, and preferentially attack non-diamond compounds both in the gas phase and those which are surface bonded. The preferential etching also includes graphite, long

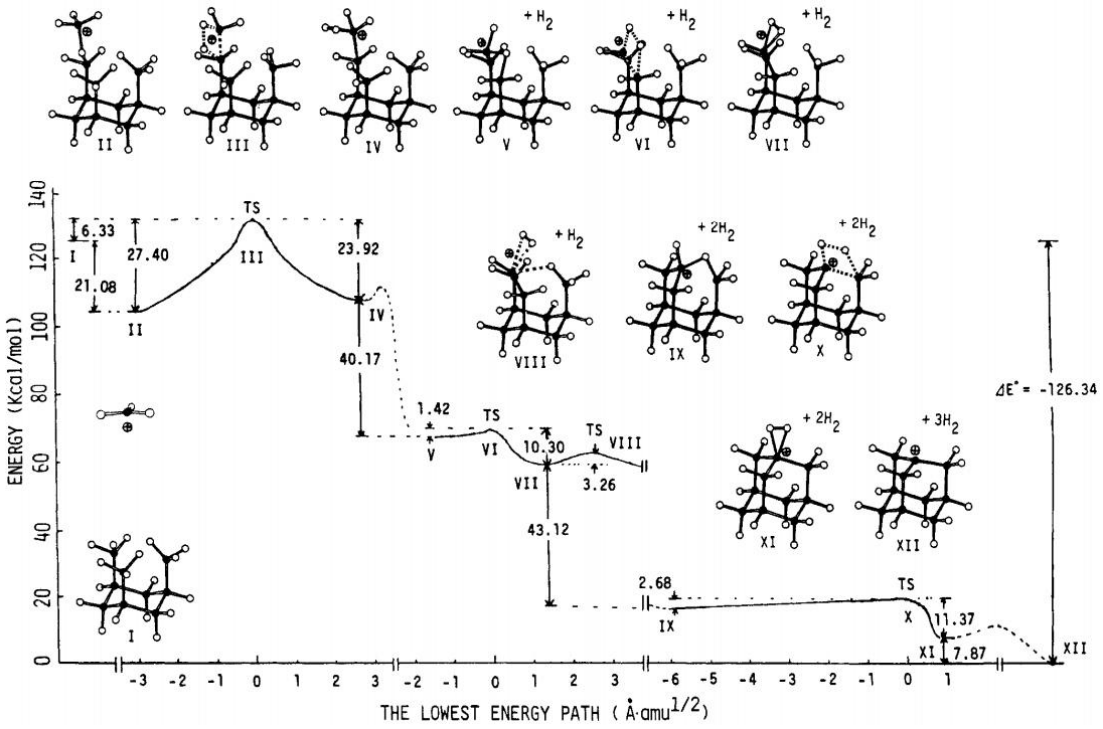

Figure 2.6: The growth mechanism of diamond when caused methyl radical. The diagram is created by [41], and is based on quantum chemical calculations and the lowest energy path for diamond growth. State I: Shows the initial state. The surface of the diamond lattice is terminated with hydrogen, and the methyl cation is located above the diamond lattice. State I→State II: Methyl cation attack the hydrogen terminated diamond surface. State II→State III: Carbon-carbon bond is forming. State III→State IV: Carbon-carbon bond is completed. State IV→State V: A hydrogen atom in the attached methyl cation attack a hydrogen atom in a neighboring hydrogen terminated group releasing hydrogen gas. Similar transitions as State I→State V happens two additional times releasing another two hydrogen molecules. State XII shows the original diamond lattice extended by one carbon atom.

chain polymers, and hydrogen terminated diamond surfaces. Additionally, it is well known that high hydrogen content is necessary for efficient growth of diamond, in the normal growth regimes where temperatures range between $500°C$ and $1300°C$ [36].

2.3.4 Oxygen

Oxygen radicals forms from oxygen containing compounds like O_2, CO_2, and CO. Oxygen radicals perform etching similar to hydrogen. However, oxygen is more active than hydrogen at lower temperature ranges due to having a lower activation energy. Additionally, oxygen suppress the incorporation of hydrogen in the films [49], and suppress acetylene generation due to increasing pyrolysis which then

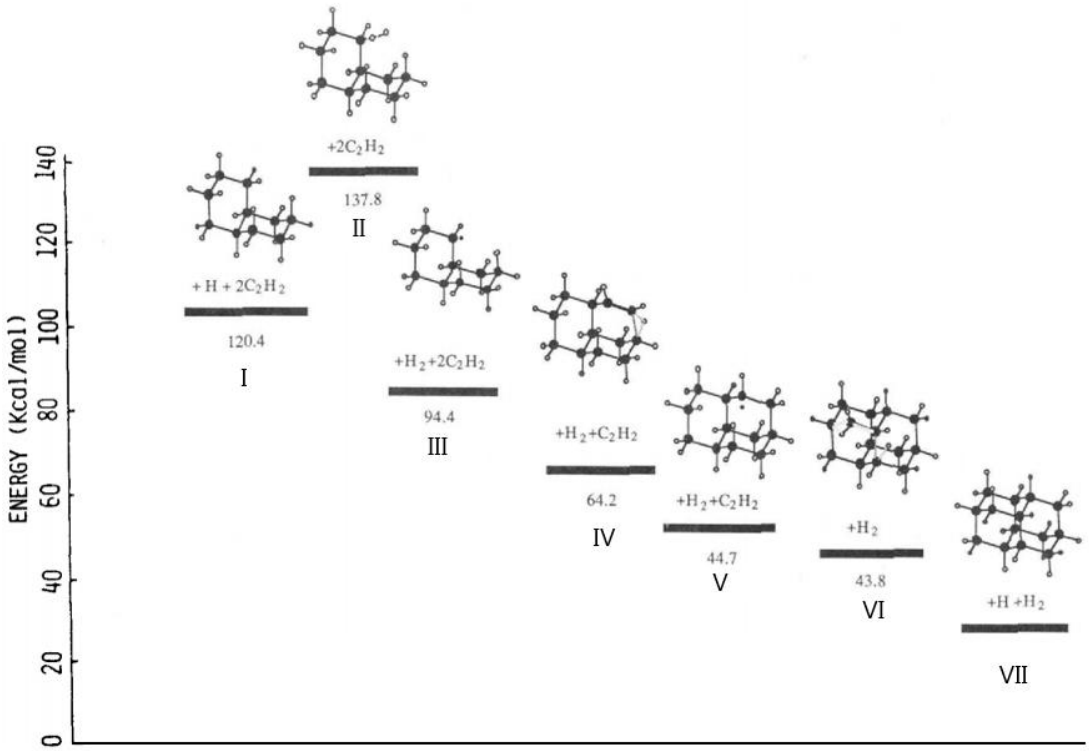

Figure 2.7: The growth mechanism of diamond when caused acetylene at a lattice terrace. The diagram is created by [44], and the path calculated using quantum mechanical calculations with the MNDO method. State I: Shows the initial state. The surface of the diamond lattice is terminated with hydrogen. State I→State II: Atomic hydrogen attack the hydrogen of the hydrogen terminated diamond surface. State II→State III: Hydrogen gas is released. State III→State IV: The acetylene insertion starts. State IV→State V: Acetylene insertion completes. State V→State VI: Another acetylene insertion starts. State IV→State VII: Acetylene insertion completes. State VII shows the original diamond lattice extended by one carbon atom.

increase the film quality [50]. The effect of oxygen on the morphology and film quality is shown in Figure 2.9.

2.3.5 Argon

The role of argon gas is to stabilize the plasma, increase the growth rate, increase the electron density [52], at the expense of film quality [53]. This decreased film quality constitutes an increase in sp^2 content and smaller diamond grain sizes. The gradual change in morphology at different argon contents is shown in Figure 2.10.

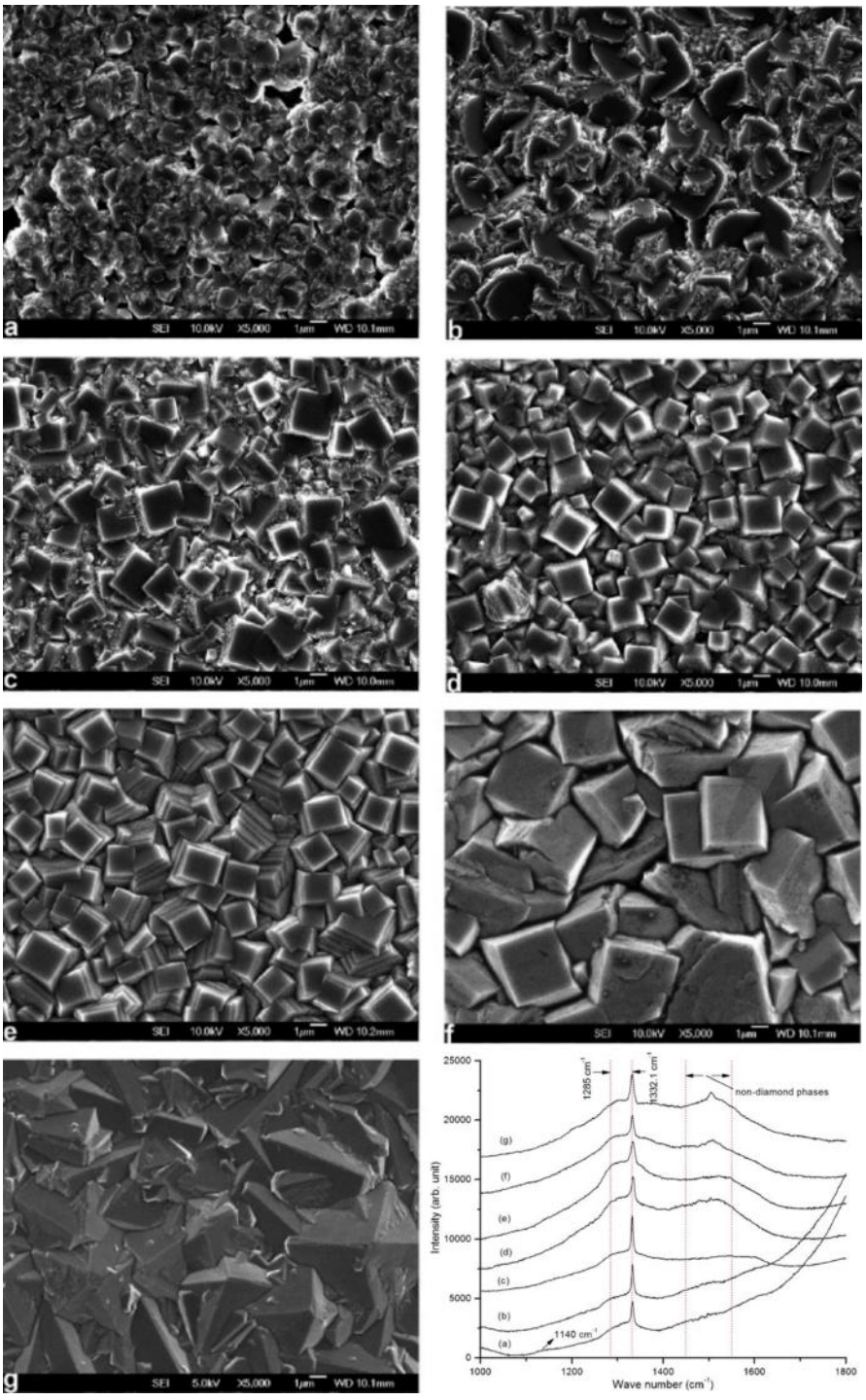

Figure 2.8: Chemical composition and structural morphology dependence on methane concentration, images from Ref [48]. At substrate temperatures T_{sub}=850°C and pressures p=80 torr. Methane concentrations (volume percent): (a) 0.5%, (b) 1.0%, (c) 1.5%, (d) 2.0%, (e) 2.5%, (f) 3.0%, (g) 3.5%. Raman spectra show the composition of the film. More information regarding Raman Spectra in section 3.

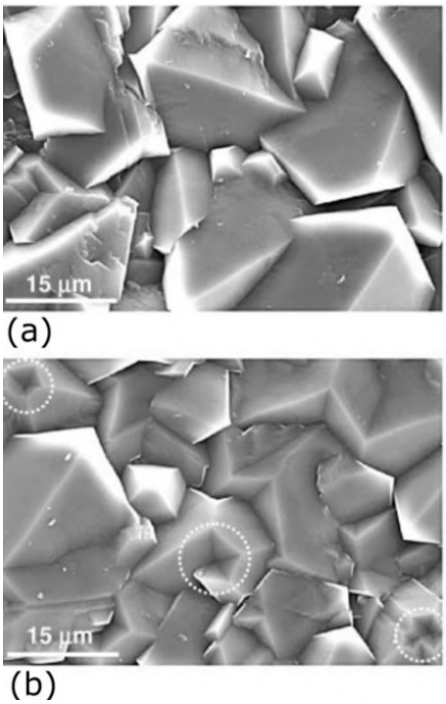

Figure 2.9: Influence of oxygen concentration on morphology, images from Ref [51]. At substrate temperatures T_{sub}=750°C and pressures p=105 torr, CH_4/H_2=4% (volume percent). O_2 concentrations (volume percent): (a) 0%, (b) 1.0%.

2.3.6 Nitrogen

Nitrogen is known to perform similarly to argon, however with some minor differences [19]. Nitrogen behaves differently in systems with oxygen present, compared to without oxygen. In oxygen free systems, nitrogen easily changes the morphology and composition of the deposit, even at low fractions as shown in Figure 2.11. However, in oxygen containing systems there is only a weak dependency between nitrogen concentration and morphology [54]. It is thus worth to note that leaks in the reactor can degrade film quality.

2.3.7 Substrate Temperature

The substrate temperature is an important parameter for growth. This is evident in how it affects deposit. Reduction of the substrate temperature reduces the growth rate, increases the defect concentration and increases the non-diamond phases [55]. Additionally, at lower substrate temperatures, hydrogen inclusions have reduced mobility which results in higher concentration of hydrogen inclusion inside of the bulk of the diamond grains, instead of forming concentrates at the grain boundaries [56].

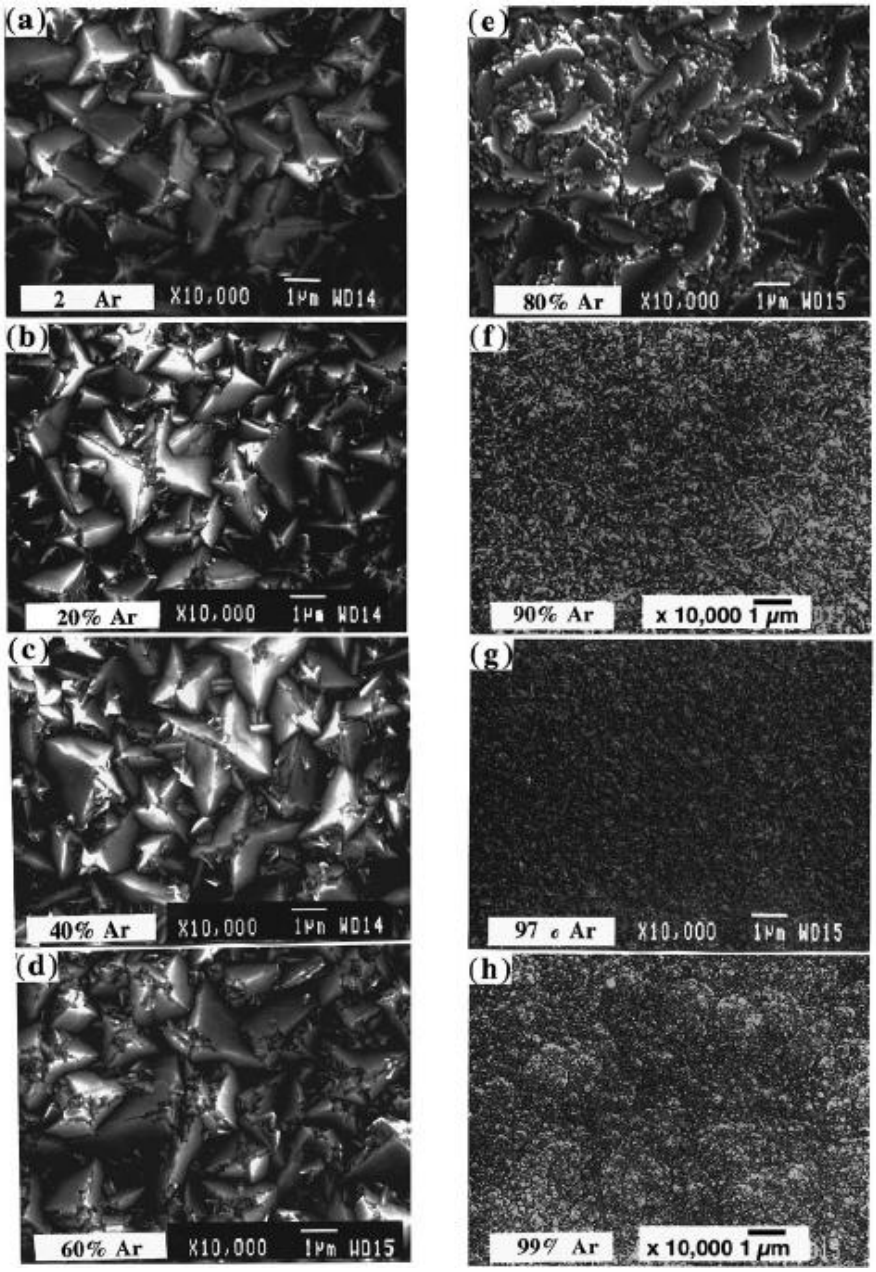

Figure 2.10: Influence of argon concentration on morphology, images from Ref [53]. At substrate temperatures T_{sub}=800°C and pressures p=100 torr, CH_4=1% (volume percent). Argon concentrations (volume percent): (a) 2%, (b) 20%, (c) 40%, (d) 60%, (e) 80%, (f) 90%, (g) 97%, (h) 99%.

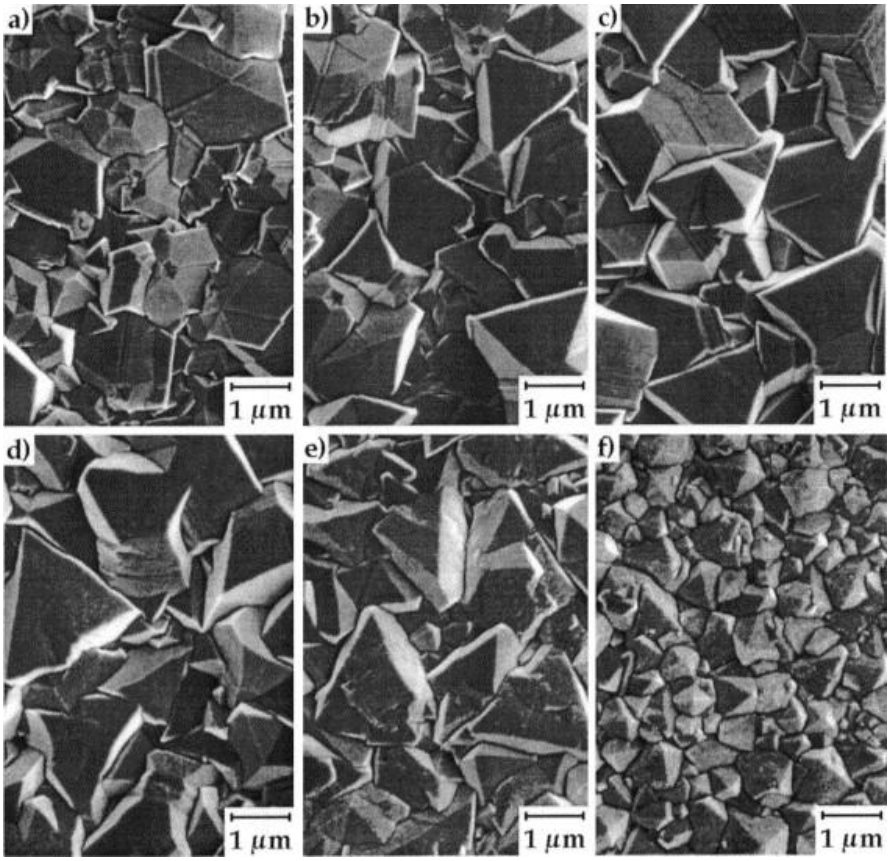

Figure 2.11: Influence of nitrogen concentration on morphology in oxygen free systems, images from Ref [54]. At substrate temperatures T_{sub}=515°C and pressures p=60 torr, CH_4=1% (volume percent). N_2 concentrations (ppm): (a) 0, (b) 34, (c) 58, (d) 94, (e) 340, (f) 930.

2.3.8 Microwave Power, and Pressure

The microwave power and the pressure is the primary method used to control the electron temperature and the gas temperature. Some systems also use the microwave power and the pressure as the main way to regulate the substrate temperature through electron-gas-substrate interactions. High microwave power is needed to achieve good film quality at high growth rates. This is because high power density is needed for high atomic hydrogen generation [32]. Pressure also has a strong effect on the temperatures in the system, since the amount of kinetic energy transfers between electrons and gas molecules increase with more particles. At low pressures, the electron temperature is large, meanwhile the gas temperature is low. At high gas pressures the energy transfer becomes more efficient and the electron temperature decreases meanwhile the gas temperature increases.

2.4 Modeling the Reactor Plasma

The model describing the MWP-CVD system is described in [57]. This model address the distribution of the electric field, the plasma, and the temperature, assuming [**Insert the assumptions of the model**]. The model contains coefficients which were determined in the original paper. The electric field is modeled by Maxwell's equation,

$$\boldsymbol{\nabla} \times \mu_r(\boldsymbol{\nabla} \times \boldsymbol{E}) - k_0^2(\epsilon_r - \frac{j\sigma}{\omega\epsilon_0})\boldsymbol{E} = 0 \tag{2.1}$$

where ϵ and σ is given by,

$$\epsilon_r = \begin{cases} 1 - \frac{\omega_p}{\omega^2+\nu_e^2}, & \in \Omega_p \\ 1, & \text{otherwise} \end{cases}, \qquad \sigma = \begin{cases} 1 - \frac{\nu_e\epsilon_0\omega_p^2}{\omega^2+\nu_e^2}, & \in \Omega_p \\ 0, & \text{otherwise} \end{cases},$$

and,

$$\omega_p^2 = \frac{e^2 n_e}{m_e \epsilon_0}.$$

The plasma distribution can be approximated by the electron distribution which itself is described by the equation,

$$\boldsymbol{\nabla} \cdot (-D_e \boldsymbol{\nabla} n_e) + R_{vr} n_e^2 + R_a n_e = R_i n_e \cdot (\boldsymbol{E}\boldsymbol{E}^*). \tag{2.2}$$

Lastly, the gas temperature is determined when combining heat transport equation (further discussed in Section **??**), and the heating caused by the electron collisions with the gas given by,

$$Q_p = \frac{e^2 v_e n_e \cdot (\boldsymbol{E}\boldsymbol{E}^*)}{2(\omega^2 + v_e^2)}, \qquad \in \Omega_p \tag{2.3}$$

The description of all the variables are listed below:

- k_0 is the wavenumber of the microwaves in vacuum.
- ω is the angular frequency of the microwaves
- j is the imaginary unit.
- e is the elementary charge.
- $\boldsymbol{E}$ is the complex electric field (vector).
- μ_r is the relative permeability
- ϵ_0 is the permittivity of vacuum.

- ϵ_r is the relative permittivity of the medium.
- σ is the conductivity of the medium.
- ω_p is the plasma frequency.
- ν_e is the electron collision frequency
- D_e is the ambipolar diffusion coefficient of electrons.
- n_e is the electron density.
- R_{vr} is the coefficient of electron recombination.
- R_a is the coefficient of attachment between electrons and neutral particles.
- R_i is the coefficient of ionization of gas molecules due to collisions with electrons.
- Q_p is the heat source arising from the plasma.
- Ω_p is the region of space where plasma is active.

2.5 Heat Transfer Models

Heat transfer models has to uphold the conservation laws of energy, mass, linear momentum, and angular momentum. These restrictions can be combined to form a single equation [58, 59], and the result is shown by equation 2.5. The starting point for this equation is the conservation of energy, i.e. the first law of thermodynamics. If a system is subjected to heat and work at a rate Q_{ext} and P_{ext} respectively, the energy will be distributed over the macroscopic internal energy E and the macroscopic kinetic energy K of the system Ω.

$$\frac{dE_\Omega}{dt} + \frac{dK_\Omega}{dt} = Q_{ext} + P_{ext} \tag{2.4}$$

By applying the remaining conservation laws, see Ref [58], equation 2.4 becomes,

$$\frac{dE_\Omega}{dt} = Q_{exch} + \int_\Omega (\boldsymbol{\sigma} : \boldsymbol{D}) dv \tag{2.5}$$

where $\boldsymbol{\sigma}$ is the Cauchy stress tensor, $\boldsymbol{D}$ is the strain rate tensor, and ":" is the contraction operator, which is calculated in the following way:

$$\boldsymbol{A} : \boldsymbol{B} = \sum_n \sum_m A_{nm} B_{nm}$$

Equation 2.5 still needs to translate the macroscopic terms E_Ω and Q_{exch}. Simple expressions can be derived for Q_{exch} and $\frac{dE_\Omega}{dt}$, however, these are also given in

the COMSOL user manual and will be skipped. Substituting terms, equation 2.5 becomes equation **??**, and is also known as the heat balance equation, which holds for both solids and for fluids. For solids the generalized heat balance equation takes the form,

$$??\rho C_p(\frac{\partial T}{\partial t} + \boldsymbol{u} \cdot \boldsymbol{\nabla} T) + \boldsymbol{\nabla} \cdot (\boldsymbol{q_c} + \boldsymbol{q_r}) = -\alpha T : \frac{dS}{dt} + Q \tag{2.6}$$

where ρ is the density, C_p is the specific heat capacity at constant stress, u is the velocity vector field for moving domains, α is the coefficient of thermal expansion, q_c is the heat flow caused by conduction, q_r is the heat flow caused by radiation, S is the second Piola Kirchoff stress tensor, and Q is any additional heat terms. Meanwhile for fluids the generalized heat balance equation takes the form,

$$\rho C_p(\frac{\partial T}{\partial t}\boldsymbol{u} \cdot \boldsymbol{\nabla} T) + \boldsymbol{\nabla} \cdot (\boldsymbol{q_c} + \boldsymbol{q_r}) = \alpha_p T(\frac{\partial p}{\partial t} + \boldsymbol{u} \cdot \boldsymbol{\nabla} p) + \tau : \boldsymbol{\nabla u} + Q \tag{2.7}$$

where α_p is the coefficient of thermal expansion, p is the pressure, τ is the viscous stress tensor.

2.5.1 Conductive Heat Transfer

Conduction is described by the law of heat conduction:

$$\boldsymbol{q_c} = -k\boldsymbol{\nabla} T \tag{2.8}$$

where k is the thermal conductivity and T is the temperature.

2.5.2 Radiative Heat Transfer

Radiative heat transfer is formulated as an exchange of fluxes by the walls in a cavity. The derivation is given in the COMSOL Multiphysics heat transfer manual [59]. The incoming radiative flux Φ_G from other places on the cavity wall, exchanges energy with the surface as well as diffusively scatters. The outgoing radiation is given by the sum of the diffusively scattered light and the emitted light from the heated surface.

$$\Phi_{out} = \Phi_{reflection} + \Phi_{emission} = \rho_d \Phi_G + \epsilon e_b$$

where ρ_d is the diffuse reflectivity, ϵ is the emissivity, and e_b is the radiated heat from a black body given by,

$$e_b = n^2 \sigma T^4$$

where n is the reflective index, and σ is Stefan-Boltzmann constant. By considering the amount of light entering the system by the flux denoted by the non-scattered fraction of the incomming light Φ_G, and the amount of energy leaving the system by the flux Φ_{out}, the heat entering the wall can be calculated from the difference:

$$q_r = \Phi_{in} - \Phi_{out} = (1 - \rho_s)\Phi_G - \rho_d \Phi_G - \epsilon n^2 \sigma T^4 \tag{2.9}$$

where ρ_s is the specular reflectivity.

2.5.3 Convection

In a system where the heat source is located above a cold sink, the convective flow will be hindered due to the formation of a stable thermal boundary. This thermal boundary is stable since heated gas will be less dense and float ontop from where it will be heated further, and the colder and denser gas will remain on the bottom and be cooled further. It is assumed that convective heat transfer is not a significant contributor to heat transfer.

Chapter 3

Characterisation Techniques

The characterisation techniques used in the experiments were Raman spectroscopy and scanning electron microscopy (SEM). Temperature measurements were also important for categorising the samples. Two types of thermometers were used to measure the temperature being thermocouples and pyrometers.

3.1 Raman Spectroscopy

Raman spectroscopy is a spectroscopic technique used to determine the chemical composition of a sample as well as other features such as the grain size of polycrystalline materials. To do Raman spectroscopy, a Raman spectrometer is used. The Raman spectrometer used for the characterisation of the samples is shown in Figure 3.1. Raman spectroscopy is based on the phenomena known as Raman scattering. Raman scattering happens when an incident photon with a particular wavelength (known as the excitation wavelength) is scattered at a different wavelength. It is an inelastic two-photon scattering process where the energy from the incident photon is transferred to a molecule such that the molecule's vibrational state change [60]. Which means that the scattered light can give information regarding structure and the chemical composition. By comparing the Raman spectra of the unknown sample to reference spectra, the chemical composition and structure can be inferred.

To obtain the Raman spectra, the light emanating from the sample is first filtered such that non-Raman scattered light is removed. After the filter the light hits a diffraction grating, which splits up the light at an angle depending on the wavelength. The larger wavelengths diffracts at a larger angle than short wavelengths. Thus, the intensity versus wavelength distribution can be measured using a CCD. The wavelength-intensity relationship is plotted as a function the Raman shift ν, which is directly related to the wavelength through the equation,

$$\nu = \frac{1}{\lambda_e} - \frac{1}{\lambda_r}$$

where λ_e is the excitation wavelength, and λ_r is the wavelength of the Raman scattered light.

Typical Raman spectra for different carbon allotopes is show in Figure 3.2. The different peaks which are typically found in nanocrystalline diamond is shown in Table 3.1. The most important peak of nanocrystalline diamond films is the diamond peak. The characteristic peak for pure diamond is usually found at 1332 cm^{-1}, with a narrow full width at half maximum (FWHM). The peak position may vary depending on the temperature during the deposition, the sample heating during the Raman spectroscopy, the grain size, and non-hydrostatic stress [61, 62]. Due to these effects, the diamond peak in nanocrystalline diamond is found ranging between 1290-1350 cm^{-1}, with a FWHM ranging between of 1-20 cm^{-1} [62, 63]. The FWHM of diamond is increased whenver the disorder of the sp^3 bonded carbon is increased, as well as whenever the crystal sizes are decreased (of pure diamond domains, i.e. phonon confinement) [62]. The review article on Raman signatures from carbon allotropes by A.C. Ferrari and J. Robertson, see Ref [64], elucidates the nature of the D peak and the G peak. First, the D peak and G peak is only associated to sp^2 sites. Second, the G peak is caused by the stretching of sp^2 carbon in carbon chains and carbon rings. Third, the D peak is caused by breathing modes in sp^2 carbon only found in carbon rings.

The full Raman spectrum of diamond is discussed by Zaitsev in [62]. Some of the additional features not addressed in Table 3.1 but discussed by Zaitsev and are listed below:

- Peak 1140-1200cm^{-1}, FWHM 30-200 cm^{-1}: Found in low-quality CVD diamond films. Is thought to be caused by stretching vibrations of C-C bonds in hydrogenous polymers.
- Peak 1166-1300 cm^{-1}, FWHM 150 cm^{-1}: Found in diamond produced by the MWP-CVD method.
- Peak 1420-1440 cm^{-1}, FWHM 100 cm^{-1}: Found in low temperature CVD growth of diamond films using oxygen. Is thought to be caused by microtwinned regions.
- Peak 1475-1564 cm^{-1}, FWHM 80-220cm^{-1}: Is thought to be caused by sp^2 inclusions in diamond crystals.
- Peak 1500 cm^{-1}, FWHM 350-500 cm^{-1}: Found in low-quality CVD diamond. Is thought to be caused by amorphous carbon, or sp^2 carbon clusters.
- Peak 1600-1620 cm^{-1}, FWHM 20-30 cm^{-1}: Found in CVD diamond films after laser ablation. Is thought to be caused by amorphous carbon, micro-

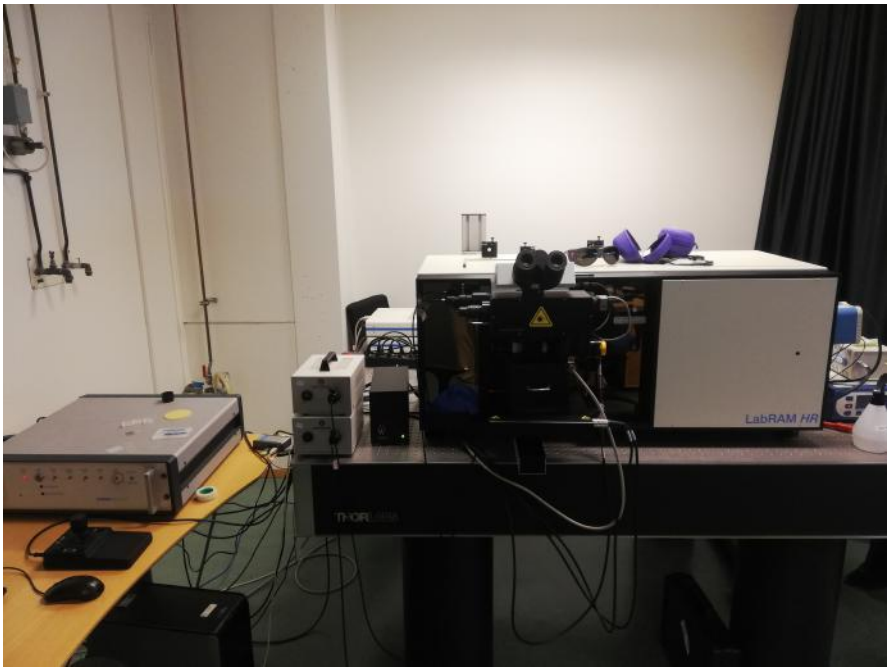

Figure 3.1: The Raman spectrometer used for the characterisation of the nanocrystalline diamond coatings. The light source of the Raman spectrometer is an Ar-ion laser with the excitation wavelength 488 nm.

crystalline graphite, or hydrogentated sp^2 bonded carbon.

- Peak 1730, FWHM 70 cm^{-1}: Is caused by stretching vibrations of C=O bonds.

3.2 Scanning Electron Microscopy

A scanning electron microscope (SEM) images a sample by scanning the surface with an electron beam. The source of the electrons is an electron gun, either driven thermionically or by field emission. The electrons are then accelerated by an acceleration voltage, and passed through magnetic lenses. The focused electron beam hits the sample and electrons are produced. These electrons are measured with an electron detector. The most common is the Everhart-Thornley detector, which is a scintillator combined with a photomultiplier. The strength of the signal from the detector is then related to how many electrons arrive. An image can then be made, using the spatial coordinates of the scanning beam, and the signal intensity as the coloring. The characteristic crystal shapes of nanocrystalline diamond in SEM images are shown in Figure 3.3. The intermediate stages between the $\langle 111 \rangle$ crystals and the $\langle 100 \rangle$ crystals are shown in Figure 3.4.

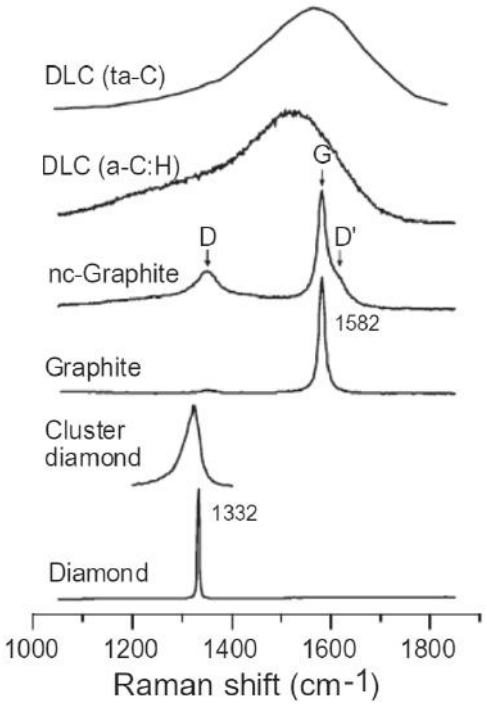

Figure 3.2: Typical Raman spectra from different allotropes of carbon. Image from [65]. DLC is amorphous carbon and exists in hydrogenated variants, and nonhydrogenated variants. D' peak is the second order peak associated with the first order D peak. NC stands for nanocrystalline. Cluster diamond is the same as nanocrystalline diamond.

Table 3.1: Characteristic peaks in the Raman spectra of nanocrystalline diamond. Values from [63, 66]. Full width height at half maximum (FWHM). There are additional peaks also observed in the spectrum for nanocrystalline diamond. However, those peaks are less common. These additional peaks are described in the bulleted list at the end of section 3.1.

Position [cm^{-1}]	FWHM [cm^{-1}]	Assignment
1100-1150	40-80	Transpolyacetylene
1290-1350	1-40	Diamond
1350	80-400	D peak
1430-1470	80	Transpolyacetylene
1520-1610	40-200	G peak

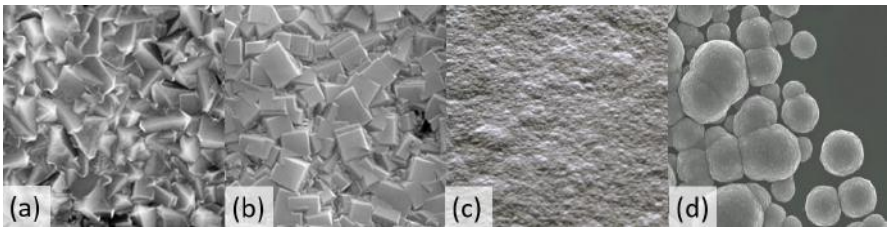

Figure 3.3: Common morphologies found in nanocrystalline diamond coatings. (a) $\langle 111 \rangle$ crystals [67], (b) $\langle 100 \rangle$ crystals [67], (c) smooth [68], (d) ballas [68].

Figure 3.4: Intermediate crystal shapes between the $\langle 111 \rangle$ shape and the $\langle 100 \rangle$ shape [69].

3.3 Temperature Measurement

Having an accurate temperature measurement is the most important aspect of the synthesis. Two pyrometers and a thermocouple were used to measure the temperature of different parts of the system.

3.3.1 Pyrometer

A pyrometer is a device which measures and analyzes the outcomming radiation from a hot surface, such that the temperature can be determined. Pyrometers have high precision, but may suffer from systematic errors if not calibrated correctly and recently. Another limiting factor for pyrometers is attaining a sufficient signal.

An investigation of two pyrometers was completed by Dr. Justas Zalieckas of the University of Bergen. The investigation looked at the Raytek E2R pyrometer and the Landmark M1 1100/2900F-V pyrometer. The Raytek pyrometer was calibrated recently, meanwhile the Landmark has not been calibrated recently. The result illustrates the inconsistency between pyrometers when not calibrated. This error is shown in Table 3.2. The equation for the measurement uncertainty for the Raytek pyrometer assuming no attenuation is:

$$u(T_{Raytek}) = \frac{0.5}{100} T_{Raytek} + 2°C \tag{3.1}$$

where the measured temperature from the pyrometer is T_{Raytek}. The equation for the measurement uncertainty for the Landmark pyrometer is:

$$u(T_{Landmark}) = \frac{0.4}{100} T_{Landmark} \tag{3.2}$$

where the measured temperature from the pyrometer is $T_{Landmark}$. Pyrometer measurements in this thesis were also completed using the Landmark M1 1100/2900F-V pyrometer and the Raytek E2R pyrometer. The Raytek pyrometer was not available during the first few depositions and was only used when the temperature reached the lower limit of the Landmark pyrometer. The lower limit of the Landmark pyrometer is $600°C$, meanwhile the lower limit of the Raytek pyrometer is $250°C$.

Table 3.2: Difference in measurement between two pyrometers. The surface was measured with the pyrometers. The center of the body was measured with a thermocouple to be equal to $789°C$.

Emissivity	Raytek E2R	Landmark M1 1100/2900F-V
0.1	$(990 \pm 7)°C$	$(935 \pm 4)°C$
0.2	$(990 \pm 7)°C$	$(935 \pm 4)°C$

3.3.2 Thermocouple

A thermocouple is a temperature measuring device. A thermocouple works by measuring the voltage difference between two metal junctions, one located at a known temperature, and another junction located at the position where the temperature is to be measured. Since the voltage difference is temperature dependent, the temperature can easily be attained. There are different kinds of thermocouples which uses different metals for the junction. The thermocouple used in the temperature measurement was a K-type (chromel/alumel) thermocouple. The benefit of this thermocouple type is that it can give accurate temperature measurements over a wide range of temperatures. The equation for the measurement uncertainty for the thermocouple is:

$$u(T_{Thermocouple}) = \begin{cases} \frac{0.75}{100} T_{Thermocouple} & \text{if } T_{Thermocouple} > 293°C \\ 2.2°C & \text{otherwise} \end{cases} \tag{3.3}$$

The thermocouple is installed internally in the sample holder, with the contact point $(12 \pm 2)mm$ off center of the stage (symmetry axis) and $(0.15 \pm 0.05)mm$ underneath the surface of the sample holder. An alternative to this approach is to weld the thermocouple to the substrate. This would give an accurate temperature measurement, but would be cumbersome whenever installing new samples. Since the thermocouple is mounted inside the stage and not ontop, the temperature measurement of the thermocouple cannot be directly compared with the values from the pyrometer.

Chapter 4

Methods - Experiment

This chapter gives an overview of the methods used for the experiments. The MWP-CVD reactor used for the deposition is shown in Figure 4.1. The principles on which the reactor works are described in chapter 2. The reactor is built by co-supervisor Justas Zalieckas according to his own patented (REF) design. Because the instrument is home built, no manual was available. A user manual was written as a part of this thesis work and can be found in appendix A.

Figure 4.1: Microwave power chemical vapour deposition (MWPCVD) reactor. Further information of all the components are given in the user manual found in the appendix.

Three types experiments were carried out. The first type experiment use typical deposition parameters (pressure and gas composition) used previously by the

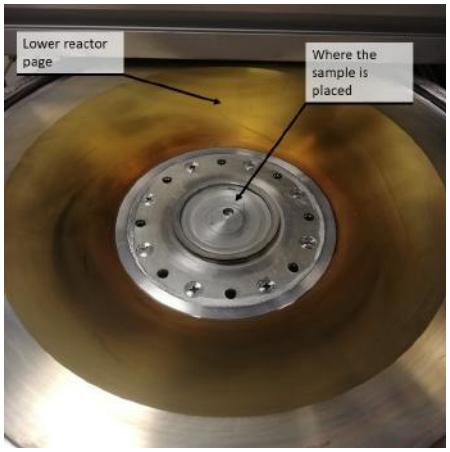

Figure 4.2: The stage setup for experiment 1: the substrate is placed in the reactor with nothing covering it. During the deposition the substrate is directly exposed to the plasma.

Table 4.1: Deposition parameters for experiment 1.

Parameter	Value
Pressure	100 torr
Flow rate(H_2)	(453 sccm, 96%)
Flow rate(CH_4)	(19 sccm, 4%)

co-supervisor Justas Zalieckas. The next type of experiment uses the same deposition parameters, but with a different stage configuration which may allow for even lower temperature deposition. Based on the result of these two types of experiments, the best stage configuration will be found. The last experiment use the best stage configuration with new deposition parameters more suited for low temperature growth. For all these types of experiments, the first sample is deposited at high temperatures, and every subsequent sample has the power adjusted such that the thermocouple readout value is decreased by $25°C$ or $50°C$. The temperature is reduced until no diamond growth is observed during the characterisation.

4.1 Experiment 1: Typical Deposition Parameters Without Protective Lid

This experiment establishes a standard with which the other two experiments can be compared. The deposition parameters are given in Table 4.1, and the stage setup is shown in Figure 4.2. The temperature readout from the pyrometer is measured from the substrate.

4.2 Experiment 2: Typical Deposition Parameters With Protective Lid

The purpose of the new stage configuration is to reflect the electromagnetic waves before they hit the substrate. The lid design similar to the Faraday cage on a microwave oven. The reasoning is that the temperature distribution follows the electric field distribution, as expressed by equation: 2.1, 2.2, and 2.3. The lid will be able to form a larger temperature gradient due to the reflection of the electromagnetic waves. The plasma can then be excited at higher input power producing more growth species for an equal amount of substrate heating. Thus the shielding effect of the lid will allow diamonds to be grown at lower substrate temperatures. The deposition parameters are the same as experiment 1 (see Table 4.1), and the stage setup is shown in Figure 4.3a. A close up image of the lid is shown in Figure 4.3b.

When the pyrometer measures the temperature of the protective lid, it has to be aimed off the center of the lid shown as in Figure 4.3b. This is because aiming it at the center does not give consistent measurements, i.e. doing many measurements in succession gives a large spread in temperature values. Certain times it also gives no temperature measurement due to insufficient signal. To work around this issue, the pyrometer is aimed off the center. By aiming the pyrometer measurement spot off-center similar to what is shown on Figure 4.3b, the temperature measurements become easier to do.

4.3 Experiment 3: Optimizing the Gas Composition

The purpose of this experiment is to test different sets of gas mixtures and see what mixture provides the best results at low substrate temperatures. The result from experiment 1 and experiment 2 showed that the best stage design was using no protective lid. The first deposition parameters tested for low temperature MWP-CVD are given in Table 4.2. The values are based on the results from reference [70]. The pressure is lowered from 100 torr to 50 torr such that the electron temperature is increased, while at the same time reducing the gas temperature. This allows the gas molecules to be ionized at lower substrate temperatures.

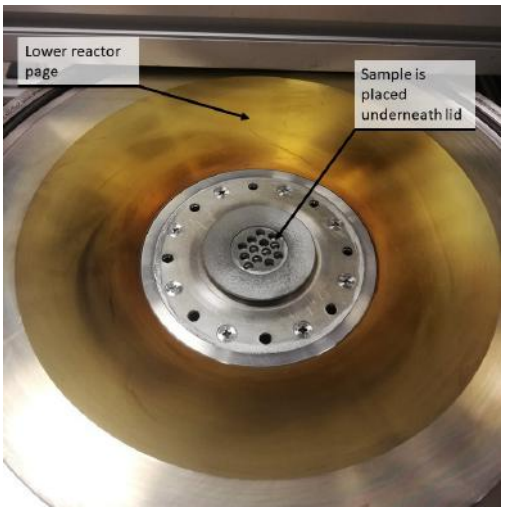

(a) The stage setup for experiment 2: the substrate is placed in the reactor with a protective lid covering it. During the deposition the substrate is behind the lid, only being exposed through the holes in the lid.

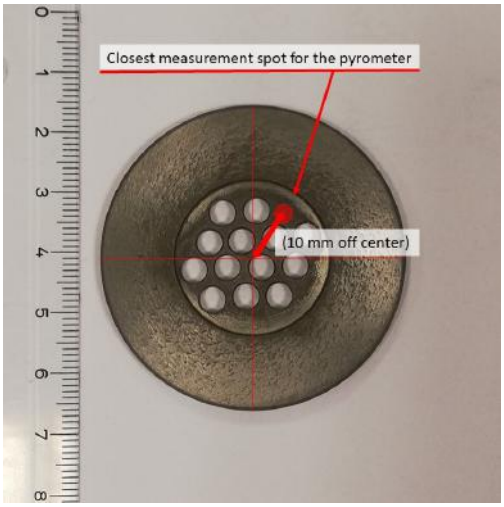

(b) The pyrometer has to measure the temperature of the lid off-center. This is because it is difficult to aim in the pyrometer. The pyrometer may measure from top of the lid or from inside the holes, and in many cases will give no temperature measurement due to insufficient signal. The intersection of the two red lines shows the center of the lid. The distance between the measured spot and the center of the lid is approximately $(10 \pm 2)mm$.

Figure 4.3

Table 4.2: The first deposition parameters to test. The result from this deposition determines any new deposition parameters.

Parameter	Values of Set 1
Pressure	50 torr
Flow rate(H_2)	(235 sccm, 94%)
Flow rate(CH_4)	(10 sccm, 4%)
Flow rate(CO_2)	(5 sccm, 2%)

Chapter 5

Methods - Simulation

This chapter gives an overview of the methods used for the simulations. All simulations were done using COMSOL Multiphysics®. The purpose is to estimate the substrate temperature using the thermocouple temperature, for the cases when the substrate temperature is not directly measurable, i.e. when the lid is covering the substrate, and when the signal intensity is too low to get a readout. Two simulations were considered. Simulation 1 estimates the electric field distribution, electron distribution, and the gas temperature distribution within the reaction chamber. Simulation 2 estimates the heat distribution throughout the metal stage.

5.1 Description of the Simulation Setup: Electric Field Distribution, Electron Distribution, and the Gas temperature distribution

Simulations were done for a flat stage and a flat stage covered with a lid, these simulations corresponds to experiment 1 and experiment 2 from last chapter. The 3D models were created by Dr. Justas Zalieckas and is shown in Figure 5.1. The stage without a protective lid, is shown in Figure 5.1a. The stage with the protective lid, is shown in Figure 5.1b. The coaxial port for the microwaves are the same for both the stage designs, and the port location is shown in Figure 5.2a. Boundary conditions regarding temperature are also placed on metal walls and the stage which acts like heat sinks. There are two separate boundaries: the first being the reactor wall and most of the lower stage, and the second domain being the center of the sample stage where the substrate is placed. These two domains are shown in Figure 5.2b.

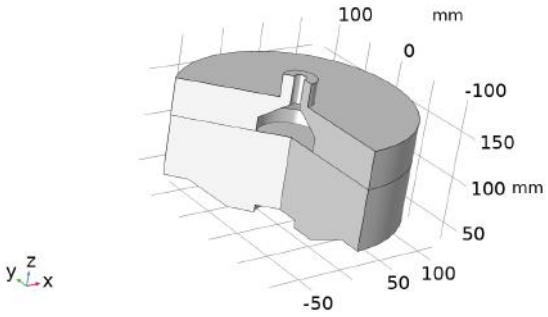

(a) A cake slice of the COMSOL 3D model showing the reactor cavity when no protective lid is installed.

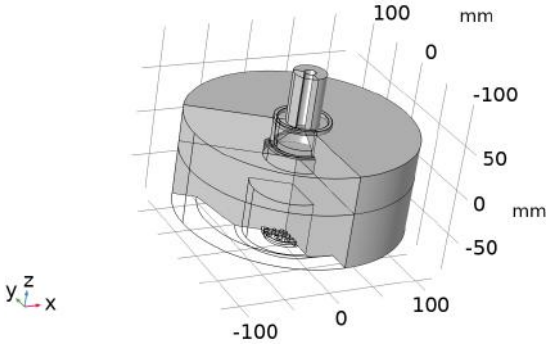

(b) A cake slice of the COMSOL 3D model showing the reactor cavity when the protective lid is installed. The small holes at the bottom of the 3D is the holes in the lid allowing gas diffusion. The holes used in this model is not an exact copy of the real lid seen in Figure 4.3b.

Figure 5.1: Simple COMSOL models of the reactor chamber used for simulating plasma physics.

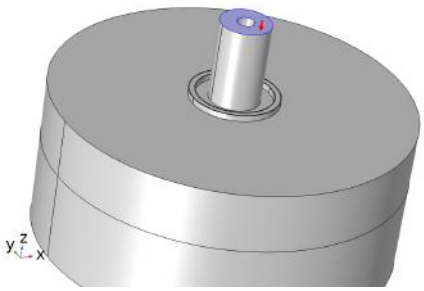

(a) The microwave port, i.e. where microwaves enter the reactor chamber. Unlike Figure 5.1a and Figure 5.1b, this does not show a cake slice, but the whole reactor when enclosed.

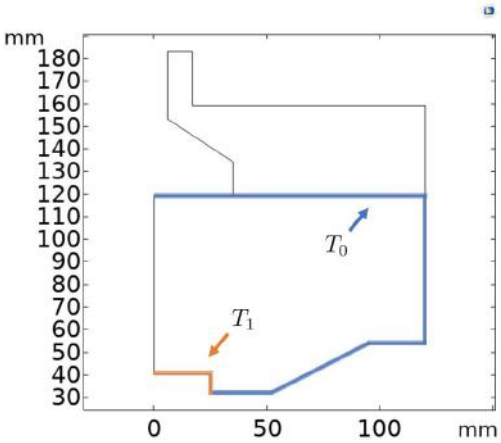

(b) The boundary conditions set at the reactor walls, and the sample stage. The boundary where the temperature is set to T_0 (i.e. the reactor wall and parts of the sample stage) is shown in blue. The boundary where the temperature is set to T_1 (i.e. the central sample stage which is close to the plasma) is shown in orange.

Figure 5.2: Simple COMSOL models of the reactor chamber used for simulating plasma physics.

5.2 Description of the Simulation Setup: Heat Transfer in Metal Stage

COMSOL Multiphysics® was used for simulating the temperature distribution throughout the sample stage. Simulations are done for two different stage setups. The 3D models were created by Dr. Justas Zalieckas, with minor adjustments to the geometry by the author. The cross-section of the 3D models are given in Figure 5.3. The stage without a protective lid is shown in Figure 5.3a. The stage with the protective lid is shown in Figure 5.3b.

The source of heat for the system is a time-independent temperature distribution on the topmost element for both stage setups. For the stage setup without the lid, the top of the substrate is held at a constant, elevated temperature, see Figure 5.4a. Similarly for the stage setup with the protective lid, the top is held at an elevated temperature, see Figure 5.4b.

The heat source in the model is supposed to represent the effect of plasma heating of the sample stage. The temperature value for this heat source is set to the measured temperature values from the pyrometer. The heat sink for both the stages are a fixed temperature boundary condition set to a lower temperature shown in Figure 5.5a and Figure 5.5b. The temperature of the heat sink is set to be equal to temperature of the water cooler measured during the deposition, which measures a temperature around 18 °C. The simulation procedure has the following steps to obtaining estimates for the substrate temperature:

1. Using the temperature data from experiment 1 (no protective lid): Create a model which predicts the temperature of the thermocouple using the measured temperature from the pyrometer as an input. Since both the temperature of the thermocouple and the pyrometer are known, the model can be tested and iteratively improved. The process of iteratively improving the model is discussed in Chapter 7.

2. Create an additional model for the experiment 2, which uses a protective lid for the substrate: In this case the model is expanded such that the air cavity between the protective lid and the substrate is taken into account. The input for this model is the temperature value from the pyrometer measured at the lid, and the model is tested by observing if the model predicts the correct value of the thermocouple. The process of iteratively improving the model is discussed in Chapter 7.

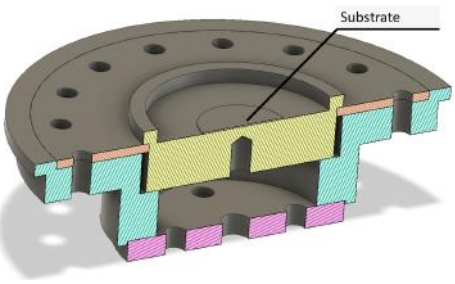

(a) Cross-section of stage setup without the protective lid.

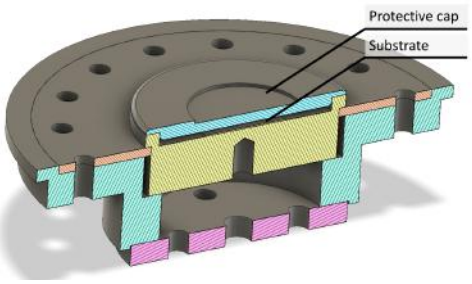

(b) Cross-section of stage setup with the protective lid. The lid used in this model does not include the holes found in the real lid, see Figure 4.3b.

Figure 5.3: Cross-section of the sample stages.

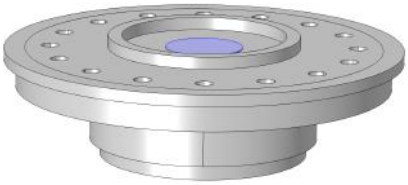

(a) Source of heat in the setup without the protective lid: Boundary with blue hue is held at a constant, elevated temperature.

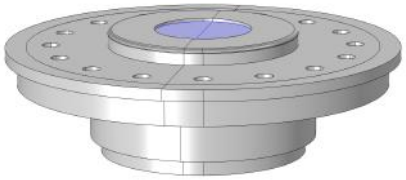

(b) Source of heat in the setup with the protective lid: Boundary with blue hue is held at a constant, elevated temperature.

Figure 5.4: The source of heat for the two stage setups is a constant temperature boundary condition held at the top element. Note that "constant" means in this specific case: $\partial T_{boundary}/\partial t = 0$.

3. Use the best models for the lid and without the lid to estimate the substrate temperature whenever, the substrate temperature is unknown.

The material properties used in the simulation are attained from the COMSOL material library. The materials used in the simulations are: molybdenum for the sample stage, silicon for the substrate, and hydrogen gas for the cavity present in stage setup with the protective lid. Hydrogen gas is used because it is the primary gas species. The pressure of the hydrogen gas is set to a pressure of 100 torr.

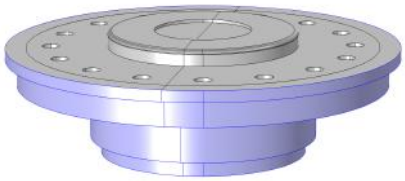

(a) Heat sink for both setup A and setup B: Boundary with blue hue is held at a constant and low temperature. Perspective from the top.

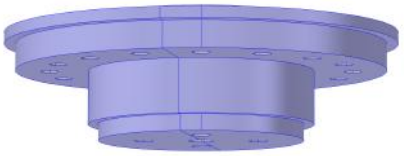

(b) Heat sink for both setup A and setup B: Boundary with blue hue is held at a constant and low temperature. Perspective from the bottom.

Figure 5.5: The heat sink for the two stage setups is a constant temperature boundary condition held at the far ends of the stage. Note that the temperature distribution is constant in terms of time and space along this boundary.

Chapter 6

Results and Discussion - Experiment

This chapter presents the results and the discussion from the experiments. The chapter is composed of three sections: (1) testing how low the temperature can be reduced with a conventional setup, (2) testing how low the temperature can be reduced when using a protective lid for the substrate, (3) testing how low the temperature can be reduced when introducing O_2 into the gas mixture. The nanocrystalline diamond films were deposited on diamond seeded silicon wafers by Paulius Pobedinskas at Hasselt University. The silicon wafers were spin coated with a nanodiamond solution with grain sizes ranging between 5-7 nm. SEM images of the seeded wafers are shown in Figure 6.1a. The particles visible in Figure 6.1 are agglomorates, evident from the size measurements shown in Figure 6.1b.

6.1 Experiment 1: Typical Deposition Parameters Without Protective Lid

This experiment investigates a typical gas composition using the standard MWP-CVD method. The stage setup for the reactor is shown Figure 4.2, and the parameters were: 96% hydrogen (453 sccm), 4% methane (19 sccm), p=100 torr. Due to time constraints, the experiment had to conclude before the lowest temperature was found. In total seven different samples were grown using different substrate temperatures. The temperature readouts for all samples are given Table 6.1, and the SEM and Raman spectra are given in Figure 6.2.

From Table 6.1, it is evident that there is a linear relationship between the temperature measured by the thermocouple and by the pyrometer. This linear relationship is plotted in Figure 6.3. The substrate temperature was evaluated by extrapolation. The uncertainty of the extrapolation was determined using the two end-points in the data set, being E1-1 and E1-5. The extrapolated values

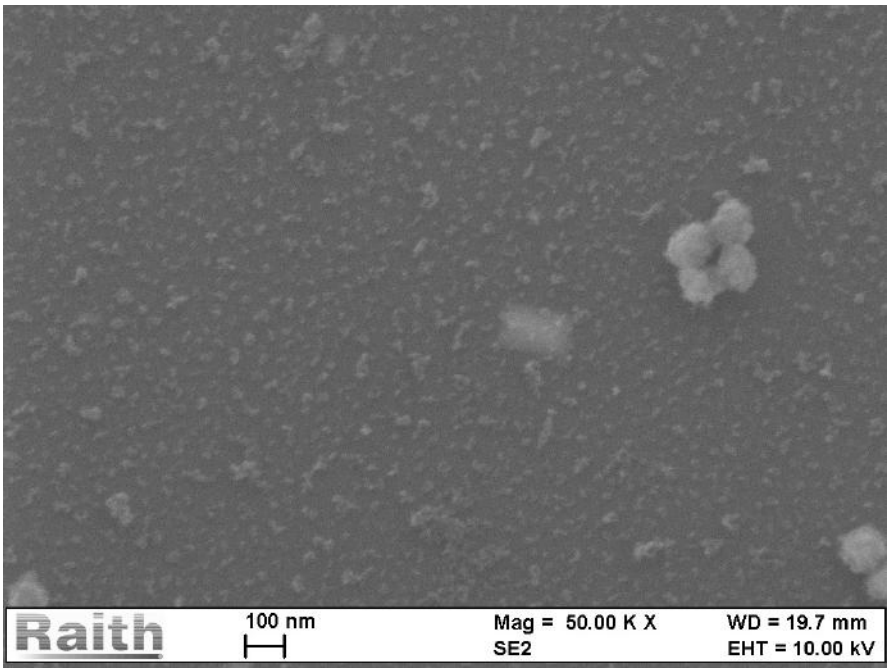

(a)

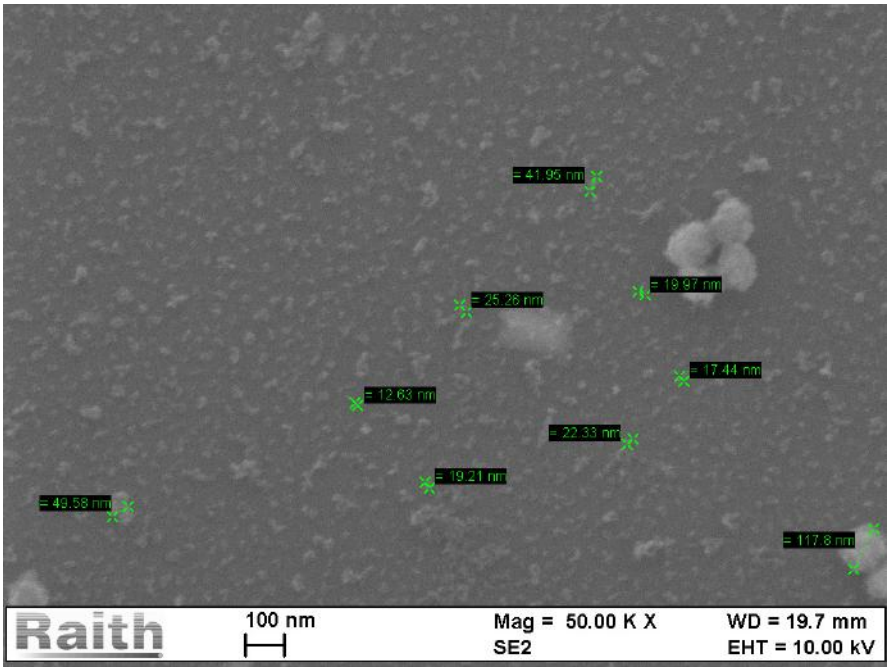

(b)

Figure 6.1: The seeded wafer before deposition. (a) Without size measurements of the agglomerates. (b) With the size measurements of the agglomerates.

Table 6.1: The samples synthesised using a conventional parameters: 96% hydrogen (453 sccm), 4% methane (19 sccm), p=100 torr. For sample E1-6, the substrate temperature was too low for the Landmark pyrometer ($T_{sub} < 600\ ^{\circ}C$). For sample E1-7 the Landmark pyrometer was exchanged with the Raytek pyrometer. NM=Not measured. N/A=Not applicable.

Sample	Temperature Thermocouple [°C]	Temperature Substrate [°C] (Raytek)	Temperature Substrate [°C] (Landmark)
E1-1	500 ± 4	NM	738 ± 6
E1-2	450 ± 3	NM	680 ± 5
E1-3	425 ± 3	NM	660 ± 5
E1-4	400 ± 3	NM	640 ± 5
E1-5	375 ± 3	NM	620 ± 5
E1-6	350 ± 3	NM	< 600
E1-7	300 ± 2	520 ± 2	NM

for the substrate temperatures (using the Landmark pyrometer) were determined to be equal to: $(550 \pm 20)^{\circ}C$ at $T_{Thermocouple} = 300^{\circ}C$ (i.e. sample E1-7), and $(590 \pm 10)^{\circ}C$ at $T_{Thermocouple} = 350^{\circ}C$ (i.e. sample E1-6). By comparing the extrapolated value for E1-7 (Landmark pyrometer) to the measured value of E1-7 (Raytek pyrometer), the systematic error is found to be the same order of magnitude and direction compared to the previous experiment by Justas Zalieckas shown in Table 3.2.

There are three main trends that can be observed from the SEM images. First, the grain size decrease with decreasing temperatures, and is observed for all samples. Second, the amount of crystal twinning increase with decreasing temperatures. The effect of twinning is evident in sample E1-1 and sample E1-2. As the temperature becomes lower, the amount of twinning becomes large enough to form spherical-looking particles, shown in sample E1-6 and E1-7. Third, the morphological transition from intergrown crystals to loosely stacked crystals occur when the temperature was decreased (when comparing sample E1-5 to E1-6). These trends are driven by an increase in the renucleation rate relative to the growth rate. The renucleation rate is still low, since clear facets were formed, similar to the example shown in Figure 3.3a.

The Raman spectra shows the following reoccuring peaks: transpolyacetylene (TPA), two unknown bands at approximately 1080 cm^{-1} and 1230 cm^{-1} with a full width at half maximum (FWHM) equal to 40 cm^{-1} and 80 cm^{-1} respectively, diamond, the G peak, and an peak at around 1720 cm^{-1} from C=O bonds. Additional unknown peaks observed in Figure 6.2b, 6.2d, and 6.2g are also marked in

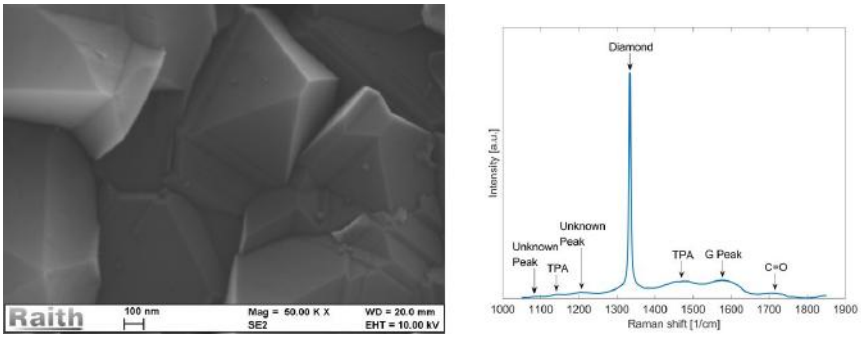

(a) Sample E1-1, $T_{Substrate} = 738°C$

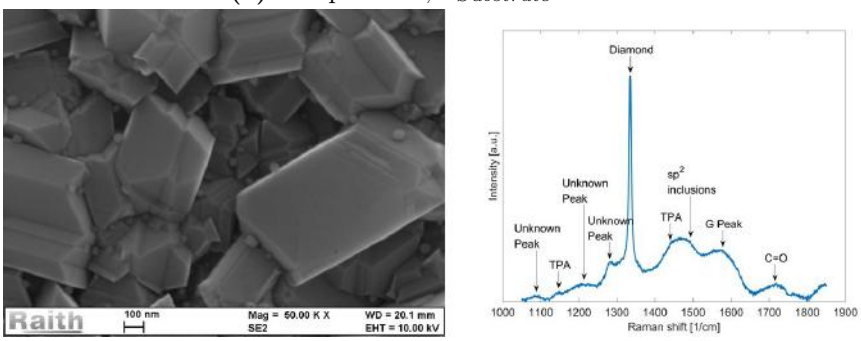

(b) Sample E1-2, $T_{Substrate} = 680°C$

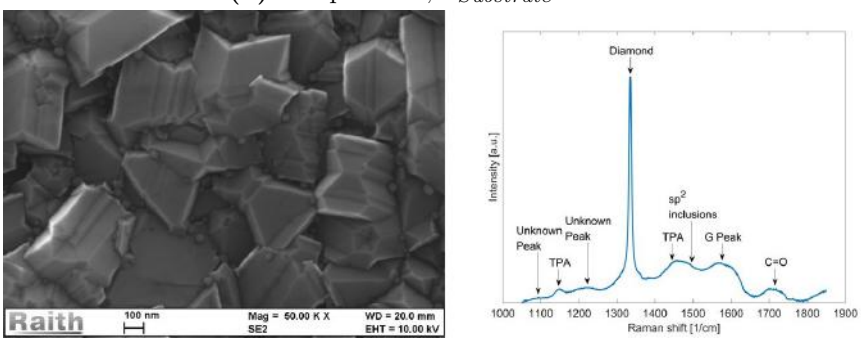

(c) Sample E1-3, $T_{Substrate} = 660°C$

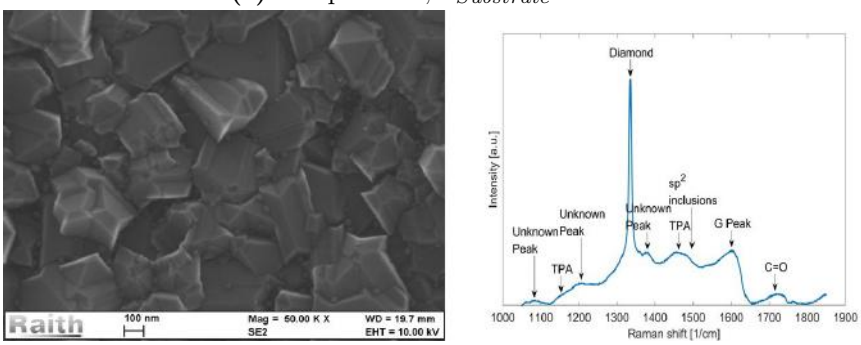

(d) Sample E1-4, $T_{Substrate} = 640°C$

the spectra. None of these unknown peaks fit the references discussed in section 3.2. The peak at 1720 cm^{-1} comes from C=O bonds. Although no oxygen is present in the deposition, C=O bonds may still form after the deposition, as oxygen in the atmosphere can reacts with the sample to form carbonyl groups [71]. The narrow FWHM shows that there is a low amount of disorder in the diamond bonded carbon and that the diamond domains are rather large. It is still obvious that the quality of the film degrades due to the increasing presence of sp^2 bonded carbon associated with the G peak.

6.2 Experiment 2: Typical Deposition Parameters With Protective Lid

This experiment investigates if adding a protective lid as shown in Figure **??**, will allow deposition of diamond at lower substrate temperatures. It uses the same parameters as the last experiment, and only exchanges the lid. The deposition parameters were: 96% hydrogen (453 sccm), 4% methane (19 sccm), p=100 torr. Four different samples were grown at thermocouple temperatures matching experiment 1. The samples are listed in Table 6.2 along with the temperature they were grown at, and the SEM results and Raman spectra is shown in Figure 6.4.

Table 6.2: The samples synthesised using a conventional parameters (with a protective lid): 96% hydrogen (453 sccm), 4% methane (19 sccm), p=100 torr. Unknown means that the temperature cannot be measured directly.

Sample	Temperature Thermocouple [°C]	Temperature Substrate [°C]	Temperature Protective Lid [°C] (Landmark)
E2-1	500 ± 4	Unknown	730 ± 3
E2-2	450 ± 3	Unknown	690 ± 3
E2-3	425 ± 3	Unknown	652 ± 3
E2-4	400 ± 3	Unknown	645 ± 3

The pyrometer will only be able to measure the temperature of the lid since the substrate is covered by it. This means that the substrate temperature is unknown. The substrate temperature will be estimated in section 7.2.2 using the measured temperature of the lid. As mentioned in section 4.2, the measured temperature of the lid is an underestimation since the pyrometer is not aimed at the center.

The results from the SEM indicate larger renucleation rates relative to the growth rates due to the presence of ballas morphology compared to faceted mor-

phology. Ballas morphology is formed in environments with higher renucleation rates. Similar to experiment 1, reducing the temperature cause a shift in morphology from intergrown crystals to loosely stacked crystals, as well as a decrease in grain size.

The Raman spectra shows the same reoccuring peaks as the Raman spectra of experiment 1: two unknown bands at approximately 1080 cm^{-1} and 1230 cm^{-1} with a full width at half maximum (FWHM) equal to 40 cm^{-1} and 80 cm^{-1} respectively, diamond, the G peak, and an peak at around 1720 cm^{-1} from C=O bonds. From the Raman spectra it is evident that the diamond is present in atleast sample E2-1. For sample E2-2 the diamond peak becomes wider due to disorder in the diamond grains or by smaller grain size (phonon confinement). The buldge towards higher Raman shifts also indicate that the intensity of the D peak is becomming noticable. The strength of the D peak is furthermore increased for sample E2-3, with only a small contribution from diamond evident during the fitting. Lastly, in sample E2-4, the Lorenzian shape of the diamond peak is completely gone and replaced with a Gaussian shaped band located at 1350 cm^{-1}. By comparing the spectra of E2-4 with the reference spectra in Figure 3.2, shows most familiarity to diamond like carbon (DLC). DLC is a mixture of sp^1, sp^2, and sp^3 bonded carbon. The major difference between E2-4 and the reference is the significantly narrower D band in the case of E2-4. The two unknown peaks at 1080 cm^{-1} and 1230 cm^{-1} repeats themselves in this experiment, as well as an additional peak at 1470-1500 cm^{-1}. Diamond is clearly not present in sample E2-4. The effectiveness of the lid on decreasing the substrate temperature while keeping diamond growth is discussed in section 7.2.2.

6.3 Experiment 3: Optimizing the Gas Composition

This experiment investigates how much the temperature can be reduced by adding oxygen to the gas mixture. The experiment does not use the protective lid. The lid is not used as it is shown in section 7.2.2 that the substrate temperature is not significantly influenced by the lid and the film quality deteriorates significantly while using the lid. The deposition parameters were: 94% hydrogen (235 sccm), 4% methane (10 sccm), 2% carbon dioxygen (5 sccm), p=50 torr. Due to time constrains only one set of parameters were possible to test.

Five samples were grown at temperatures listed in Table 6.3. At low temper-

Table 6.3: The samples synthesised using the parameters (without a protective lid): 94% hydrogen (235 sccm), 4% methane (10 sccm), 2% carbon dioxide (5 sccm), p=50 torr. N/A=Not applicable. LS=Too low signal.

Sample	Temperature Thermocouple [°C]	Temperature Substrate [°C] (Raytek)
E3-1	350 ± 4	450 ± 4
E3-2	300 ± 4	417 ± 4
E3-3	250 ± 2	LS
E3-4	200 ± 2	LS
E3-5	150 ± 2	LS

atures (i.e. for sample E3-3, E3-4, E3-5), insufficient signal was registered by the pyrometer, leaving the substrate temperature of these three samples unknown. These values will be estimated in section 7.2.1. By only considering sample E3-1 and sample E3-2, the ratio between the substrate temperature and the thermocouple temperature changed significantly compared to what was measured in experiment 1. Doing extrapolation for sample E3-3, E3-4, and E3-5, gives the rough estimates of: $384°C$, $351°C$, $318°C$ respectively. The uncertainty on these values can be very large due to them being formed from a sample of 2, but it serves as a very rough approximation of the substrate temperatures.

The SEM results show diamond growth for all samples except sample E3-5. No growth is observed on sample E3-5 when comparing it to the wafer before deposition, see Figure 6.1. High quality diamond facets are observed in sample E3-1, even at the low substrate temperature of $T_{Substrate} = 450°C$. This shows clearly the effect of oxygen and low pressures.

The Raman spectra shows the same reoccuring peaks as the Raman spectra of experiment 1 and experiment 2: two unknown bands at approximately 1080 cm^{-1} and 1230 cm^{-1} with a full width at half maximum (FWHM) equal to 40 cm^{-1} and 80 cm^{-1} respectively, diamond, the G peak, and an peak at around 1720 cm^{-1} from C=O bonds. An additional unknown peak is located at 1400 cm^{-1} in the spectrum for sample E3-1. The Raman spectra show a narrow FWHM for diamond in sample E3-1, E3-2, and E3-3. The signal deteriorate for sample E3-4 and E3-5, indicating that the film thickness is lower, and is supported by the SEM image of sample E3-5.

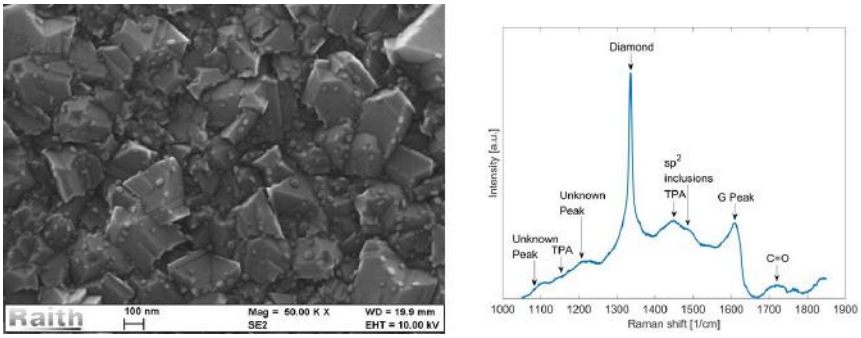

(e) Sample E1-5, $T_{Substrate} = 620°C$

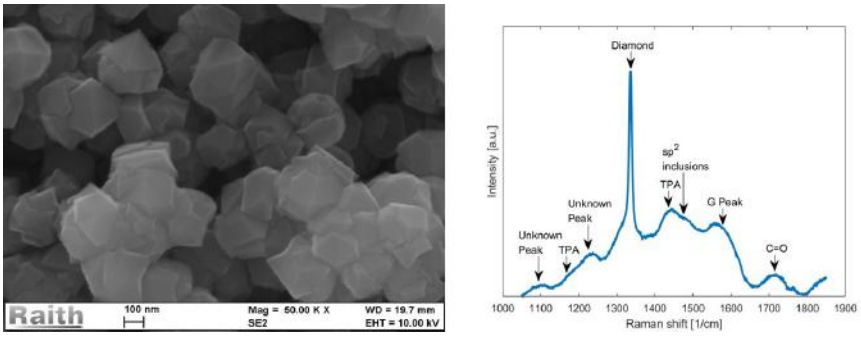

(f) Sample E1-6, $T_{Substrate} < 600°C$

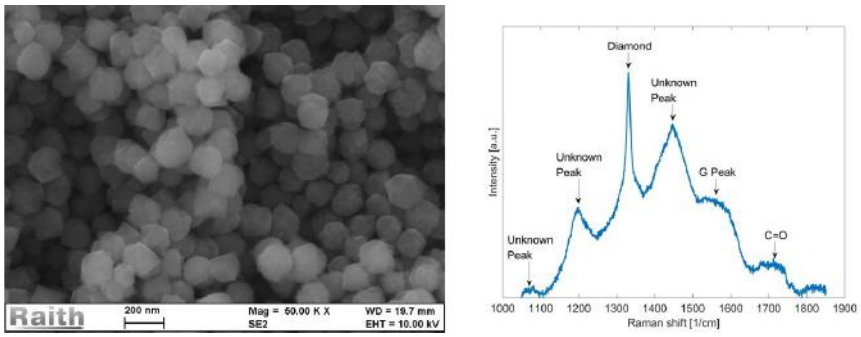

(g) Sample E1-7, $T_{Substrate} = 520°C$

Figure 6.2: The samples synthesised using a conventional parameters: 96% hydrogen (453 sccm), 4% methane (19 sccm), p=100 torr. TPA is the abbreviation for transpolyacetylene .

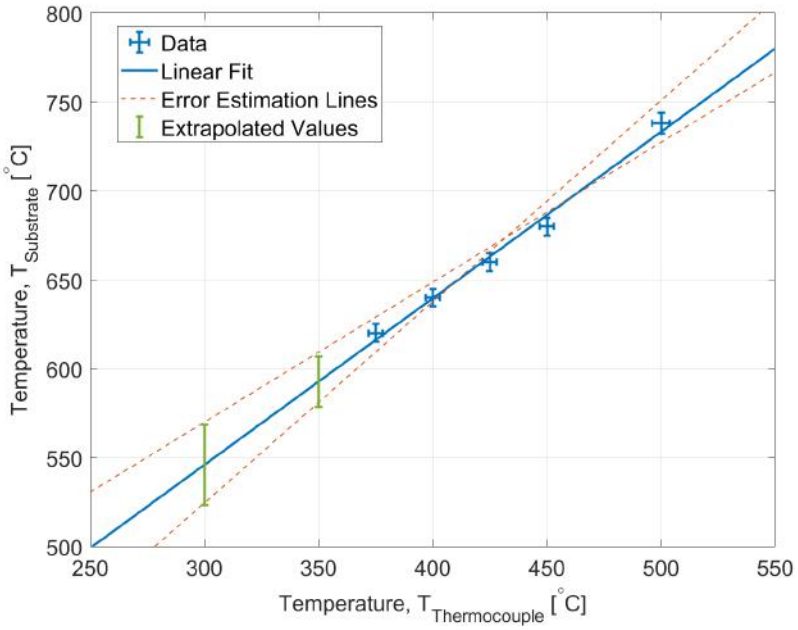

Figure 6.3: Plot of the temperature measured by the thermocouple which is embedded into the sample stage, and the substrate which is located ontop of the sample stage. Fit with a linear function. The data is fitted to a linear curve. The substrate temperature for sample E1-6 and sample E1-7 were estimated by extrapolation. The error of the extrapolated values were estimated by fitting two lines between the left-most and the right most data points.

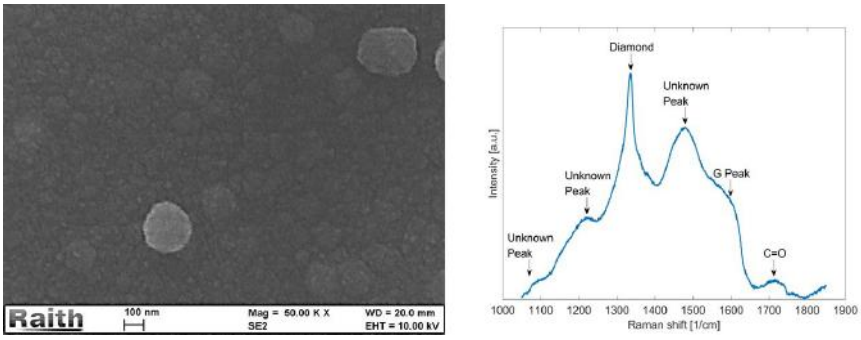

(a) Sample E2-1

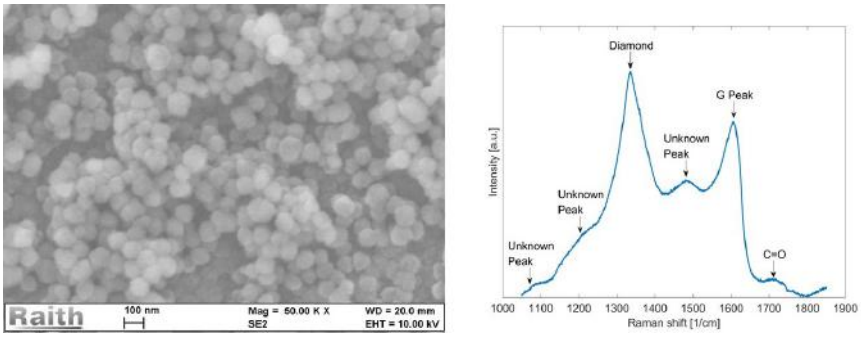

(b) Sample E2-2

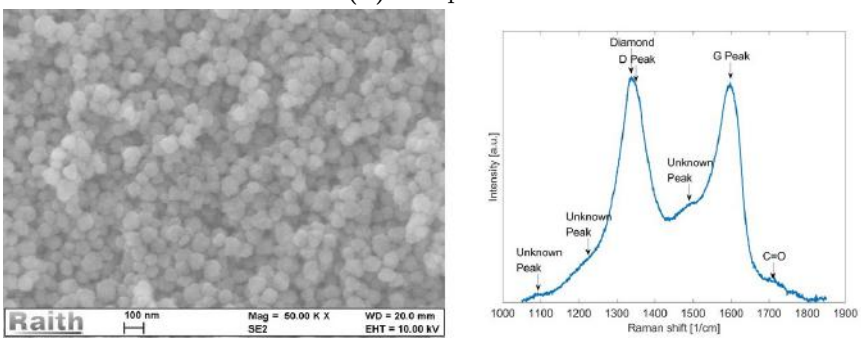

(c) Sample E2-3

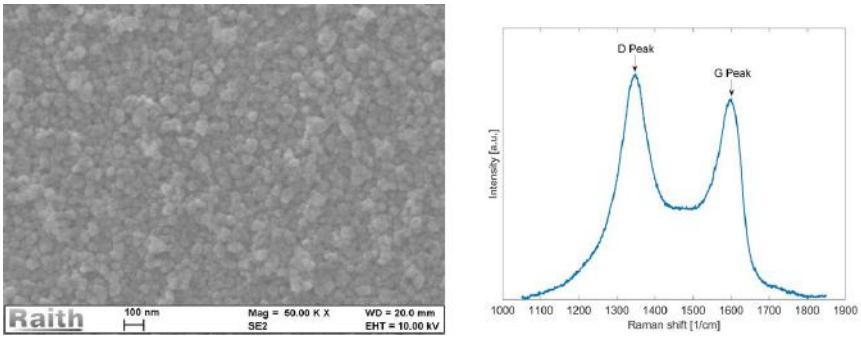

(d) Sample E2-4

Figure 6.4: The samples synthesised using a conventional parameters: 96% hydrogen (453 sccm), 4% methane (19 sccm), p=100 torr. .

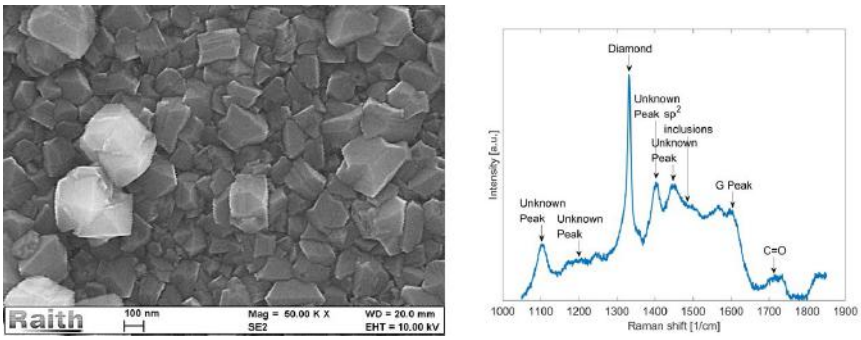

(a) Sample E3-1, $T_{Substrate} = 450°C$

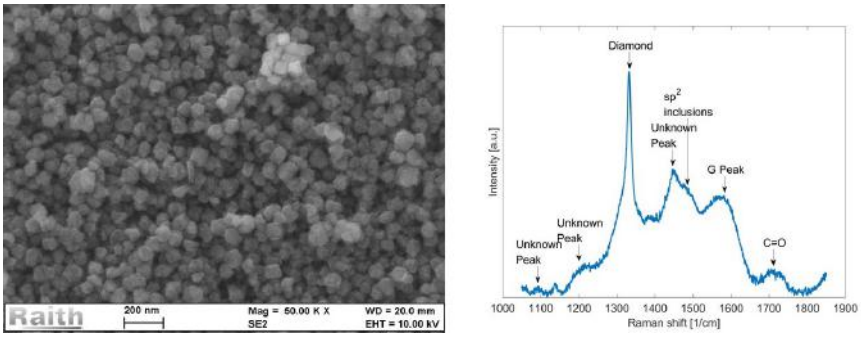

(b) Sample E3-2, $T_{Substrate} = 417°C$

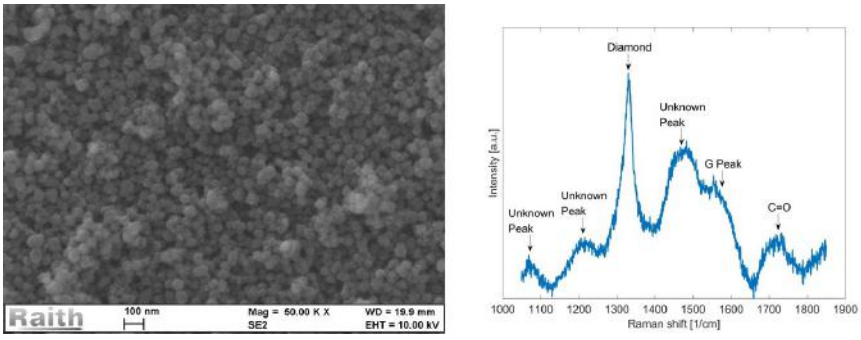

(c) Sample E3-3, $T_{Substrate}$ is unknown.

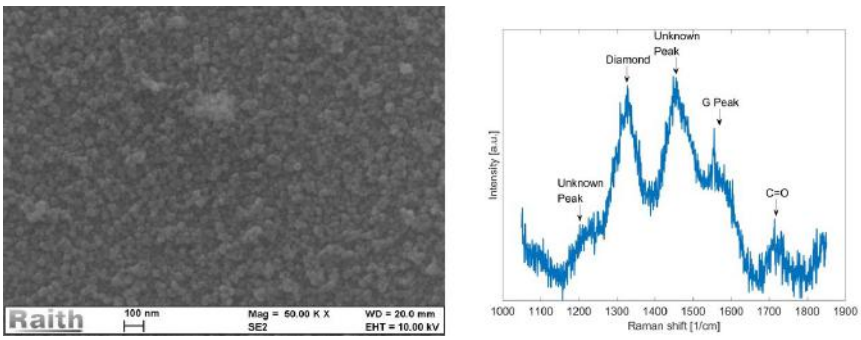

(d) Sample E3-4, $T_{Substrate}$ is unknown.

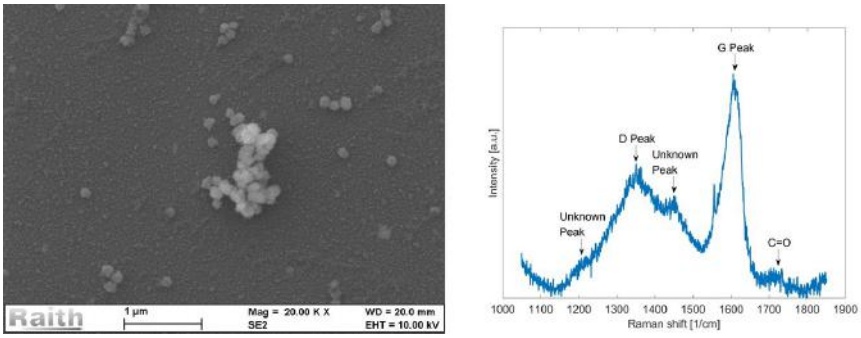

(e) Sample E3-5, $T_{Substrate}$ is unknown.

Figure 6.5: The samples synthesised using the parameters (without a protective lid): 94% hydrogen (235 sccm), 4% methane (10 sccm), 2% carbon dioxide (5 sccm), p=50 torr. .

Chapter 7

Results and Discussion - Simulation

This chapter shows (1) the result from the plasma simulation, and (2) the iterative development of the heat transfer model. The purpose of these simulations is to get an estimate on the substrate temperature whenever no measurements were available. The plasma model and the heat transfer model is in reality coupled. The plasma heats up the sample stage, and the sample stage cools down the plasma. The plasma model and the heat transfer model is divided into two groups to reduce the computation time. The surface of the sample stage is where the two models overlap. And, to decouple the models the interaction zone has to be eliminated. The interaction can be eliminated by using the measured temperature values for the surface of the sample stage from chapter 6.

7.1 Plasma Physics in the Reaction Chamber

This section shows the simulation result for the electric field, the electron density, and the gas temperature. The two stage setups are shown in Figure 4.2 and Figure **??**, and the 3D model of the two stage setups are shown in Figure 5.1a, and Figure 5.1b. The simulation solve for equation 2.1, equation 2.2, and equation 2.3.

7.1.1 Stage: Without Protective Lid

Simulations for the stage without the protective lid were completed using the 3D model from Figure 5.1a. The results for the electric field, electron density and gas temperature are shown in Figure 7.1. The gas temperature plot match well with the general shape of the plasma ball observed through the reactor window. Additionally, electric field enhancements are also visible at the position of the microwave coupler. The enhanced electric field may lead to the generation of secondary plasma which also is an observable effect in some MWP-CVD reactors. This secondary plasma has been observed in the reactor and is shown in the user

manual found in the appendix of this thesis.

A source of uncertainty is the boundary temperature for the plasma simulation. The boundary temperatures are shown in Figure 5.2b. The temperature are approximate. To evaluate the effect of the boundary temperature on the gas temperature distribution, the gas temperature is measured along the parametric curve shown in Figure 7.2a, and the result is shown in Figure 7.2. Regardless of the constant temperature distribution on the boundary, a clear Gaussian-like temperature distribution is still formed at the substrate. In light of this, the temperature distribution can be approximated by a Gaussian distribution close to the substrate. The result also show how that the temperature at different parts of the stage heavily influences the temperature of the gas, and vice versa.

7.1.2 Stage: With Protective Lid

Due to time constraints, this simulation was not completed.

7.2 Heat Transfer in the Metal Stage

This section shows the results for the temperature distribution for both stage setups, an estimation for the substrate temperature on samples for which it could not be directly measured (sample: E2-1, E2-2, E2-3, E2-4, E3-3, E3-4, E3-5), and the iterative design of the heat transport models. The stage setup with the lid and the stage setup without the lid is considered. The 3D model for the two stage setups are shown in Figure 5.3a, and Figure 5.3b. By using temperature measurements at different locations in the system (pyrometer and reactor wall), and the physics model, the temperature throughout the system can be estimated. Unfortunately, the reactor wall cannot be measured, nor can the sample stage other than the center due to low signal or low temperature.

7.2.1 Stage: Without Protective Lid

This subsection considers the stage without the protective lid. The purpose of these simulations is to estimate the substrate temperature of sample E3-3, E3-4, and E3-5. However the models have to first be tailored to fit existing data. The tailoring of the model is done by comparing the measured thermocouple temperatures to simulated thermocouple temperatures of samples' E1-1, E1-2, E1-3, E1-4, E1-5. The measured thermocouple temperatures are listed in Table

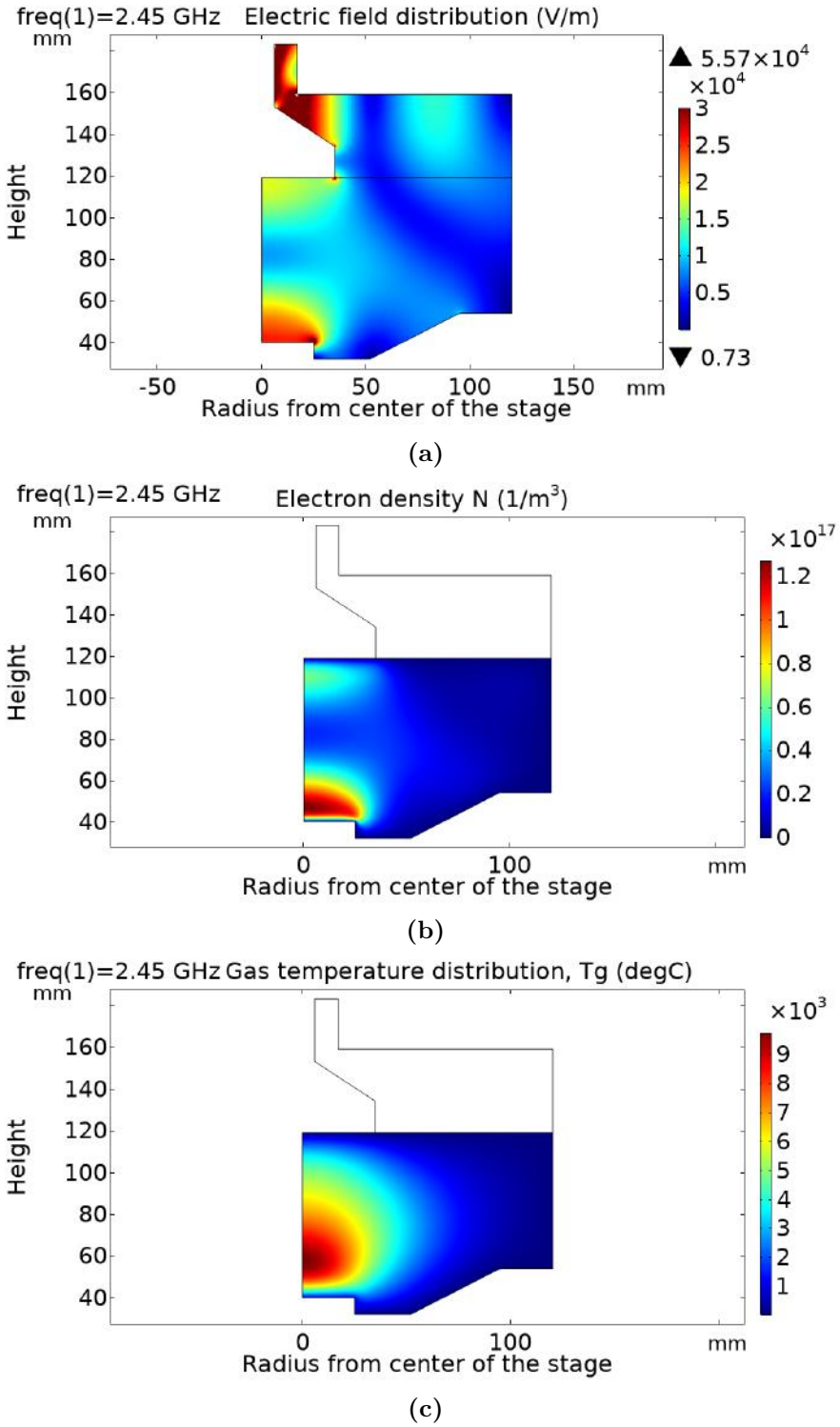

Figure 7.1: Shows the simulation result for: (a) the electric field distribution, (b) the electron density, (c) the gas temperature. The illustration is a 2D slice of the stage being plotted from $r = 0$ and outwards. The full 2D slice can be generated by combining the figure with its mirror image. The frequency of the microwave source was set at 2.45 GHz, and an input power of 3000W.

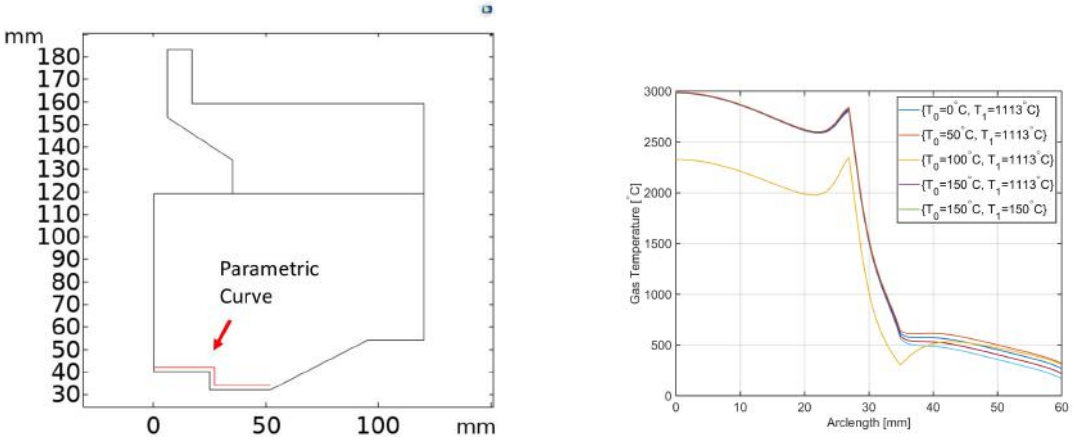

Figure 7.2: Shows the temperature distribution of the gas along the sample stage (2 mm from the stage).

6.1. The only heat transfer mechanism considered is conduction. The reason for this is that the alternative mechanisms, being convection and radiation are insignificant. Convection only whenever material flow is possible, which is not possible in solids. Radiative heat transfer occur in cavities, and is only significant in regions where there is a large temperature difference between the surfaces. This stage configuration has no cavities near the regions of high thermal gradients. The only region with a large thermal gradient is the area close to the substrate, and no cavities can be found near the substrate. The input for the model is the pyrometer values at the substrate shown in Table 6.1, and the temperature of the water cooler has been measured to be approximately $18°C$. The pyrometer value is set at the boundary shown in Figure 5.4a, and the water cooler temperature is set at the boundary shown in Figure 5.5a.

The uncertainty of the simulated temperature is given by,

$$u(T) = \sqrt{\left(\frac{\partial T}{\partial r}u(r)\right)^2 + \left(\frac{\partial T}{\partial z}u(z)\right)^2 + \left(\frac{\partial T}{\partial T_{boundary}}u(T_{boundary})\right)^2} \tag{7.1}$$

where T is the temperature, r is the radial position, z is the depth, and $T_{boundary}$ is the temperature set at the hot boundary (the measured value from the pyrometer). There is also an uncertainty from the water cooler, however this uncertainty is neglected.

For a temperature evaluated at the position of the thermocouple: *u(r)*, and *u(z)* are given in section 3.3.2 equal to: $u(r) = \frac{2}{\sqrt{3}}mm$ and $u(z) = \frac{0.05}{\sqrt{3}}mm$. The division by $\sqrt{3}$ is to convert between the rectangular uncertainty distribution and

a Gaussian uncertainty distributions. The sensitivity of temperature relative to position can be approximated using the definition of the differential operator,

$$\frac{\partial T}{\partial r} \approx \frac{T(r+u(r)) - T(r-u(r))}{2u(r)}, \quad \frac{\partial T}{\partial z} \approx \frac{T(z+u(z)) - T(z-u(z))}{2u(z)}.$$

These temperature values, (i.e. $T(r+u(r))$, $T(r-u(r))$, $T(z+u(z))$, $T(z-u(z))$), cannot be measured and has to be determined from the simulations. The uncertainty in the temperature on the hot boundary $u(T_{boundary})$ comes from the inaccuracy of the pyrometer given in Table 6.1 and using the same table the sensitivity can also be expressed by:

$$\frac{\partial T}{\partial T_{boundary}} = \frac{\partial T_{Thermocouple}}{\partial T_{Pyrometer}} \approx 1.1.$$

Model 1: Flat Temperature Distribution Boundary Condition

The starting point for the model is assuming a temperature distribution on the boundary shown in Figure 5.4a. A constant temperature distribution across the boundary is assumed. The temperature at this boundary is set to be equal to the pyrometer values of Table 6.1. The results from the simulations are shown in Table 7.1 in terms of thermocouple temperatures. It is clear that there is a large uncertainty in the simulated temperature. However, the simulations and the measured value do overlap for all the values in the data set.

The different contributions of uncertainty are evaluated and compared in Figure 7.3. The figure shows that the uncertainty in radial position of the thermocouple, *u(r)*, is the only significant contribution. The uncertainty in position is a systematic error. To account for systematic error, the position can be optimized to fit perfectly with the data of sample E1-1, giving: $r = 11.168$ mm and $z = 0.153$ mm. Using these parameters, the values for the rest of the samples (E1-2, E1-3, E1-4, and E1-5) can be predicted and are shown in Table 7.2. Since the positions are optimized, there are no uncertainties in r and z. The simulation results using these optimalizations show a trend between samples which do not match the measurements. This result cannot be attributed to randomness due to the low uncertainty, nor systematic error, and is most likely by an inaccurate physical model.

The simulated temperature distribution for sample E1-1 is shown in Figure 7.4a. The general trend of the temperature distribution is shared among the other samples. The temperature distribution can be described as a gradual trans-

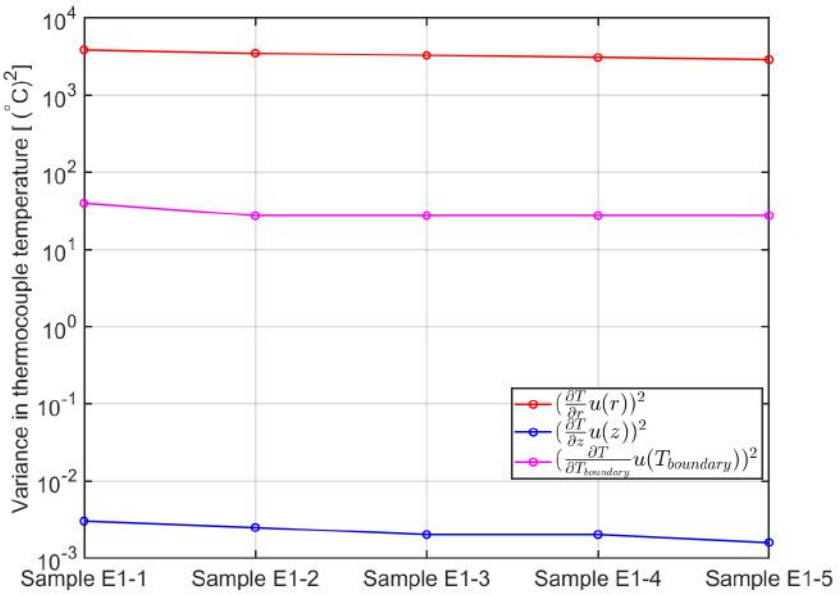

Figure 7.3: Comparison between sources of uncertainty on the temperature at the thermocouple position. The red line represents the radial position uncertainty of the thermocouple. The blue line represents the depth position uncertainty of the thermocouple. The purple line represents the uncertainty in the pyrometer measurements. $r$is radial position of the thermocouple, z is the depth of the thermocouple embedded into the stage, and $u(T_{boundary})$ is the uncertainty of boundary temperature caused by uncertainties in the pyrometer measurement.

formation between two semiellipses of different focal points. One immediately noticeable feature is how rapid the temperature distribution falls off along the radial direction.

Table 7.1: Simulation results comparison the simulated and the measured thermocouple values.

Sample	Measured Temperature Thermocouple [°C]	Simulated Temperature Thermocouple [°C]
E1-1	500 ± 4	450 ± 60
E1-2	450 ± 3	410 ± 60
E1-3	425 ± 3	400 ± 60
E1-4	400 ± 3	390 ± 60
E1-5	375 ± 2	380 ± 50

Table 7.2: Simulation results when the thermocouple position is optimized to match with sample E1-1.

Sample	With Optimal Position [°C]
E1-1	500 ± 7
E1-2	461 ± 6
E1-3	447 ± 6
E1-4	434 ± 6
E1-5	421 ± 6

Model 2: Gaussian Temperature Distribution Boundary Condition

As seen by the results from the plasma simulations (see Figure 7.2), the temperature distribution across the top of the substrate is not flat and can be more accurately modeled by assuming a Gaussian temperature distribution. The Gaussian transitions to a different shape at (at arc lengths: 20 mm - 35mm) due to field enhancements close to the edge, and then falls off somewhat linearly (at arc lengths: 35-60). However these two features of the figure were not accounted for because the temperature values from these two regions was difficult to measure with the pyrometer, due to line of sight or low signal/low temperature.

A simple Gaussian temperature distribution was used for the boundary condition. The requirements of the Gaussian distribution is the following: (1) easy to parametrize, (2) the temperature goes to the cooler temperature at distances infinitely far away, (3) distribution has a smooth shape with one central peak where the temperature is at the maximum. Assumption (2) is not entirely correct as illustrated by Figure 7.2, there seems to be an offset. The Gaussian temperature distribution can be written mathematically by,

$$T_{boundary}(x, y) = (T_s - T_c)e^{-(\frac{x^2+y^2}{2\sigma^2})} + T_c$$

assuming that the origin of the coordinate system is centered in the middle of the substrate. The standard deviation σ is calculated empirically from measuring the temperature distribution using a pyrometer at different positions on the substrate. The temperature at the center of the substrate was measured to be 755 $^{\circ}C$ and the edge of the substrate was measured to be 632 $^{\circ}C$. The distance from the center was: $r = (14 \pm 3)mm$ (given with a rectangular uncertainty distribution). Resulting in a standard deviation: $\sigma = (23 \pm 5)mm$. The simulated temperature distribution for sample E1-1 is then shown in Figure 7.4b. This gives a predicted temperature at the thermocouple of $T_{Thermocouple} = (482 \pm 65)^{\circ}C$. This is incorrect when compared to the real measured thermocouple value of of the thermocouple, which is equal to $T_{Thermocouple} = (500 \pm 4)^{\circ}C$. The Gaussian temperature distribution should address the correct values for the substrate, but not for any other parts of the system.

Further improvements can be done by adding a temperature distribution across the entire surface of the stage which is in contact with the plasma. This means that not only the blue substrate is heated, but also the rest of the stage in Figure 5.5a. The temperature distribution should then be shaped similarly to Figure 7.4b, where an Gaussian-like distribution is added close to the center, and a

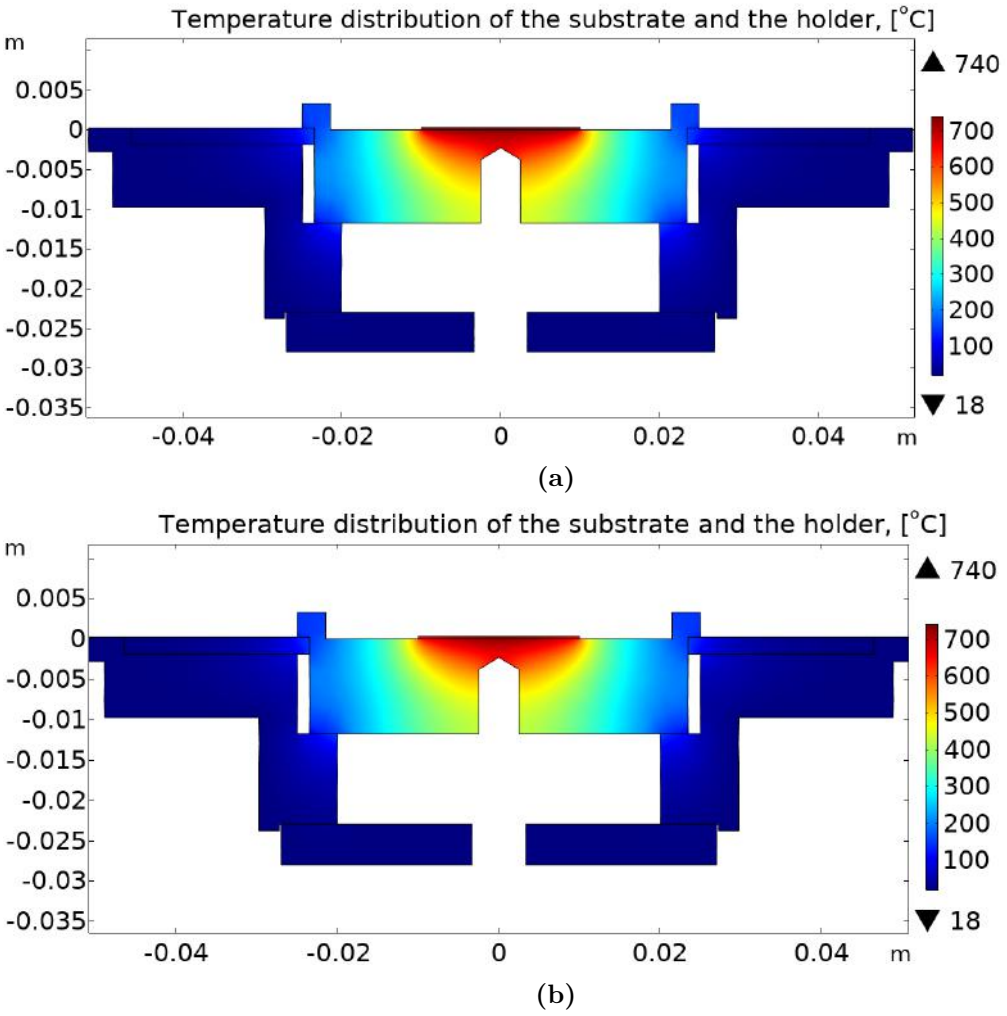

Figure 7.4: (a) The temperature distribution when assuming a flat temperature distribution as the boundary condition. (b) The temperature distribution when assuming a Gaussian temperature distribution as the boundary condition.

linear-like distribution further away from the stage. An alternative approach is by combining the plasma model and the heat transfer model into one model. Some minor improvements to the heat model can also be done by adding thermal contact between separate physical domains, such as the boundary between the substrate and the stage, and between different stage components.

Substrate temperature of samples: E3-3, E3-4, E3-5

Model 1 is used to predict the substrate temperature of samples E3-3, E3-4, and E3-5. The reason model 1 is chosen is because it is more consistent with the temperature measurements. In this case, the thermocouple temperature is used to predict the substrate temperature. This means that the uncertainty equation

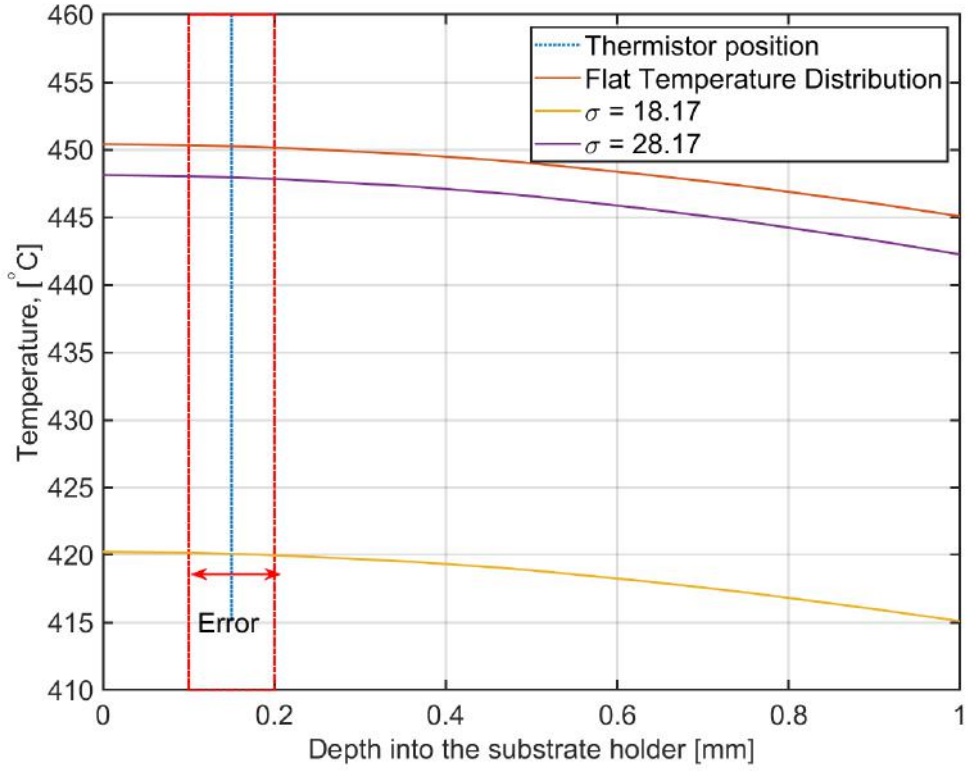

Figure 7.5: Temperature at the position of the thermocouple from heat transfer simulations. The measured temperature value by the thermocouple was $500°C$ (sample E1-1). The two red parallel lines showcase the uncertainty in the thermocouple depth. Similarily, the purple line and the yellow line also signify uncertainty. The yellow line denotes the value σ shifted one standard deviation down, and the purple line denotes the value of σ shifted one standard deviation up.

becomes approximately,

$$u(T) = \sqrt{\left(\frac{\partial T}{\partial r}u(r)\right)^2 + \left(\frac{\partial T}{\partial T_{Thermocouple}}u(T_{Thermocouple})\right)^2} = \frac{1}{1.1}u(T_{Thermocouple})$$

where T is evaluated at the substrate. The uncertainty in radial position is independent in model 1, since the temperature distribution is constant across the substrate. The predicted substrate temperatures are shown in Table 7.3. The results show values which are roughly expected when compared with the trend and values observed in Table 6.3. Although the model is clearly false, the two components which are untrue counteract eachother. The flat distribution give larger substrate temperatures values compared to what is measured and simulated in Figure 7.2. However, this is counteracted by the small area the flat temperature distribution is applied to (see Figure 5.4a).

Table 7.3: Simulated substrate temperature for sample E3-3, sample E3-4, and sample E3-5. The uncertainty holds if the temperature distribution is flat, and only the area shown in Figure 5.4a is exposed to this temperature. The rest of stage is assumed to be heated only by conduction within in the stage.

Sample	Substrate Temperature
E3-3	406 ± 3
E3-4	322 ± 3
E3-5	238 ± 3

7.2.2 Stage: With Protective Lid

For the stage setup with the lid, radiative heating adds as a relevant heat transfer mechanism. Radiative heating occur between the protective lid and the substrate. The 3D model of the stage setup is shown in Figure 5.3b. The experimentally determined temperature values used for the simulations are given in Table 7.4. This represents the measured values for sample E2-1. The primary test for checking if the model behaves well is if the simulated thermocouple temperature becomes: $T_{sub} = (500 \pm 5)°C$. A Gaussian distribution is used for the lid. The reasoning for this is that the surface of the lid is larger, and might not lead to as much of an underestimation. It is assumed that the Gaussian temperature distribution has the same value for σ, $\sigma = (23 \pm 5)mm$.

Parameter	Temperature $[°C]$
Temperature of the Surface, T_s	730
Temperature of Cold Sink, T_c	18

Table 7.4: Experimental values used as model inputs for the simulations.

Model 1: Only conduction

The simplest model for the heat transport in this system is when only conductivity is considered. In this model, both the conductivity of the solid and the fluid is accounted for. The solid consists of the sample stage, the substrate, and the lid. The fluid occupies the cavity bounded by the sample stage, substrate, and lid. The resulting thermal distribution is shown in Figure 7.6a. It is immediately apparent that the substrate temperature is too low.

Model 2: Conduction and Radiation

The heat transport can be increased by adding the effect of radiative heat transfer between the cavity surfaces. The resulting thermal distribution is shown in Figure 7.6b. Similar to model 1, the temperature is too low at the position of the thermocouple. It is obvious from the result of model 1 and model 2 that solid conduction is dominating, to such an extent that it cannot explain the measured values. The effect of radiation and/or conduction by gas is insignificant in comparison. Although conduction does allow heat to flow from the surface of the lid to the substrate, to primarily causes all the heat to flow out to the heat sink.

A natural extension of the model which could explain this large disparity between the simulation and the result is the effect of thermal contact. The thermal contact will increase the thermocouple temperature and the substrate temperature, since it will partition the temperature distribution into several domains. Domains close to the heat source will have increased temperature, meanwhile the domains close to the heat sink will have decreased temperature. This is caused by the decreased conduction at the boundary regions, effectively function as a dam for the heat flow. The parameters required for modeling the thermal contact is more difficult to acquire due to it being linked to surface roughness, contact pressure, etc. For this reason an alternative approach is recommended.

Model 3: Volumetric averaging of thermal conductivities

An alternative approach to including radiation is to keep the assumption that conductive heating is the primary mechanism, and that the effect of radiative heating is low by comparison, but average out the thermal conductivity of the cavity and the lid. The lid and the cavity will then form a single bulk material. This new bulk material has a thermal conductivity determined by volumetric averaging, i.e. $V_{molybdenum}/(V_{molybdenum} + V_{hydrogen})$, evaluated only for the lid and the cavity. The resulting thermal distribution is shown in Figure 7.6c.

Substrate temperature of samples: E2-1, E2-2, E2-3, E2-3, E2-4

Did not have sufficient time to calculate the substrate temperature for the samples. The effect of the lid cannot be fully determined since the plasma distribution is different when the lid is used, and when the lid is not used. However, the ballas morphology of sample E2-1 indicates lower crystalline quality compared to the clearly faceted crystals of sample E1-1. The primary way of decreasing the substrate temperature successfully is by decreasing the substrate temperature

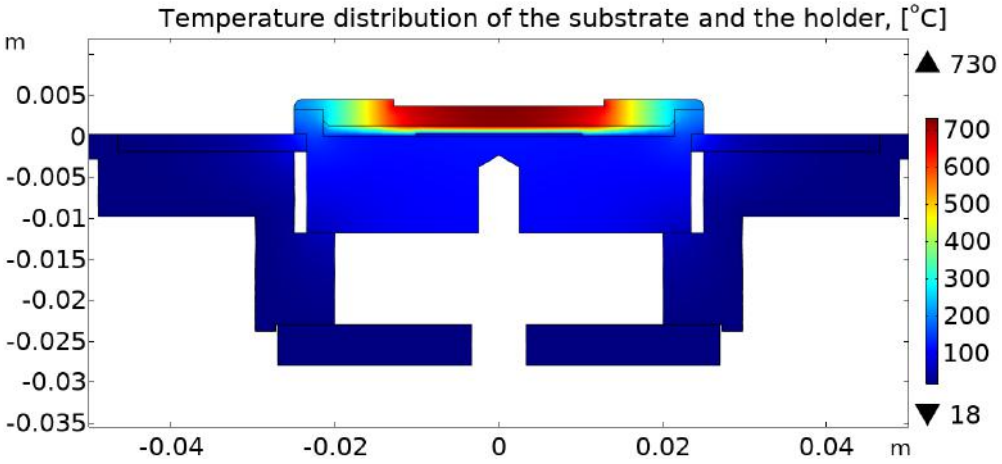

(a)

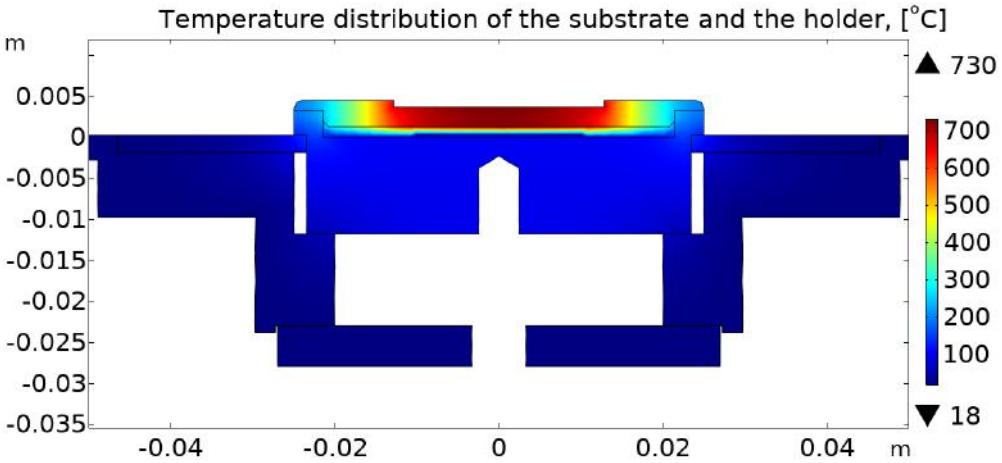

(b)

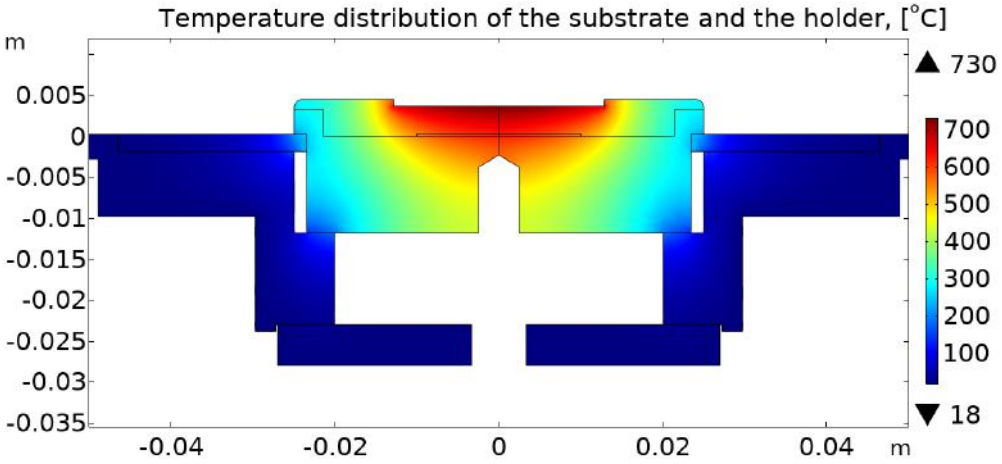

(c)

Figure 7.6: (a) The temperature distribution when assuming only conduction is a significant. (b) The temperature distribution when also accounting for radiative heat transfer. (c) The temperature distribution when the cavity and the cap is replaced with an equivalent thermal conductivity.

without decreasing the crystalline quality substantially. Since E2-1 shows the opposite of the desired effect, experiment 3 was chosen to be completed without a protective lid.

For a more complete investigation of the effect of the protective lid, more simulations have to be done with a combined heat transfer and plasma model. This will relieve some of the restrictive assumptions on the plasma model, and allow a more realistic temperature distribution to be found. This improved model can then be used to evaluate the substrate temperature. Alternatively, the thermocouple can be moved and added directly to the substrate removing the temperature measurement issue.

Chapter 8

Summary

In this thesis, the objective was to (1) perform low temperature microwave plasma chemical vapour deposition (MWP-CVD) of diamond on epoxy coated carbon fiber, (2) write a user manual for the MWP-CVD reactor, and (3) design a new LabVIEW program for the reactor. Simple simulations were also done to estimate the substrate temperature whenever the substrate temperature was impossible to measure.

Low temperature deposition was completed down to substrate temperatures of $450°C$, showing clear crystal facets. Although this is not the lowest deposition temperature in the literature, it is still a low value considering the reasonably high reactor pressure of 50 torr. Different gas compositions and pressures could not be tested due to time restrictions. In a similar vain, different substrates were not investigated due to time restrictions.

Simulations were done to estimate the substrate temperature. The simulations considered both plasma physics in the reaction chamber and heat flow from the reaction chamber into the stage/substrate. The models were shown to be insufficient to accurately estimate the substrate temperature.

A user manual was created by the author of the thesis, and was used for all the depositions. The user manual consists of a brief-chapter regarding key components of a MWP-CVD reactor, a chapter regarding safety, and the deposition procedure.

A new LabVIEW program was designed. The new program added the following new features: (1) being able to run lists of instructions from text files, (2) automatically create a log file with all the commands being sent to the reactor during the reactor run-time, (3) this log file can be inserted back into the instruction reader such that the deposition can be repeated in the future, (4) the state of the reactor (pressure, temperature, etc) is automatically saved in a log file, (5) automatic controls (categorized by emergency controls e.g. overheating, and normal controls e.g. PID controllers), (6) architecture for the automatic controls such that additional controls can easily be added, (7) user output which shows error properties (such as when the error first occurred, when it last occurred, where it occurred, and how many times it occurred), (9) added structures which can do

action based on all errors which are produced, (10) communication between loops in the form of a message handler.

Chapter 9

Future work

For any future work on low temperature deposition it is suggested that (a) the substrate temperature is measured directly with the thermocouple, and (b) more than two gas compositions should be tested. Although it was discussed that the plasma model and the heat transfer model should be combined, it would no longer be necessary if the thermocouple measures the substrate temperature directly.

Appendices

Appendix A

User Manual Microwave Power Chemical Vapour Deposition Reactor

This section of the appendix shows the user manual written by the author. It includes a description of the following: key components of the reactor, safety hazards of the laboratory and the reactor system, the deposition procedure.

User Manual
Microwave Plasma Chemical Vapour Deposition Reactor

by John Benjamin Lothe

May 12, 2021

Contents

1 Introduction

This user manual explains the step by step procedure for running the small microwave plasma chemical vapour deposition (MWPCVD) reactor at the University of Bergen. Chemical vapour deposition (CVD) rely on depositing activated gaseous reactants on a substrate to form a film. In this system, the gas activation is done by microwaves.

2 System overview

The MWPCVD system is shown in Figure 1. The system contains 6 subsystems: the gas supply, the vacuum pump, the microwave system, the deposition chamber, the cooling system, and the control system.

(a) The cabinet storing the hydrogen and methane is found in the left in the image. In the middle, under the window and on the floor is the vacuum pump. The deposition reactor is located in the middle of the scaffolding. And, lastly the microwave generator is found under the metal covers.

(b) The water cooler is located across the room.

Figure 1: MWPCVD system overview (date: 17/08/2020).

2.1 Gas supply

The gases used in the deposition is mostly hydrogen and methane. The hydrogen and methane cylinders are located in the cabinet. The hydrogen cylinder is connected to a manually operated gas central, shown in Figure 2. The operational instructions for the gas central is given at the end of the user manual. In any case, interacting with this part of the system is only necessary when starting the rig and after running it. The flow rate is controlled by the user through a LabVIEW program. The LabVIEW program communicates the desired set value to the mass flow meters stationed at the bottom of the scaffolding, as seen in Figure 3. After the gases pass through the

mass flow meters they join together in one centralized pipe. This pipe leads to the deposition chamber.

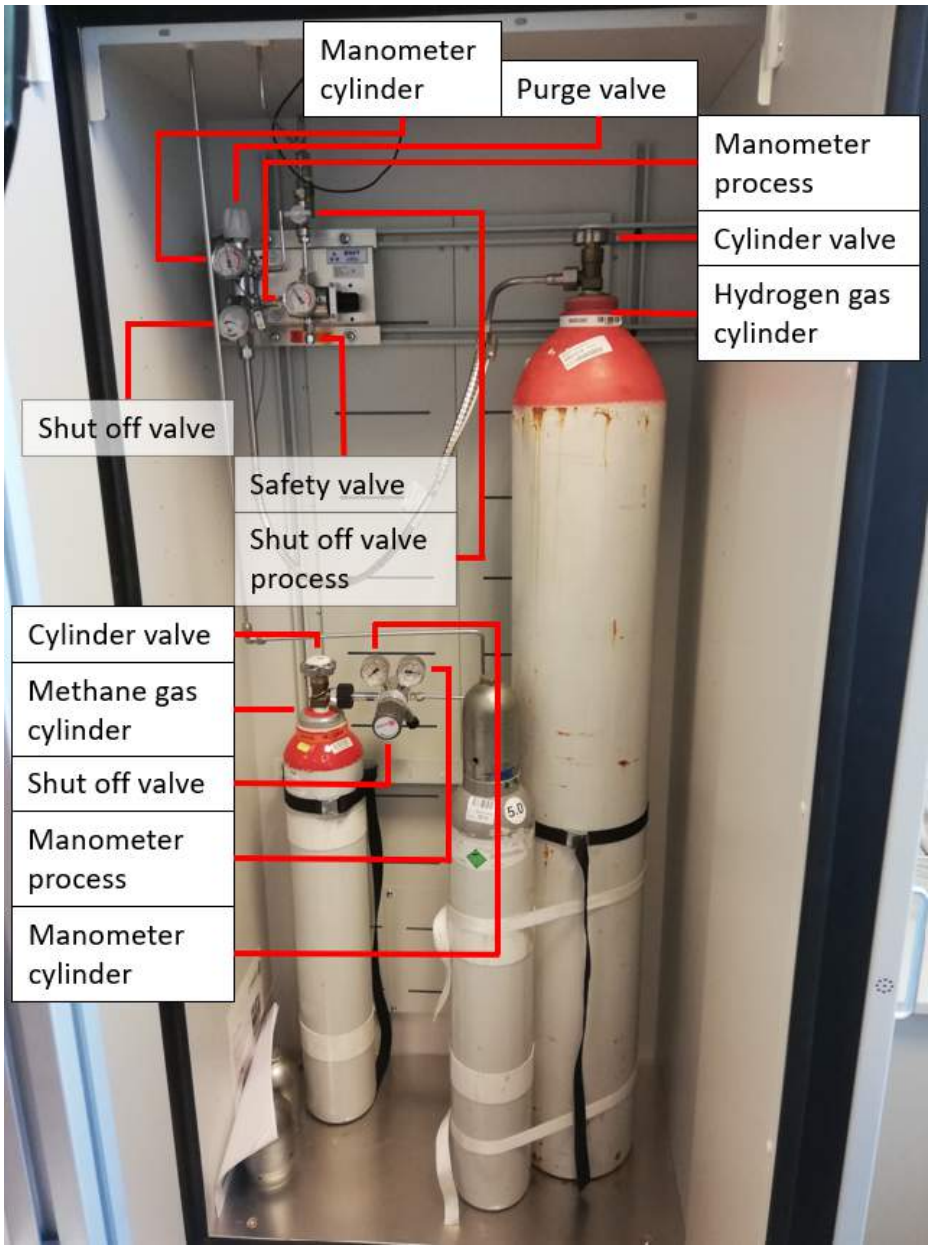

Figure 2: Gas supply located in the cabinet.

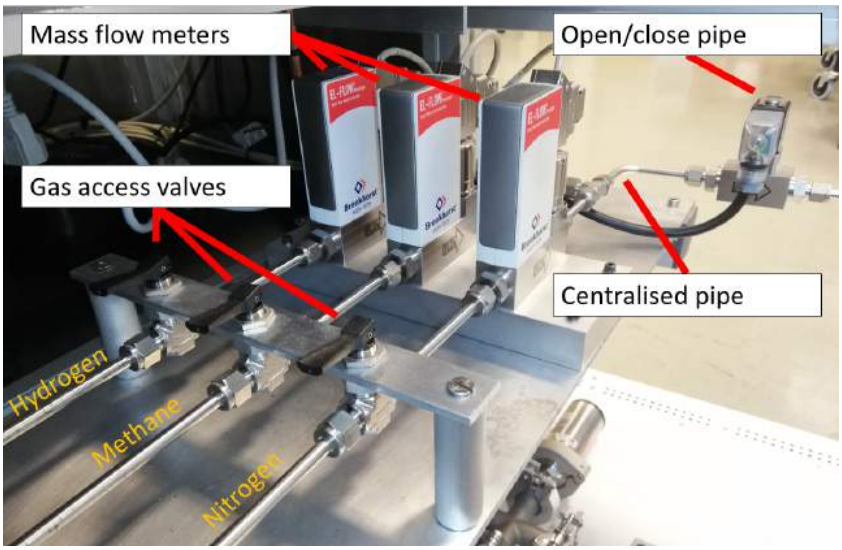

Figure 3: The gas from the cylinders are regulated by a set of mass flow switches. The gases are then mixed together, when they are added to the centralised pipe. The "Open/close valve" button in LabVIEW controls the gas flow in the centralised pipe. However, it can also be controlled by pressing the physical button.

2.2 Vacuum pump

To maintain a specific amount of pressure in the deposition chamber a vacuum pump is used in conjunction with a PID controlled butterfly valve. The set point for the pressure is controlled by the user through the LabVIEW control panel. The vacuum pump and the butterfly valve is shown in Figure 4, along with the direction of the gas flow, and other minor components. The adjustment valve allows the opportunity to pump straight from the upper chamber half, which is useful for decreasing the pressure further.

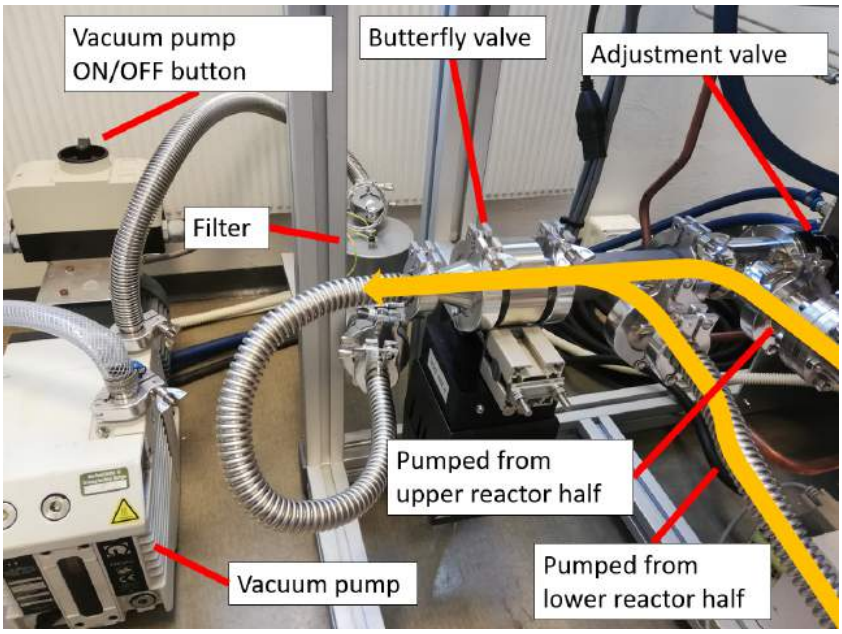

Figure 4: The vacuum pump system.

2.3 Microwave system

The microwave system is responsible for the generation and the transport of microwaves to the deposition chamber. The microwave system consists of the following components: a power supply, a magnetron, a circulator, a dummy load, multiple rectangular waveguides, a three-step tuner, a circular waveguide, and a reflecting wall. The microwaves are generated from the magnetron and travel through the system as shown in Figure 5. The power to run the magnetron is supplied from the power supply shown in Figure 6. Once the microwaves reaches the junction between the rectangular and the circular waveguide, they encounter a reflective object which is obstructing their way. This reflective object has a very specific geometric shape which allows it to transfer the microwaves from the rectangular waveguide to the circular waveguide. To futher increase the power entering the chamber, a reflective wall is included at the end of the path. It is also desired to reduce reflections. Reflections occur in regions where the impedance changes abruptly. To reduce these reflections, the impedance of the components on the left of Figure 5 has to be equal to the the impedance of the components on the right side. This impedance matching is done by a device known as a three-step tuner. The three-step tuner has three modes: (1)

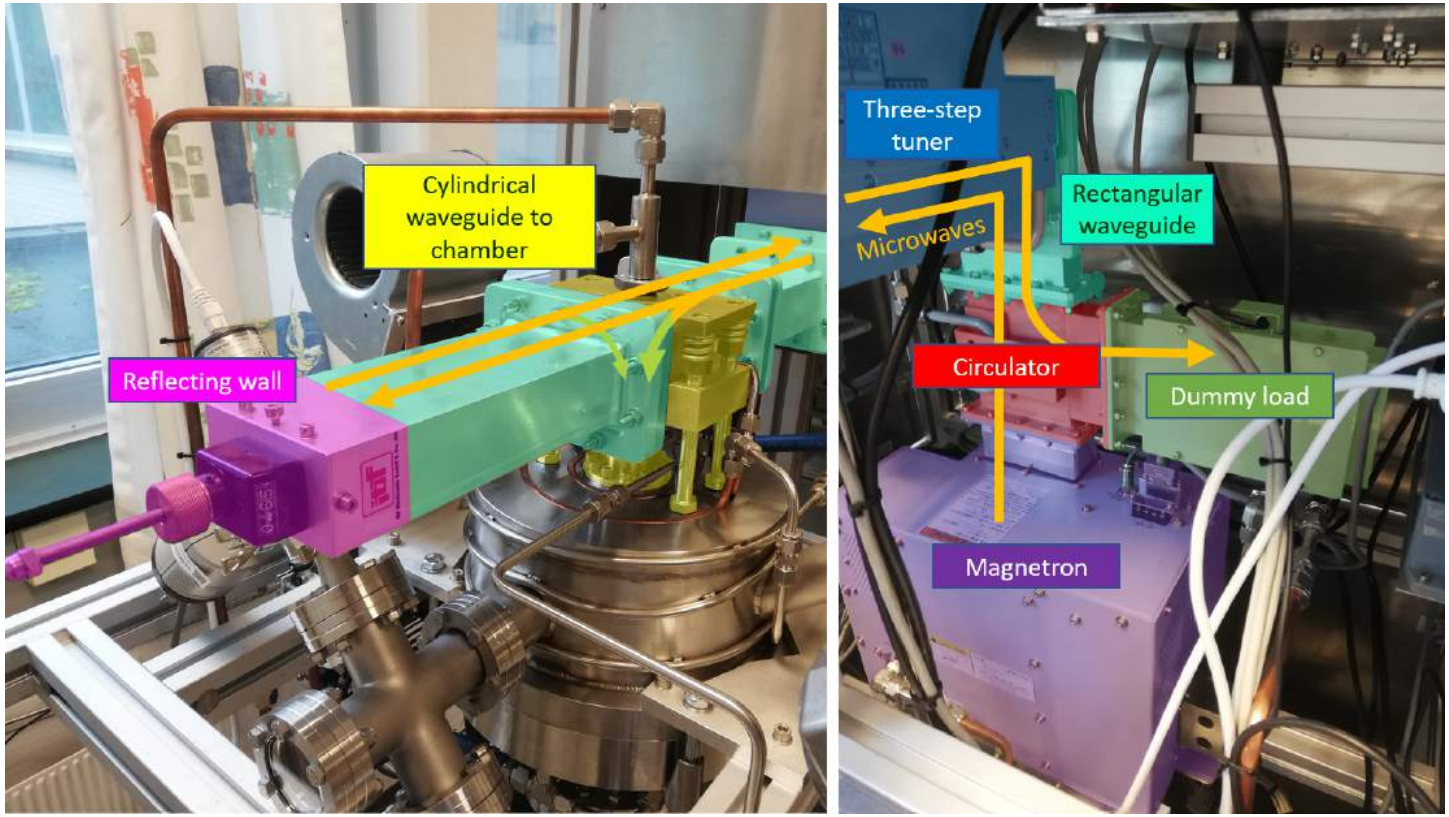

Figure 5: Illustrating conceptually how the microwave system works.

automatic, (2) manual, and (3) preset. During deposition it is required to use both the automatic mode and the manual mode. In addition, the user interface of the tuner also list the following measurements: forward power, reflected power, and the reflection coefficients. The tuning nob is used to navigate between the mode selection and the measurement tabs.

Figure 6: Shows the power supply for the magnetron.

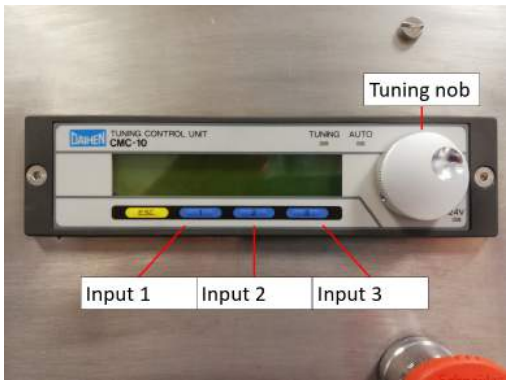

Figure 7: Shows the user interface of the automatic tuner.

2.4 Deposition chamber

The primary function of the deposition chamber is to facilitate an environment suited for diamond growth. This requires the combination of the previously mentioned subsystems. Some other notable features of the deposition chamber is: the substrate holder, the O-ring, the two windows, and the quartz ring. The primary window is used when studying the plasma, but also when measuring the substrate temperature. The secondary window is important for investigating if there is any secondary plasma present. This plasma can damage important components especially if it breaks through the protective quartz ring. The lower half of the deposition chamber is shown in Figure 8, and the upper part of the deposition chamber is shown in Figure 9.

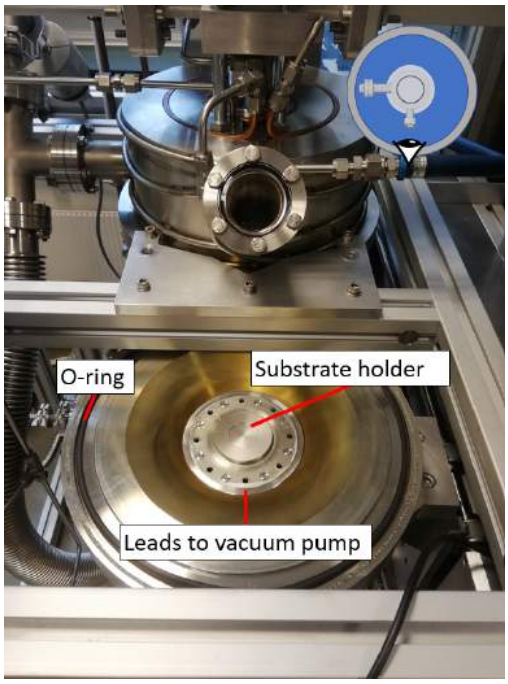

Figure 8: Lower chamber half.

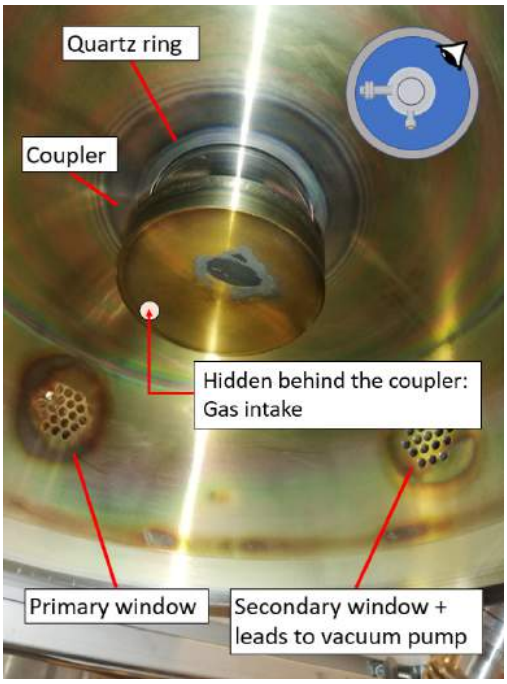

Figure 9: Upper chamber half

2.5 Cooling system

To keep the deposition reactor cool, both water cooling and air cooling is employed. Air cooling is done by a set of fans, one that point at the bottom of the reactor, and one that points at the top of the reactor. The water cooling pump is separated from the MWPCVD reactor, as seen in Figure 10. The water cooler consists of a pump, and a large electric fan that cools the pipe. The water pipe supplies cold water to the water reservoir of the reactor, to the components of the microwave system, and also wraps around the reactor walls for further cooling. The water in the cooler has to be between the minimum and the maximum value during the run. To change the water level, read the instructions located on the the cooler.

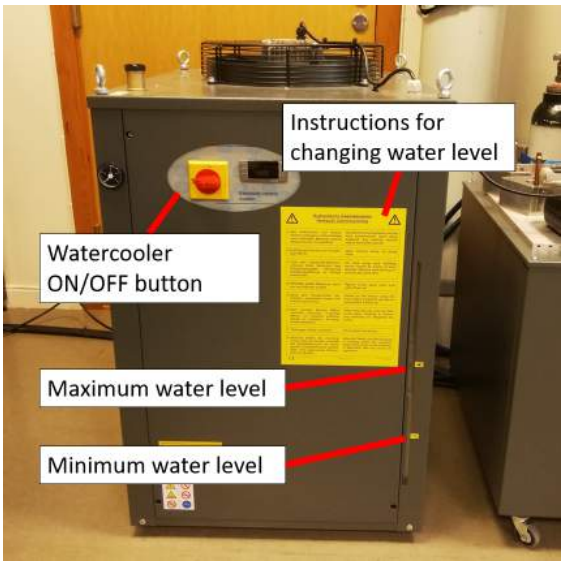

Figure 10: Water cooler

2.6 Control system

There are two components of the control system which the user will interact with: the LabVIEW front panel, and the electrical panel. The LabVIEW front panel sends the desired set points to other controllers like the butterfly valve controller, the mass flow meter controller, and etc. These controllers then adjust the system directly, like opening or closing valves. However, the electrical panel has to be accessed to power all of these devices, including the computer which runs the LabVIEW front panel. This is done by flipping the respective master switches found on the electrical panel, see Figure 11. Most of the master switches are located at the opposite side of the scaffolding, and face the power outlets. However, some of the master switches are located on the devices themselves, for example the master switch for the power supply, as shown in Figure 6. After the computer and the display has been turned on using the master switches, the LabVIEW front panel can be accessed. The directory navigation is shown in Figure 12. During the deposition, the user will control the process purely through the LabVIEW control panel, see Figure 13.

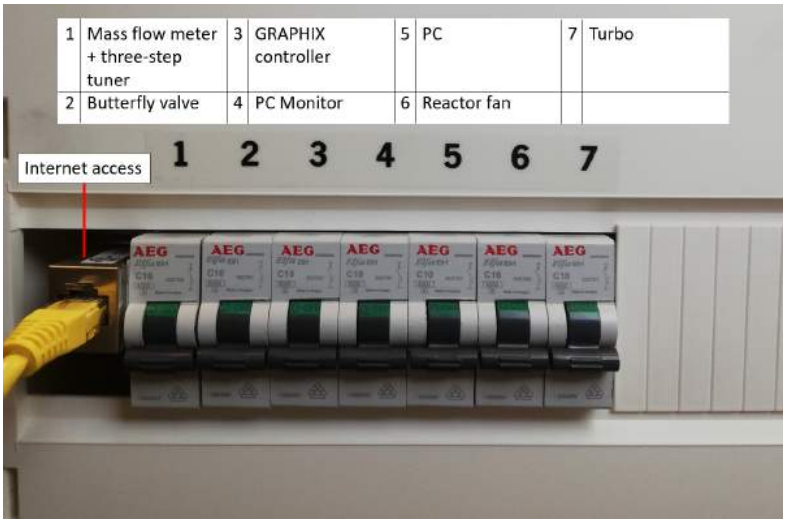

Figure 11: The electrical panel contains the majority of the master switches. Switch down = OFF, switch up = ON.

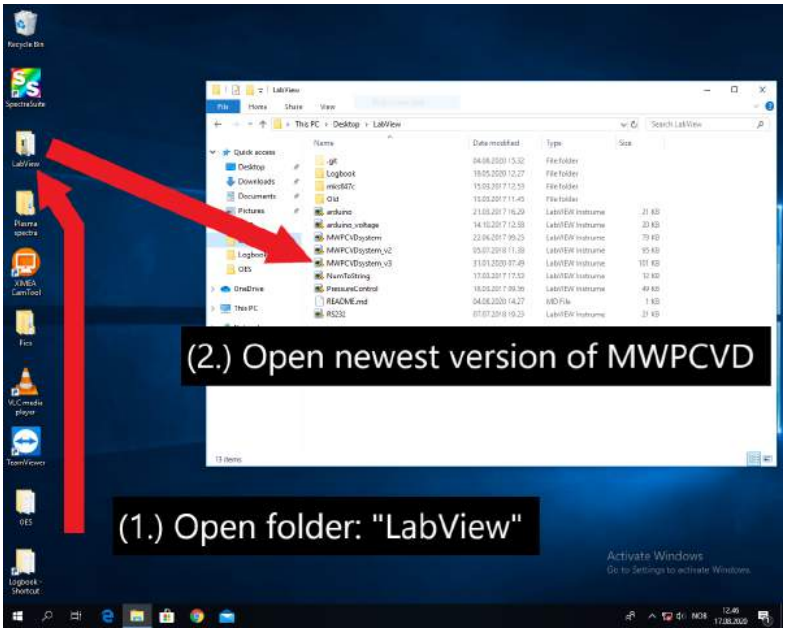

Figure 12: How to start the LabVIEW front panel.

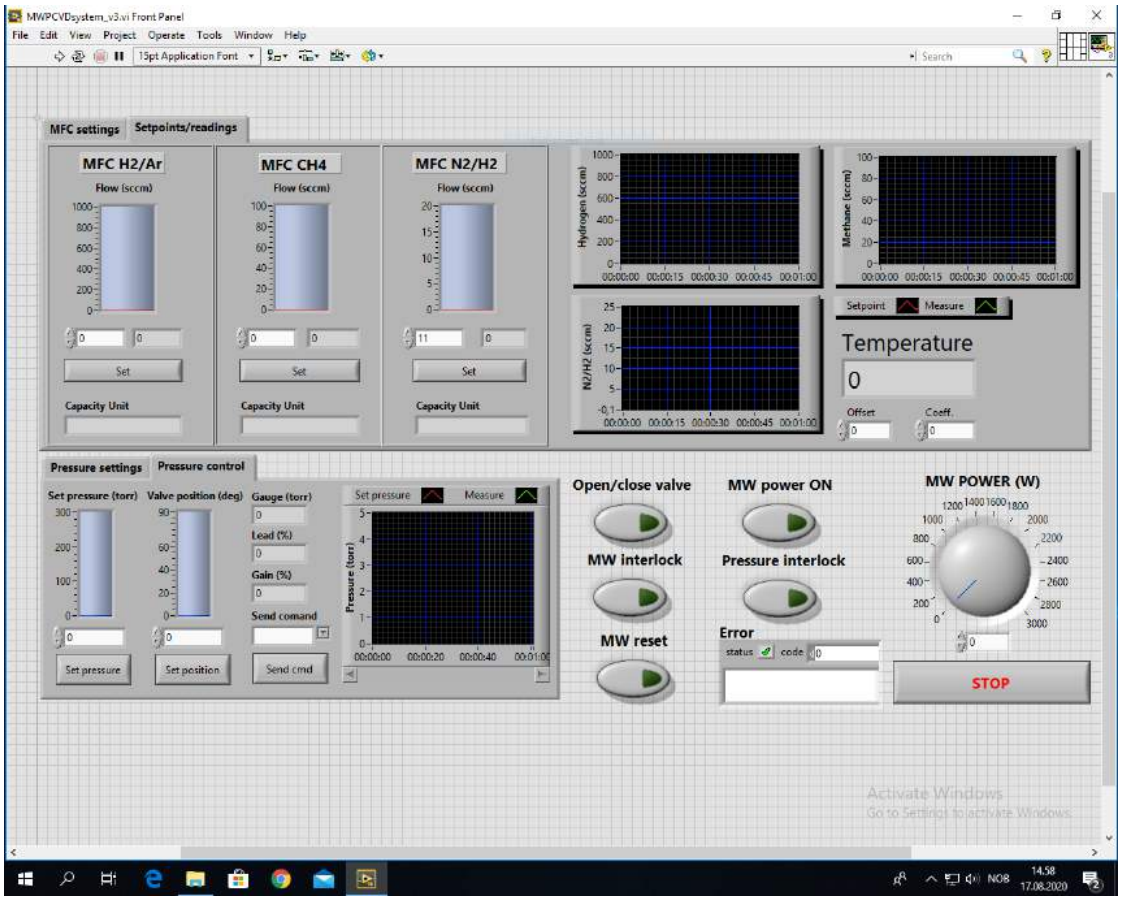

Figure 13: LabVIEW front panel.

3 Safety

3.1 Beeping: Flourine gas leak

If loud beeping is heard in the laboratory, hit the emergency button for the reactor and leave the room immediately! Fluorine gas is leaking from the gas tank. Contact the person listed on the door. The in-field treatment for fluorine gas exposure is given below:

- Eye exposure: Rinse with room temperature water for 15 minutes.
- Skin exposure: Treat as if a thermal burn.
- Inhalation exposure: Move to an environment with fresh air, and administer oxygen if available.
- Further information can be found at: [`https://www.kansashealthsystem.com/-/media/Files/PDF/Poisons/Fluorine.pdf`]

Please note that the in-field treatment should not replaceable treatment provided by medical professionals. The location of the fluoride tank and the fluorine gas detector is shown in Figure 14.

3.2 Microwave leak

While the system is running, the microwaves can leak into the environment. These high intensity microwaves are dangerous as they heavily interfere with electrical systems and can also cause harm to the user. It is thus essential to check for microwave leaks using the microwave leakage detector. **The microwave leakage detector should always be turned on when anyone is inside the room**. Note that the detector automatically turns OFF, so remember to turn it ON again!

3.3 Electric shock

While the system is running, a large amount of electric charge can accumulate on the metallic surface of the microwave system. Do not touch these surfaces while the system is running! The dangerous regions are shown on Figure 15.

3.4 Secondary Plasma

Secondary plasma can be generated from the electric fields at the top of the chamber. This can cause fatal damage to the system if it destroys the protective quartz ring. The presence of secondary plasma can be seen through the secondary window of the chamber. Figure 16 shows the absence of secondary plasma, and Figure 17 shows the presence of secondary plasma.

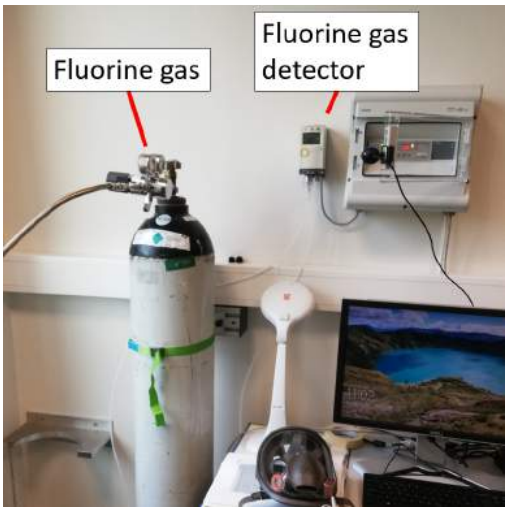

Figure 14: Shows the location of the XeF_2 cylinder, and the fluoride detector beside it. If the alarm goes off, leave the room immediately and call the phone numbers that are listed on the door.

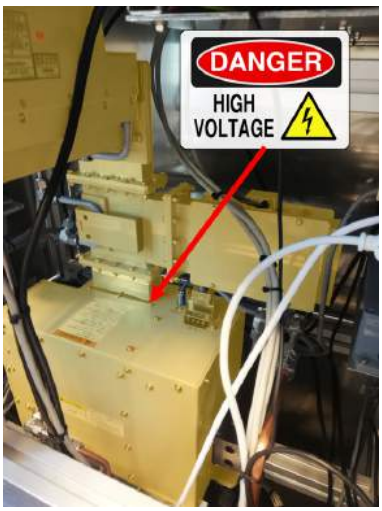

Figure 15: Do not touch the regions shown in yellow, nor any connected metal surfaces that aren't grounded.

Figure 16: Shows the absence of secondary plasma seen through the secondary window of the reactor.

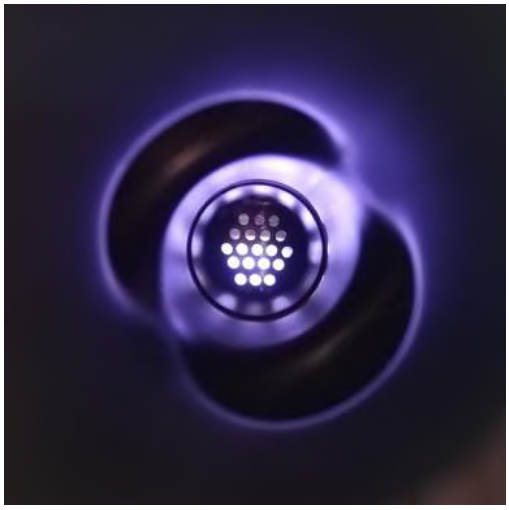

Figure 17: Shows the presence of secondary plasma seen through the secondary window of the reactor.

3.5 Water level for the water cooler

While running the system, the water level of the cooler has to be between the minimum value and the maximum value. The maximum and the minimum value are marked on the water tank, as shown in Figure 10.

3.6 Water leaks

If water is leaking from the cooling system, the system has to be stopped. The water leaks are most commonly found at connection points. The water pipes that should be checked are shown in Figure 18.

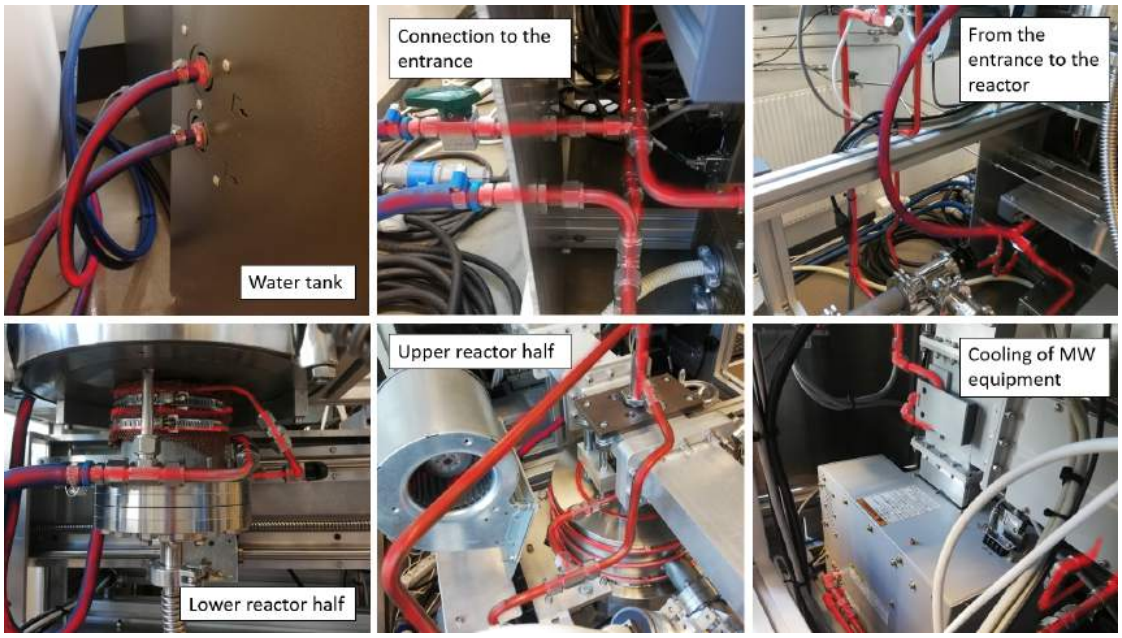

Figure 18: Check for water leaks along the water pipe. The water pipes in the figure have been made red such that it is easier to keep track of them. When looking for water leaks take especially care to investigate places where two pipes are connected together.

3.7 Overheating of the reactor's metal housing

If the temperature of the metal housing for the reactor reaches a large temperature, i.e. too warm to touch, stop the deposition immediately, something is either wrong

with the cooling, or the plasma environment. Figure 19 shows where the temperature of the reactor is checked.

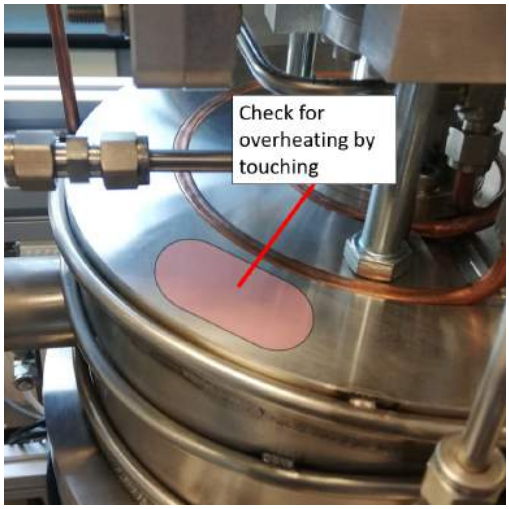

Figure 19: An easy way to tell if the system is overheated is by touching it in the region shown with a red color.

3.8 Hearing damage

Under prolonged stay, i.e. several hours, it is advised to wear ear protection if the pumps are running. Even with everything in stand-by except for the ventilation system, the noise level in the room is at 50-60 dB. When the MWPCVD system is operating, the noise level rises to 60-80 dB.

4 Procedure

Be sure to read and **understand** the whole procedure before running the system! The procedure is divided into five parts. Part (1) is the basic safety checks. Part (2) is the preparation of the reactor. Part (3) is the initialisation procedure for the system. Part (4) is the procedure and adjustments that can be made when the system is in equilibrium. Part (5) is the procedure needed to end the deposition. However, first we take a look at how to perform an emergency stop.

4.0 Emergency stop

To perform an emergency stop, hit the big red emergency button, shown in Figure 1a. Pressing the emergency button deactivates the microwave interlock, stopping microwaves from entering the chamber. After hitting the red button, set the non-hydrogen gases to 0 sccm, then follow the stop procedure explained in Section 4.5, starting at step 9.

4.1 Part 1: The basic safety checks

Before thinking about starting the system a few basic items needs to be checked.

- **Check that the microwave leakage detector is working by turning it on.** If the display is dim, then the batteries have to be replaced.
- Check that the water cooler has a water level between the minimum and the maximum level as shown in Figure 10.
- Check that the hydrogen tank has sufficient gas pressure. **During all points in time, the gas pressure of the tank has to be above 20 bar**. The rate of change in cylinder pressure is usually (-0.9 ± 0.1)bar/hr. Use these two pieces of information to calculate if there is enough hydrogen gas to conduct the deposition.
- Make sure that other gases used in the deposition have a gas pressure above 20 bar.

4.2 Part 2: The preparation of the reactor

1. Flip all the switches except for the reactor fan and turbo pump on the electrical panel, see Figure 11. This will supply power to several components like the mass flow switches, PC, and more.

2. **After turning on the power, it takes at least 30 minutes for the mass flow controllers to heat up and get ready. It is important that the mass flow meters are in thermal equilibrium before the they are used.**

3. If the chamber is dirty, clean it using one of two options: (1) wiping with acetone, or (2) etch with hydrogen gas. If acetone is being used, it is recommended to use gloves as acetone is a skin irritant. Hydrogen etching follows the same procedure as conventional deposition. However, only hydrogen gas is used as the gas supply. The duration of the etching is usually 1 hour with pressures between 70 and 100 torr.

4. Open the hydrogen gas following the detailed instructions given in the manual "Operation Instruction for PRAXIS SBM-204" found as an appendix to this user manual. Using it in conjunction with Figure 2 can be helpful.

5. Open the gas flow for the other gases. Only the cylinder valve needs to be turned for the methane supply.

6. Turn the computer on. The ON button is located behind the metal covers. However, by reaching around the cover, it can be turned on.

7. Check that the O-ring for the chamber is clean. If it is dirty, clean it using isopropanol.

8. Check that the groove for O-ring is clean. If it is dirty, clean it using isopropanol.

9. Load the substrate into the chamber using plastic tweezers.

10. Fit the two reactor halves together using the two wheel controls, shown in Figure 20. Hold the reactor on the opposite side of the support beam to provide counter torque when they are fitted together. This will allow the metal ridges to fit into the grooves. **Only use the wheel controls to guide the reactor halves, then use the following step tighten the connection:**

11. On the reactor there are 4 large holes, seen in Figure 21. These holes are made such that 4 bolts can be threaded through them, and used to tighten the chamber. The bolts are tightened by a pair of 17mm wrenches. Do not over-tighten the reactor at this point. The reactor will be further tightened during the initialization procedure when the vacuum pump is turned on.

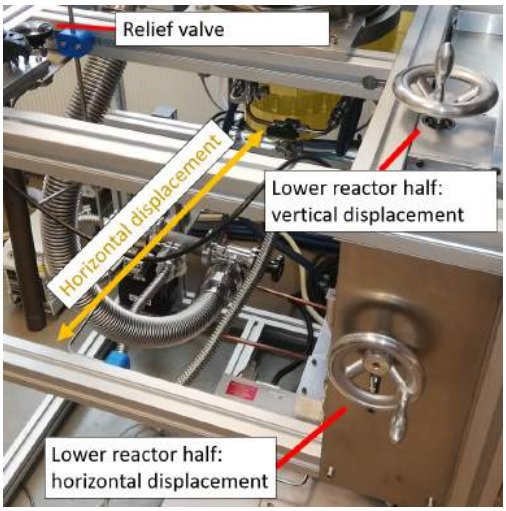

Figure 20: The adjustment wheels are used to adjust the vertical and the horisontal position of the lower reactor half seen in Figure 8. The position of the relief valve is also shown in the figure.

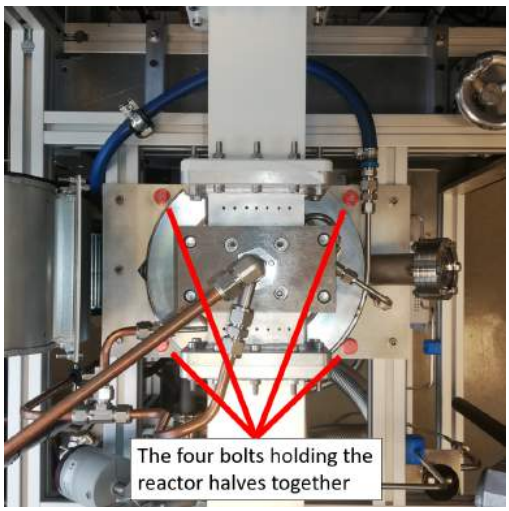

Figure 21: The positions of the 4 main bolts that hold the reactor together. Requires 2 x 17mm wrenches.

12. Close the relief valve by turning it clock-wise. The relief valve is shown in Figure 20.

13. Open the LabVIEW program used to run the reactor, see Figure 12.

$\Longrightarrow$ The system is now ready for the initialization procedure.

4.3 Part 3: The initialisation procedure

1. Run the LabVIEW program by clicking the white arrow in the top left of the LabVIEW front panel, see Figure 13.

2. In the front panel: Activate the "Open/close valve" button, this electronically opens the centralised pipe seen in Figure 3.

3. Activate the vacuum pump by turning the black nob, seen in Figure 4.

4. Further tighten the 4 bolts seen in Figure 21. However, do not overtighten the bolts. Fasten them only until they are tight enough to secure the reactor.

5. Check if the reactor is able to reach a pressure in the order of $\sim 10^{-2}$ mbar before continuing.

    - If the pressure couldn't be attained, it means that the system is not sealed properly. Turn off the vacuum pump, then **slowly** depressurize the chamber using the using the relief valve.

6. If a turbo molecular pump is connected to the system, use it to reach the baseline pressure. (As of date: 17/08/2020 it is not connected)

7. Open the gas access valves, seen Figure 3, but only for the gases needed in the deposition. This will allow gas into the mass flow meters. These are opened by flipping the levers from a horizontal position to a vertical position.

8. Turn on the water cooler unit, and the air conditioning unit.

9. Check for water leaks from the pipes. An overview of the water pipes are given in Figure 18.

10. Turn on the master switch for the microwave generator, see Figure 6.

11. Make a log file and save it to the logbook folder found in the LabVIEW folder.

12. Set the emissivity of the temperature measuring device. The exact coefficient depends on what material you wish to deposit. For polycrystalline diamond the emissivity has to be set to 0.6. The emissivity value is found by looking through the litterature.

13. Calculate the flow rate of the methane and other gasses: Hydrogen flow rate is usually set at 500 sccm. Flow rates in sccm is denoted by X, and flow rates in percentage is denoted by x. By knowing the value of all the gas percentages, and the primary gas flow rate, the flow rate of any secondary gas can then determined by the formula,

$$X_j(sccm) = X_p \frac{x_j}{x_p}$$

    where X_j is the gas flow in sccm of a particular secondary gas j, x_j is the associated gas flow percentage, X_p is the gas flow in sccm of the primary gas

(most commonly H_2), and x_p is the gas flow of the primary gas in percent. The definition of the gas flow percentage of the primary gas is given by:

$$1 = x_p + \sum_j x_j$$

which means that the sum of all of the percentages, consisting of the primary gas, and all the secondary gases should add up to 1.

14. In the front panel: increase the set values for the different gases from 0 sccm to the final set value.

15. In the front panel: Reset the butterfly valve by selecting and sending the command "B".

16. In the front panel: set the pressure to 25 Torr.

17. In the front panel: enable pressure interlock.

18. In the front panel: enable MW interlock.

19. In the tuning unit: set the tuning mode to auto.

20. Make sure the microwave leakage detector is ON.

21. In the front panel: set microwave power input (in LabVIEW) to 300W.

22. In the front panel: Ignite the plasma by activating the "MW power ON" button

    - If the plasma isn't formed deactivate the "MW power ON" button, and increase the power slightly.
    - Repeat the procedure above until plasma is formed.

23. Check that the automatic tuning works, the reflected power should be only a few watts.

24. Use the microwave leakage detector on the areas around the reactor. If the detector is beeping, it means that there is a large amount of microwave leakage, and the emergency button should be pressed.

25. Check for secondary plasma, using the secondary window. if it is formed turn the microwave power OFF and try again with lower microwave power.

26. Turn on the cooling fan for the upper reactor half and the lower reactor half, by activating power to them from the electrical panel (see Figure 11).

27. Move the temperature measuring device into position.

$\Longrightarrow$ The system has now finished the initialization procedure.

4.4 Part 4: The system equilibrium

For tuning the plasma an important key feature is that: the plasma size is increased with an increase in microwave power, and the plasma size is decreased with an increase in gas pressure. A specific temperature is reached by adjusting the microwave power.

4.5 Part 5: The end procedure

1. Turn off non-hydrogen gases, and let the plasma etch the substrate for 1-5 minutes.

2. In the tuning unit: change the tuning mode to manual. All the settings for the manual mode are properly set. There is no need to change them.

3. In the front panel: deactivate the "MW power ON" button.

4. In the front panel: turn off the "MW interlock".

5. Wait at least 1 minute, then turn off the power supply using the master switch.

6. In the front panel: set the chamber pressure to 100 torr, and let the gas cool down the substrate and the chamber.

7. In the front panel: deactivate the pressure interlock.

8. In the front panel: change the set point for the hydrogen gas to 0 sccm.

9. In the front panel: set the butterfly valve at 90 deg.

10. In the front panel: click on "open/close valve" such that it becomes deactivated. This will close the centralised pipe shown in Figure 3.

11. Turn off the gas cylinders. Remember the extra valve for the hydrogen tank located on the gas central.

12. Lock the cabinet that stores the gas cylinders.
13. Turn off the water cooler, reactor fans, and the air conditioning unit.
14. Let the vacuum pump reduce the pressure to $\sim 10^{-2}$ mbar.
15. Turn off the vacuum pump.
16. Very slowly open the relief valve to reintroduce atmosphere to the chamber. The valve is opened by turning it anti-clockwise.

$\Longrightarrow$ The system now fully prepared for next run.

5 Appendix

The next following pages details the operational instructions for the gas central: PRAXIS SBM-204.

PRAXAIR
Making our planet more productive

Operating Instructions

Manual Gas supply SBM 204

General information

This panel is suitable for all gas applications that require cleanliness and a high degree of safety.

One or several gas bottles/bundles can be connected on each side of the panel.

- Can be connected to a low pressure alarm system.
- Is delivered with a shut off valve VLM-200-PU.

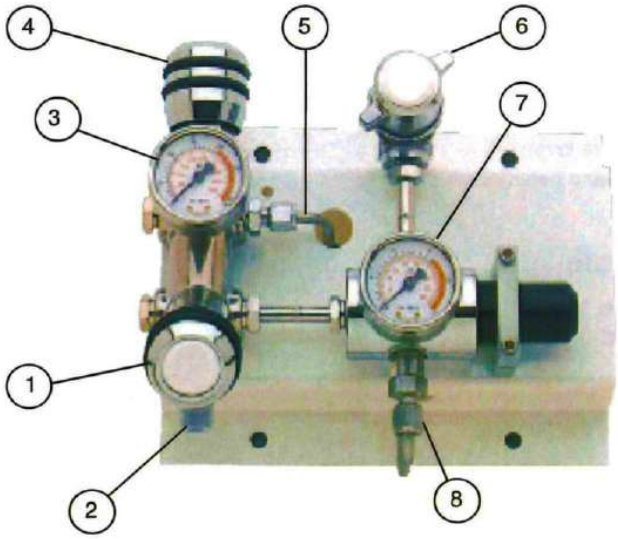

Position and description:

1 Shut off valve
2 Connection for high pressure hose
3 Manometer cylinder pressure
4 Purge valve
5 Purging
6 Shut off valve process
7 Manometer process
8 Safety Valve

Instructions SBM 204 Manual Gas supply

1.0 Start-up procedure

1.1 Place and secure gas bottle/gas bundle.
1.2 Connect bottle/bundle to the high pressure hose.
1.3 Use a suitable wrench.
1.4 Make sure valves 1 and 4 are closed.

2.0 Flushing Procedure

2.1 Open the cylinder valve slowly.
2.2 Check the pressure gauge in position 3.
2.3 Close the cylinder valve.
2.4 Open purge valve 4 to relieve the system down to 5-10 bar.
2.5 Close valve 4.
2.6 Repeat steps 2.1 to 2.5 at least three (3) times.

3.0 Operating procedure

3.1 Ensure that the valve 4 is closed.
3.2 Open the bottle/bundle valve, and valve 1 carefully.
3.3 Manometer 3 shows the bottle/bundle pressure level.
3.4 Manometer 7 shows the pressure at the pipeline network.

4.0 Changing bottle/bundle on the left hand side

4.1 Close the valve of the bottle/bundle and valve 1.
4.2 Relieve pressure in the hose through valve 4.
4.3 Close the valve 4.
4.4 Disconnect hose.
4.5 Once the new bottle/bundle is connected, run the flushing procedure 2.0 and operating procedure 3.0.

If experiencing irregularities, please contact Praxair

7.30 am - 3.30 pm: 92 29 15 50
Emergency service: 48 26 98 51

PRAXAIR
Making our planet more productive

Praxair Norge AS
e-post: norge@praxair.com

Tlf. 04277
www.praxair.no

Appendix B

New Reactor Software: LabVIEW Program

The new LabVIEW program is designed to work similar to the original LabVIEW program, however with has additional features and a structure which allows the user to more easily add additional code in a non-obstructive way. The orignal MWP-CVD program could do the following:

- General process functions:
  - Communicate with the gas inlet valve (Open/Close)
  - Communicate with the mass flow controllers (flow rate)
  - Communicate with the butterfly valve (pressure and valve degree)
  - Communicate with the microwave generator (ON/OFF, reset)
- Handle errors

In the original LabVIEW program, all the functionalities were located inside a single while loop. This made it very difficult to add new features. In the new program there are multiple parallel while loops each with its own purpose. New features can be be added simply by adding another case for while loop. In this way, additional code does not spread out across the screen, but stack inside the case structure. All the loops of the new LabVIEW program are listed below:

- User Interface: All actions done by the user is registered. Some of these events cause a message to be sent to another loop.
- Message Handler: All messages pass through the Message Handler loop. The message handler works as the post office for the LabVIEW program allowing loops to communicate with eachother. Messages consist of the loop address (the name of the recipient loop), the loop message (the instruction or keyword), and the message data (data value).
- Process: Contains the same general process functions as with the original LabVIEW program, but is executed both continuous actions as well as instructions from other loops. The process loop is mostly designed to interact

with instruments.

- Data Acquisition: Sends data requests to the process loop, and in return receives data from the process loop. The Data Acquisition loop also passes the data to other loops such as the User Output loop.
- User Output: Receives data from the Data Acquisition loop and other loops, and displays it on the Front Panel.
- Loop Monitor: Keeps track of the state of each loop. The primary use for the loop monitor is to make sure that the loops are initiated and shut down in the right order.
- Error Listing: Keeps track of all the errors which have emerged, when it first emerged, when is last emerged, how many times it emerged, from which loop the error originate, and the error code.
- Data Logging (history): Records all messages sent to the Process loop (with exception of data request) and saves them in a txt file.
- Data Logging (state): Continuously records the state of the process (e.g. records the temperature measurements).
- Preset Sender: Reads a file with instructions and executes them.
- Autonomous Control (emergency): Reads the state of the process, and check that everything is okay. If an emergency is found (e.g. overheating), the controller automatically sends a shut down message to message handler, which redirects it to all components.
- Autonomous Control (conventional): Works exactly like the Autonomous Control (emergency), but has a lower priority.

An overview of how these loops interact is shown in Figure B.1. Due to the fact there is in total 118 LabVIEW files needed to run this program, none of the block diagrams are shown. The front panel is shown in Figure B.2.

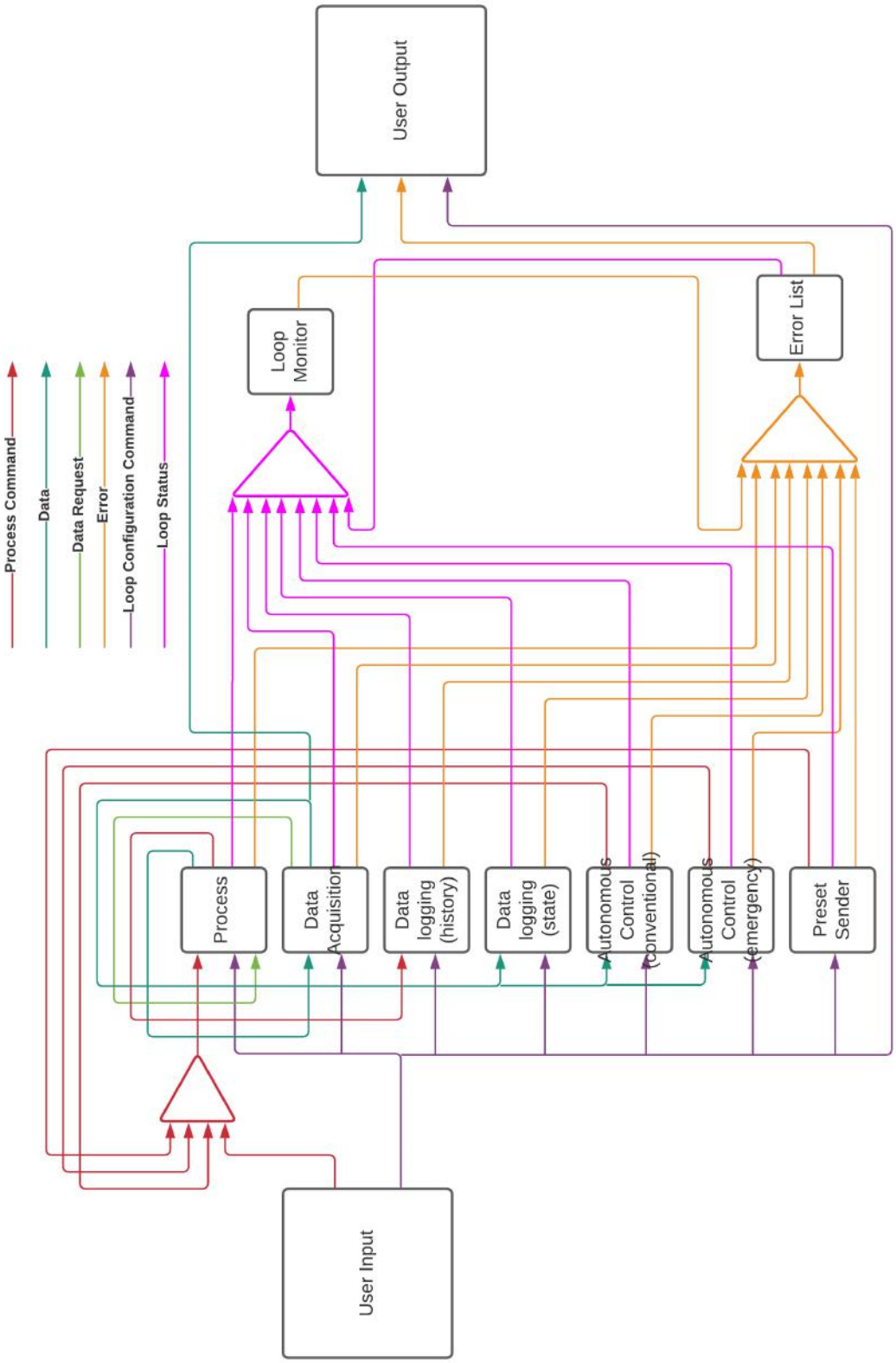

Figure B.1: Cross loop communication paths. Although not shown on the diagram, all cross loop communications pass through the Message Handler loop. This is not included such that the clutter is reduced.

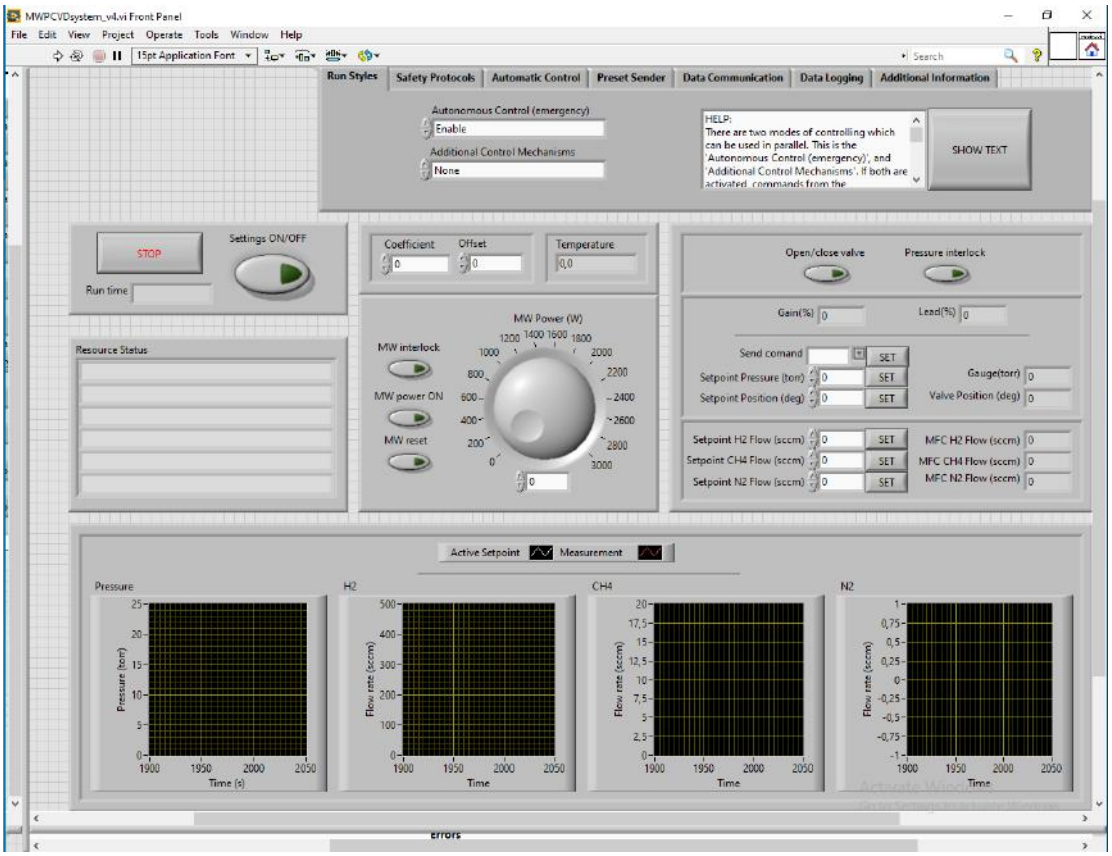

Figure B.2: Front panel of the new LabVIEW program. All the loop configuration commands are given in the settings tab on the front panel. Loop configuration commands is additional parameters which can be sent to a loop examples of this is: Sampling rate (i.e. how often data requests are sent from the data acquisition loop to the process loop), path of the file for the Preset Sender loop (to read the instructions from a txt file, it needs to know the name and location of the file).

Bibliography

[1] IEA Paris. Global energy review 2020. *IEA*, 2020. URL https://www.iea.org/reports/global-energy-review-2020.

[2] IEA Paris. World energy outlook 2020. *IEA*, 2020. URL https://www.iea.org/reports/world-energy-outlook-2020.

[3] IEA Paris. World energy model. 2013. URL https://www.iea.org/reports/world-energy-model.

[4] IEA Paris. Onshore wind. *IEA*, 2020. URL https://www.iea.org/reports/onshore-wind.

[5] IEA Paris. Offshore wind. *IEA*, 2020. URL https://www.iea.org/reports/offshore-wind.

[6] Javier Serrano-González and Roberto Lacal-Arántegui. Technological evolution of onshore wind turbines—a market-based analysis. *Wind Energy*, 19(12):2171–2187, 2016. doi: 10.1002/we.1974. URL https://onlinelibrary.wiley.com/doi/abs/10.1002/we.1974.

[7] IEA. Wind energy: technology roadmap. *IEA*, 2013. URL https://webstore.iea.org/technology-roadmap-wind-energy-2013.

[8] M H Keegan, D H Nash, and M M Stack. On erosion issues associated with the leading edge of wind turbine blades. *Journal of Physics D: Applied Physics*, 46(38):383001, sep 2013. doi: 10.1088/0022-3727/46/38/383001. URL https://doi.org/10.1088%2F0022-3727%2F46%2F38%2F383001.

[9] Agrim Sareen, Chinmay A. Sapre, and Michael S. Selig. Effects of leading edge erosion on wind turbine blade performance. *Wind Energy*, 17(10):1531–1542, October 2014. ISSN 1095-4244. doi: 10.1002/we.1649.

[10] N. Dalili, A. Edrisy, and R. Carriveau. A review of surface engineering issues critical to wind turbine performance. *Renewable and Sustainable Energy Reviews*, 13(2):428 – 438, 2009. ISSN 1364-0321. doi: https://doi.org/10.1016/j.rser.2007.11.009. URL http://www.sciencedirect.com/science/article/pii/S1364032107001554.

[11] Luis Bartolomé and Julie Teuwen. Prospective challenges in the experimentation of the rain erosion on the leading edge of wind turbine blades. *Wind Energy*, 22(1):140–151, 2019. doi: 10.1002/we.2272. URL https://onlinelibrary.wiley.com/doi/abs/10.1002/we.2272.

[12] B.F. Soerensen, E. Joergensen, C.P. Debel, F.M Jensen, H.M Jensen, T. Jacobsen, and K.M. Halling. Improved design of large wind turbine blade of fibre composites based on studies of scale effects (phase 1) - summary report, Sep 2004.

[13] Junlei Chen, Jihui Wang, and Aiqing Ni. A review on rain erosion protection of wind turbine blades. *Journal of Coatings Technology and Research*, 16(1): 15–24, Jan 2019. ISSN 1935-3804. doi: 10.1007/s11998-018-0134-8. URL https://doi.org/10.1007/s11998-018-0134-8.

[14] William F Adler. Rain impact retrospective and vision for the future. *Wear*, 233-235:25 – 38, 1999. ISSN 0043-1648. doi: https://doi.org/10.1016/S0043-1648(99)00191-X. URL http://www.sciencedirect.com/science/article/pii/S004316489900191X.

[15] Leon Mishnaevsky Jr. Toolbox for optimizing anti-erosion protective coatings of wind turbine blades: Overview of mechanisms and technical solutions. *Wind Energy*, 22(11):1636–1653, 2019. doi: https://doi.org/10.1002/we.2378. URL https://onlinelibrary.wiley.com/doi/abs/10.1002/we.2378.

[16] H.M. Slot, E.R.M. Gelinck, C. Rentrop, and E. van der Heide. Leading edge erosion of coated wind turbine blades: Review of coating life models. *Renewable Energy*, 80:837 – 848, 2015. ISSN 0960-1481. doi: https://doi.org/10.1016/j.renene.2015.02.036. URL http://www.sciencedirect.com/science/article/pii/S0960148115001366.

[17] A.G. Evans, M.E. Gulden, and M. Rosenblatt. Impact Damage in Brittle Materials in the Elastic-Plastic Response Regime. *Proceedings of the Royal Society of London Series A*, 361(1706):343–365, June 1978. doi: 10.1098/rspa.1978.0106.

[18] J.D. ACHENBACH. *Wave Propagation in Elastic Solids*. North-Holland Series in Applied Mathematics and Mechanics. Elsevier, Amsterdam, 1975. doi: https://doi.org/10.1016/B978-0-7204-0325-1.50008-4. URL https://www.sciencedirect.com/science/article/pii/B9780720403251500084.

[19] J.E. Butler and A.V. Sumant. The cvd of nanodiamond materials. *Chemical Vapor Deposition*, 14(7-8):145–160, 2008. doi: 10.1002/cvde.200700037. URL https://onlinelibrary.wiley.com/doi/abs/10.1002/cvde.200700037.

[20] Matthias Lodes, F Kachold, and S. Rosiwal. Mechanical properties of micro- and nanocrystalline diamond foils. *Philosophical transactions. Series A, Mathematical, physical, and engineering sciences*, 373, 03 2015. doi: 10.1098/rsta.2014.0136.

[21] D. K. Reinhard, T. A. Grotjohn, M. Becker, M. K. Yaran, T. Schuelke, and J. Asmussen. Fabrication and properties of ultranano, nano, and microcrystalline diamond membranes and sheets. *Journal of Vacuum Science & Technology B: Microelectronics and Nanometer Structures Processing, Measurement, and Phenomena*, 22(6):2811–2817, 2004. doi: 10.1116/1.1819928. URL https://avs.scitation.org/doi/abs/10.1116/1.1819928.

[22] Y. Muranaka, H. Yamashita, and H. Miyadera. Low temperature (400 °c) growth of polycrystalline diamond films in the microwave plasma of co/h2 and co/h2/ar systems. *Journal of Vacuum Science and Technology*, 9:76–84, 1991.

[23] J.J. Gilman. Why diamond is very hard. *Philosophical Magazine A*, 82(10): 1811–1820, 2002. doi: 10.1080/01418610208235692. URL https://doi.org/10.1080/01418610208235692.

[24] R.J. Hemley V.V. Brazhkin, A.G. Lyapin. Harder than diamond: Dreams and reality. *Philosophical Magazine A*, 82(2):231–253, 2002. doi: 10.1080/01418610208239596. URL https://doi.org/10.1080/01418610208239596.

[25] R.H. Telling, C.J. Pickard, M.C. Payne, and J.E. Field. Theoretical strength and cleavage of diamond. *Phys. Rev. Lett.*, 84:5160–5163, May 2000. doi: 10.1103/PhysRevLett.84.5160. URL https://link.aps.org/doi/10.1103/PhysRevLett.84.5160.

[26] Thomas A. Scott. The influence of microstructure on the mechanical properties of polycrystalline diamond: a literature review. *Advances in Applied Ceramics*, 117(3):161–176, Apr 2018. ISSN 1743-6753. doi: 10.1080/17436753.2017.1389462. URL https://doi.org/10.1080/17436753.2017.1389462.

[27] Pierre Cartigny, Médéric Palot, Emilie Thomassot, and Jeff W. Harris. Diamond Formation: A Stable Isotope Perspective. *Annual Review of Earth and Planetary Sciences*, 42:699–732, May 2014. doi: 10.1146/annurev-earth-042711-105259.

[28] J.M. Zazula. On Graphite Transformations at High Temperature and Pressure Induced By Absorption of the LHC Beam. Technical Report LHC-Project-Note-78, CERN, Geneva, Jan 1997. URL `http://cds.cern.ch/record/691793`.

[29] F.P. Bundy, W.A. Bassett, M.S. Weathers, R.J. Hemley, H.U. Mao, and A.F. Goncharov. The pressure-temperature phase and transformation diagram for carbon; updated through 1994. *Carbon*, 34(2):141–153, 1996. ISSN 0008-6223. doi: https://doi.org/10.1016/0008-6223(96)00170-4. URL `https://www.sciencedirect.com/science/article/pii/0008622396001704`.

[30] J. Steinbeck et al. A model for pulsed laser melting of graphite. *Journal of Applied Physics*, 58(11):4374–4382, 1985. doi: 10.1063/1.335527. URL `https://doi.org/10.1063/1.335527`.

[31] Milton Ohring. Chapter 6 - chemical vapor deposition. In Milton Ohring, editor, *Materials Science of Thin Films (Second Edition)*, pages 277–355. Academic Press, San Diego, second edition edition, 2002. ISBN 978-0-12-524975-1. doi: https://doi.org/10.1016/B978-012524975-1/50009-4. URL `https://www.sciencedirect.com/science/article/pii/B9780125249751500094`.

[32] F Silva, K Hassouni, X Bonnin, and A Gicquel. Microwave engineering of plasma-assisted CVD reactors for diamond deposition. *Journal of Physics: Condensed Matter*, 21(36):364202, aug 2009. doi: 10.1088/0953-8984/21/36/364202. URL `https://doi.org/10.1088/0953-8984/21/36/364202`.

[33] J Christopher Whitehead. Plasma–catalysis: the known knowns, the known unknowns and the unknown unknowns. *Journal of Physics D: Applied Physics*, 49(24):243001, may 2016. doi: 10.1088/0022-3727/49/24/243001. URL `https://doi.org/10.1088/0022-3727/49/24/243001`.

[34] C.G. Schwärzler, O. Schnabl, J. Laimer, and H. Störi. On the plasma chemistry of the c/h system relevant to diamond deposition processes. *Plasma Chemistry and Plasma Processing*, 16(2):173–185, Jun 1996. ISSN 1572-8986. doi: 10.1007/BF01570176. URL `https://doi.org/10.1007/BF01570176`.

[35] Roland Haubner. Low-pressure diamond: from the unbelievable to technical products. *ChemTexts*, 7(2):10, Mar 2021. ISSN 2199-3793. doi: 10.1007/s40828-021-00136-z. URL https://doi.org/10.1007/s40828-021-00136-z.

[36] J.J. Gracio, Q.H. Fan, and J.C. Madaleno. Diamond growth by chemical vapour deposition. *Journal of Physics D: Applied Physics*, 43(37):374017, sep 2010. doi: 10.1088/0022-3727/43/37/374017. URL https://doi.org/10.1088/0022-3727/43/37/374017.

[37] Butler et al. Thin film diamond growth mechanisms [and comment]. *Philosophical Transactions: Physical Sciences and Engineering*, 342(1664): 209–224, 1993. ISSN 1935-3804. doi: 10.1098/rsta.1993.0015. URL www.jstor.org/stable/54081.

[38] L. R. Martin. High-quality diamonds from an acetylene mechanism. *Journal of Materials Science Letters*, 12(4):246–248, Jan 1993. ISSN 1573-4811. doi: 10.1007/BF00539814. URL https://doi.org/10.1007/BF00539814.

[39] M.P D'Evelyn, J.D. Graham, and L.R. Martin. The role of methyl radicals and acetylene in [100] vs. [111] diamond growth. *Diamond and Related Materials*, 10(9):1627–1632, 2001. ISSN 0925-9635. doi: https://doi.org/10.1016/S0925-9635(01)00441-1. URL https://www.sciencedirect.com/science/article/pii/S0925963501004411. Proceedings of the 7th International Conference on New Diamond Science and Technology(ICNDST-7).

[40] R. Mania and R. Pampuch L. Stobierski. Diamond synthesis in cool plasma. *Kristall und Technik*, 16(7):785–788, 1981. doi: https://doi.org/10.1002/crat.2170160709. URL https://onlinelibrary.wiley.com/doi/abs/10.1002/crat.2170160709.

[41] M. Tsuda, M. Nakajima, and S. Oikawa. Epitaxial growth mechanism of diamond crystal in methane-hydrogen plasma. *Journal of the American Chemical Society*, 108(19):5780–5783, 1986. doi: 10.1021/ja00279a019. URL https://doi.org/10.1021/ja00279a019. PMID: 22175327.

[42] P.W. May, J.N Harvey, N.L Allan, J.C. Richley, and Y.A. Mankelevich. Simulations of chemical vapor deposition diamond film growth using a kinetic monte carlo model. *Journal of Applied Physics*, 108(1):014905, 2010. doi: 10.1063/1.3437647. URL https://doi.org/10.1063/1.3437647.

[43] M. Frenklach and K.E. Spear. Growth mechanism of vapor-deposited diamond. *Journal of Materials Research*, 3(1):133–140, 1988. doi: 10.1557/JMR.1988.0133.

[44] D. Huang, M. Frenklach, and M. Maroncelli. Energetics of acetylene-addition mechanism of diamond growth. *The Journal of Physical Chemistry*, 92(22):6379–6381, 1988. doi: 10.1021/j100333a039. URL https://doi.org/10.1021/j100333a039.

[45] F.M. Cerio, W.A. Weimer, and C.E. Johnson. Diamond growth using carbon monoxide as a carbon source. *Journal of Materials Research*, 7(5):1195–1203, May 1992. ISSN 2044-5326. doi: 10.1557/JMR.1992.1195. URL https://doi.org/10.1557/JMR.1992.1195.

[46] D.C. Barbosa, P. Hammer, V.J. Trava-Airoldi, and E.J. Corat. The valuable role of renucleation rate in ultrananocrystalline diamond growth. *Diamond and Related Materials*, 23:112–119, 2012. ISSN 0925-9635. doi: https://doi.org/10.1016/j.diamond.2012.01.028. URL https://www.sciencedirect.com/science/article/pii/S0925963512000386.

[47] Paul W. May and Yuri A. Mankelevich. From ultrananocrystalline diamond to single crystal diamond growth in hot filament and microwave plasma-enhanced cvd reactors: a unified model for growth rates and grain sizes. *The Journal of Physical Chemistry C*, 112(32):12432–12441, Aug 2008. ISSN 1932-7447. doi: 10.1021/jp803735a. URL https://doi.org/10.1021/jp803735a.

[48] M. Ali and M. Ürgen. Surface morphology, growth rate and quality of diamond films synthesized in hot filament cvd system under various methane concentrations. *Applied Surface Science*, 257(20):8420–8426, 2011. ISSN 0169-4332. doi: https://doi.org/10.1016/j.apsusc.2011.04.097. URL https://www.sciencedirect.com/science/article/pii/S0169433211006428.

[49] C.J. Tang, A.J. Neves, and A.J.S. Fernandes. Study the effect of o2 addition on hydrogen incorporation in cvd diamond. *Diamond and Related Materials*, 13(1):203–208, 2004. ISSN 0925-9635. doi: https://doi.org/10.1016/j.diamond.2003.10.032. URL https://www.sciencedirect.com/science/article/pii/S0925963503004242.

[50] T. Kawato and K. Kondo. Effects of Oxygen on CVD Diamond Synthesis. *Japanese Journal of Applied Physics*, 26(9):1429, September 1987.

doi: 10.1143/JJAP.26.1429. URL https://ui.adsabs.harvard.edu/abs/1987JaJAP..26.1429K.

[51] C.J. Tang, A.J. Neves, S. Pereira, A.J.S. Fernandes, J. Grácio, and M.C. Carmo. Effect of nitrogen and oxygen addition on morphology and texture of diamond films (from polycrystalline to nanocrystalline). *Diamond and Related Materials*, 17(1):72–78, 2008. ISSN 0925-9635. doi: https://doi.org/10.1016/j.diamond.2007.10.022. URL https://www.sciencedirect.com/science/article/pii/S0925963507004402.

[52] H.C. Shih, C.P. Sung, W.L. Fan, and W.T. Hsu. Growth and morphological changes of chemically vapour deposited diamond in the presence of argon. *Thin Solid Films*, 232(1):41–46, 1993. ISSN 0040-6090. doi: https://doi.org/10.1016/0040-6090(93)90759-I. URL https://www.sciencedirect.com/science/article/pii/004060909390759I.

[53] D. Zhou, D.M. Gruen, L.C. Qin, T.G McCauley, and A.R Krauss. Control of diamond film microstructure by ar additions to ch4/h2 microwave plasmas. *Journal of Applied Physics*, 84(4):1981–1989, 1998. doi: 10.1063/1.368331. URL https://doi.org/10.1063/1.368331.

[54] J. Stiegler, A. Bergmaier, J. Michler, S. Laufer, G. Dollinger, and E. Blank. The effect of nitrogen on low temperature growth of diamond films. *Thin Solid Films*, 352(1):29–40, 1999. ISSN 0040-6090. doi: https://doi.org/10.1016/S0040-6090(99)00285-0. URL https://www.sciencedirect.com/science/article/pii/S0040609099002850.

[55] Y. Muranaka, H. Yamashita, and H. Miyadera. Worldwide status of low temperature growth of diamond. *Diamond and Related Materials*, 3(4):313–318, 1994. ISSN 0925-9635. doi: https://doi.org/10.1016/0925-9635(94)90177-5. URL https://www.sciencedirect.com/science/article/pii/0925963594901775. Proceedings of the 4th European Conference on Diamond, Diamond-like and Related Materials.

[56] J. Stiegler, A. Bergmaier, J. Michler, Y. von Kaenel, G. Dollinger, and E. Blank. Impurity and defect incorporation in diamond films deposited at low substrate temperatures. *Diamond and Related Materials*, 7(2):193–199, 1998. ISSN 0925-9635. doi: https://doi.org/10.1016/S0925-9635(97)00164-7. URL https://www.sciencedirect.com/science/article/pii/S0925963597001647.

[57] J.J. Su, Y.F. Li, X.L. Li, P.L. Yao, Y.Q. Liu, M.H. Ding, and W.Z. Tang. A novel microwave plasma reactor with a unique structure for chemical vapor deposition of diamond films. *Diamond and Related Materials*, 42:28–32, 2014. ISSN 0925-9635. doi: https://doi.org/10.1016/j.diamond.2013.12.001. URL https://www.sciencedirect.com/science/article/pii/S0925963513002343.

[58] G.A. Maugin. *The Thermomechanics of Nonlinear Irreversible Behaviors*. World Scientific, 1999. doi: 10.1142/3700. URL https://www.worldscientific.com/doi/abs/10.1142/3700.

[59] COMSOL Multiphysics. The heat transfer module user's guide. *COMSOL Multiphysics 5.5, Burlington, MA, accessed April*, 9:156–159, 1998.

[60] P. Larkin. *Infrared and raman spectroscopy : principles and spectral interpretation*. Elsevier, Saint Louis, second edition edition, 2011. ISBN 9780123869845.

[61] W. Kulisch, L. Ackermann, and B. Sobisch. On the mechanisms of bias enhanced nucleation of diamond. *physica status solidi (a)*, 154(1):155–174, 1996. doi: https://doi.org/10.1002/pssa.2211540113. URL https://onlinelibrary.wiley.com/doi/abs/10.1002/pssa.2211540113.

[62] A.M. Zaitsev, editor. *Optical Properties of Diamond*. Springer-Verlag Berlin Heidelberg, 2001. ISBN 978-3-540-66582-3. doi: 10.1007/978-3-662-04548-0.

[63] V.I. Korepanov, H. Hamaguchi, E. Osawa, V. Ermolenkov, I.K. Lednev, J.M.B. Etzold, O. Levinson, B. Zousman, C.P. Epperla, and H.C. Chang. Carbon structure in nanodiamonds elucidated from raman spectroscopy. *Carbon*, 121:322–329, 2017. ISSN 0008-6223. doi: https://doi.org/10.1016/j.carbon.2017.06.012. URL https://www.sciencedirect.com/science/article/pii/S0008622317305791.

[64] A.C. Ferrari and J. Robertson. Raman spectroscopy of amorphous, nanostructured, diamond–like carbon, and nanodiamond. *Philosophical Transactions of the Royal Society of London. Series A: Mathematical, Physical and Engineering Sciences*, 362(1824):2477–2512, 2004. doi: 10.1098/rsta.2004.1452. URL https://royalsocietypublishing.org/doi/abs/10.1098/rsta.2004.1452.

[65] G. Irmer and A. Dorner-Reisel. Micro-raman studies on dlc coatings. *Advanced Engineering Materials*, 7(8):694–705, 2005. doi: https://doi.org/10.1002/adem.200500006. URL https://onlinelibrary.wiley.com/doi/abs/10.1002/adem.200500006.

[66] S. Prawer and R.J. Nemanich. Raman spectroscopy of diamond and doped diamond. *Philosophical Transactions of the Royal Society A: Mathematical, Physical and Engineering Sciences*, 362(1824):2537–2565, November 2004. ISSN 0962-8428. doi: 10.1098/rsta.2004.1451.

[67] S Bühlmann, E Blank, R Haubner, and B Lux. Characterization of ballas diamond depositions. *Diamond and Related Materials*, 8 (2):194–201, 1999. ISSN 0925-9635. doi: https://doi.org/10.1016/S0925-9635(98)00258-1. URL https://www.sciencedirect.com/science/article/pii/S0925963598002581.

[68] Diamond films on planar (flat) substrates. URL http://www.chm.bris.ac.uk/pt/diamond/semflat.htm.

[69] R. Tu, T. Xu, D. Li, S. Zhang, M. Yang, Q. Li, L. Zhang, T. Shimada, T. Goto, and J. Shi. Morphology and mechanical behavior of diamond films fabricated by ih-mpcvd. *RSC Adv.*, 8:16061–16068, 2018. doi: 10.1039/C8RA01871E. URL http://dx.doi.org/10.1039/C8RA01871E.

[70] J. Stiegler, T. Lang, M. Nygard-Ferguson, Y. von Kaenel, and E. Blank. Low temperature limits of diamond film growth by microwave plasma-assisted cvd. *Diamond and Related Materials*, 5(3):226–230, 1996. ISSN 0925-9635. doi: https://doi.org/10.1016/0925-9635(95)00349-5. URL https://www.sciencedirect.com/science/article/pii/0925963595003495.

[71] O.A. Williams, editor. *Nanodiamond*. Nanoscience & Nanotechnology Series. The Royal Society of Chemistry, 2014. ISBN 978-1-84973-639-8. doi: 10.1039/9781849737616. URL http://dx.doi.org/10.1039/9781849737616.

Appendix 20pt